University of Stavanger

Faculty of Science and Technology

MASTER'S THESIS

Study program/ Specialization: Master of Science in Petroleum Engineering Specialization - Reservoir Engineering	Spring semester, 2017 Open / ~~Restricted~~ access
Writer: Shijia Ma	…… (Writer's signature)
Faculty supervisor: Merete Vadla Madland and Reidar Inge Korsnes	
Thesis title: **PERMEABILITY EVOLUTION OF CHALK UNDER DIFFERENT STRESS STATES**	
Credits (ECTS): 30	
Key words: Chalk Permeability evolution Hydrostatic test Deviatoric test Creep	Pages: 116 Stavanger, 15/06/2017 Date/year

Title page for Master's Thesis Faculty of Science and Technology

Abstract

This thesis reports the results obtained from triaxial tests on Kansas outcrop chalk flooded with inert NaCl brine. Permeability measurements are conducted at 50ºC under different stress states simulated by five test sequences of hydrostatic and deviatoric loadings. The loading behaviors like shear failure, dilatancy, compression of chalk and their influences on permeability evolution are studied and discussed in detail. The results show that permeability is strongly dependent on stress and strain. It generally decreases with increasing confining pressure by compressing the pore spaces. Deviatoric loading performed prior to hydrostatic loading has minor effect on permeability. As the confining pressure continues to increase, permeabilities of all the tested samples tend to converge. Shear failure occurring in the deviatoric loading phase contributes to the enhancement of permeability in chalk with porosities ranging from 38 to 40%. Single shear-band failure is exhibited with a symbol of the critical point where radial strain rate exceeds axial strain rate. This behavior is accompanied with an increase in permeability. Despite the profound influences of the loading phases, short-term creep and unloading cycles only have minor effects on permeability evolution. Experimental results from deviatoric loadings indicate that confining pressure has a great influence on permeability since chalks tend to be more brittle at lower confining pressure, thus resulting in greater increase in permeability when shear failure occurs.

These experimental results can provide the fundamental approaches to establish the basic understanding of the stress states impact on permeability evolution and can be employed as a foundation and illustration for the future work.

Table of Contents

Acknowledgement

My deep gratitude goes first to my supervisor, Professor Merete V. Madland, who has expertly guided me through the master thesis and broaden my scope of mind with her expertise. Without her guidance and continuous assitance, this work would not have been possible.

My appreciation also extends Dr. Reidar I. Korsnes for shearing his knowledge and furnishing me with new ideas for the thesis work. His mentoring and encouragement have been especially valuable and appreciated.

I would also like to express my gratitude to Dr. Emanuela I. Kallesten for her assistance on the master thesis.

Above ground, I am indebted to my family, whose value to me only grows with age.

List of Figures

List of Tables

Chapter 1 Introduction

Permeability is considered one of the fundamentally important characteristics of the hydrocarbon reservoirs due to the fact that it can be used to measure the productivity of the reservoir. At a time scale of the industrial underground activities, i.e. petroleum production, pressure depletion associated with the production might induce strains and deformations of the reservoir rocks, resulting in serious consequences like the subsidence (Wiborg and Jewhurst, 1986) or permeability damages.

Since the permeability of the formation is related to the stress state and deformation of the rock, therefore, a better understanding of the rock deformation under different stress states and its effect on permeability can lead to an improvement of the reservoir predictions.

1.1 Background

Hydrocarbon-bearing chalk rocks have been found in the North Sea, Gulf Coast, Middle East, midcontinent region of the U.S. and the Scotian Shelf of Canada (Scholle 1977). In the development of these reservoirs, challenges were encountered due to the unusual mechanical properties of chalk:

High Porosity. The chalk reservoirs have a relatively high porosity, which can be as high as 70% (Fjær et al., 2008). Chalks with a porosity of 35-45% are favorable, which only possess a permeability of 1-3 mD (Hardman, 1982).

Low permeability. Despite the high porosity, chalk reservoirs exhibit low permeabilities in a range around 1-10 mD (Thomas, 1981).

Production. For most of the chalk reservoirs, the permeability is low enough to trap the pore fluids resulting in abnormally high pore pressures (Byrd et al., 1975). As production of the reservoir continues, due to the reduction in pore pressure, it may give rise to compaction of the reservoir causing the subsidence or resulting in a shift of weight to the soft matrix leading to pore collapse and further permeability reduction. These challenges during production draws attention to the fundamental study on the

mechanical behavior of chalk. The ability to predict pore collapse or permeability change at different stress states may lead to an increase in recovery.

1.2 Permeability studies

During the production interval of a reservoir, the pore pressure undergoes variations of increase or decrease. These variations of the reservoir pore pressure promote the alterations of effective stresses and total stress distributions within the reservoir and the surrounding rocks. The rock geomechanical changes may give rise to a drastic decrease in the rock permeability, causing a reduction in reservoir productivity. In contrast, cases of an increase in permeability were also reported from laboratory tests carried out by Rhett and Teufel (1992) as well as Zhu and Wong (2008).

In order to get a clearer understanding of the permeability evolution, extensive work has been conducted in the laboratories to evaluate the influence of the effective stresses on the reservoir permeability over the last 60 years. The pioneering work carried out by Fatt & Davis (1952) demonstrates that the specific permeability of intact sandstone decreases with increasing overburden pressure, which was in agreement with the research conducted by Donald et al. (1963). Furthermore, the effect of pressure on permeability was studied by Nelson and Handin in 1977, indicating that the deformation of fractures in the porous sandstone under confining pressure is mostly inelastic and the permeability decrease was lower during the second loading. The shear deformation effect on the permeability of fractured rock has been investigated by Teuful in 1987. The results specify a permeability decrease with increasing shear deformation. In some laboratory studies, it is shown that the permeability experiences significant modifications under hydrostatic or non-hydrostatic stresses. Generally, an increase in mean stress will result in a deduction in permeability, whereas, regarding the deviatoric stress effects on permeability, it is dependent on the rock type, porosity, and failure mode (Zhong and Wong, 1997). Subsequently, the relationship between permeability and porosity was studied by Zhong and Wong (2008), indicating that for porous rock, the permeability and porosity during the shear enhanced compaction can be approximated by a liner function rather than power law relationship. The study of stress path effect on permeability of sandstone was investigated by Rhett and Teufel (1992)

indicating an increase in permeability when the constant stress ratio K is lower than 0.75.

Based on these studies on permeability, it is shown that permeability generally decreases with increasing effective stress. During a hydrostatic loading test, the behavior commonly observed is a decrease in the permeability with increasing effective confining pressure, which simulates the effective mean stress in the reservoir. Regarding the impact of deviatoric stress on permeability, both decrease and increase were reported in laboratory studies, depending on different factors like rock type, porosity and stress path/state. A great amount of these experimental studies are conducted on sandstone and less studies on chalk under different stress conditions are reported in the literature. Korsnes et al. (2006) performed a stress dependent permeability study on chalk indicating that increasing hydrostatic stress gives rise to reduction in permeability, whereas, deviatoric stress has only minor effects on the permeability evolution. Therefore, a more specific study on the chalk permeability evolution under different stress states achieved by different sequences of either hydrostatic or deviatoric loading is necessary.

1.3 Production challenges

Ekofisk field is located within the central graben of North Sea in the Norwegian Sector with water depth at 70m. Figure 1.1 is the location map showing structure at the top of the chalk, which is the Ekofisk Formation. The Ekofisk oil field is first discovered by Phillips Petroleum Company and the first production takes place in 1971. Ever since that time, the Ekofisk field has been under production for more than 40 years until now. In the primary production phase, pressure decline due to the production of hydrocarbons caused compaction of the reservoir and furthermore lead to subsidence of the seafloor. The hydrocarbon production in this phase induces a depletion that in turn induces variation of the in-situ stresses. The changes in mechanical parameters and petrophysical characteristics of the rock can thus have an impact on permeability affecting the reservoir productivity.

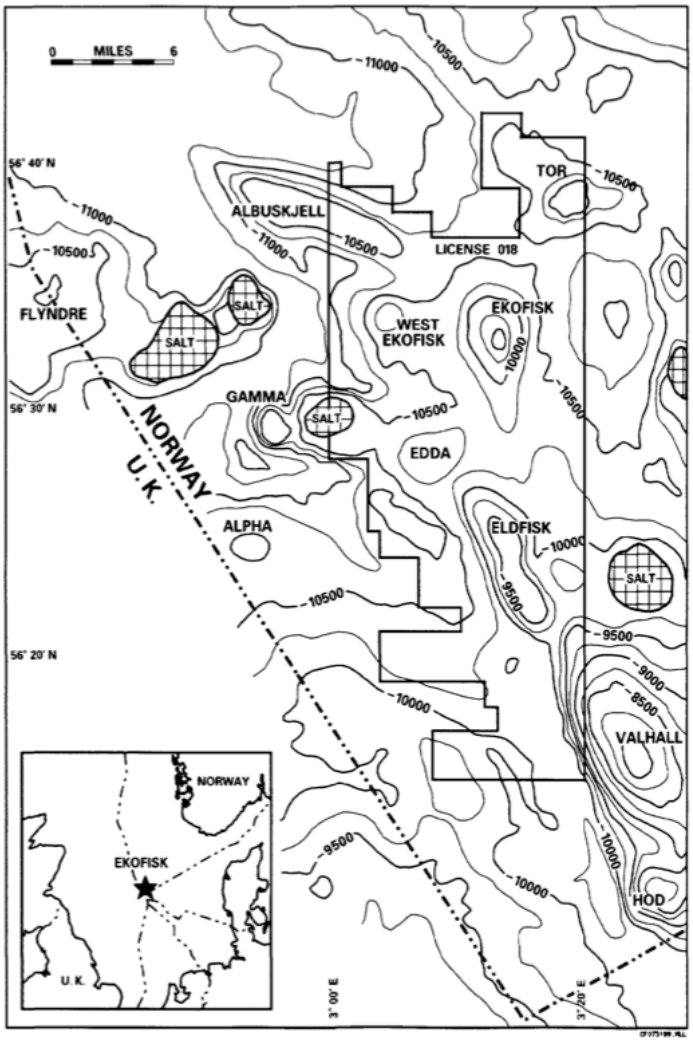

Figure 1.1 Location map showing structure at Ekofisk Formation (Charles et al., 1990)

Enhanced recovery studies on Ekofisk field were initiated soon after the start of the primary production. Waterflooding was applied after the primary production to increase the reservoir pressure to its initial level and maintain the pressure. This voidage replacement has also been used to mitigate the additional surface subsidence. In the study of failure of chalk during waterflooding in the Ekofisk field performed by Teufel and Rhett et al. (1992) in the laboratory demonstrates that the large increase in permeability measured before and after waterflooding indicates the extensive nature of waterflood-induced fracturing due to the reduction in principal effective stresses caused by the injection of cold seawater.

As the reservoir undergoes the process of compaction, depletion and repressurizing during the production, the inherent properties of the formation rock can be altered due

to the in-situ stress or pressure changes. Simulations of the reservoir conditions and tests under different stress states can enhance the understanding of permeability evolution, resulting in a better prediction in reservoir production and avoiding reduction on reservoir productivity.

1.4 Objectives

This thesis aims at studying the permeability evolution of chalk under different stress states at low temperature for the purpose of establishing views on the effect of compaction on permeability and further aiding in predicting permeability behavior at actual reservoir conditions.

To achieve this goal, simple diagnostic tests will be designed to experience deformations assumed to have an influence on permeability. The permeability of chalk can be measured under both hydrostatic and non-hydrostatic conditions. In a hydrostatic test, the axial stress is equal to the confining stress. Non-hydrostatic test is the triaxial compression tests consisting of two phases: first a hydrostatic phase and then a deviatoric phase. In the deviatoric phase, the confining pressure is kept constant, and the axial stress is increased until failure. These designed stress sequences for chalk cores will have different impact on the core permeability. With these variations in permeabilities, a reasonable interpretation and better understanding of the permeability evolution could be achieved.

1.5 Outline of the thesis

In Chapter 2, the geological-aspect literature review of chalk rock in North Sea is covered. Basic mechanical concepts and types of rock deformation are presented. The relationship between permeability and rock deformation as well as rock failure is also covered.

Chapter 3 covers the experimental methods employed in all the tests with. Data processing and calculation methods are explained. The earlier stage of core preparation including drilling, shaping and saturation of a core is shown. Porosity calculation

method is presented, followed by detailed experimental procedures and mechanical test series designed to achieve the representative stress states.

Experimental results for each core are exhibited in Chapter 4. The chalk mechanical behaviors in each loading cycle are studied and analyzed. In addition, the influences of these behaviors on permeability evolution are noted for further discussion.

A detailed discussion of the observed chalk behaviors and their impact on permeability is conducted in Chapter 5. Explanations and assumptions are made to investigate the results.

The end of this thesis is presented with conclusion remarks in Chapter 6 and recommendations for future work in Chapter 7.

Chapter 2 Literature and Theory Review

Chapter 2 covers a brief overview of the chalk mechanical properties as well as mechanic theories. Chalk is classified as sedimentary rock and the geological processes like subsidence, tectonic forces, precipitation will have a complicated influence on the rock mechanical properties, for instance, the change in the in-situ stresses and pore pressure. The petrophysical characteristics, such as permeability, which is profoundly influenced by mechanical behavior, could also be affected by different factors like the grain size or deformation of the rock.

2.1 Petroleum related geological aspect of chalk

Chalk is a white limestone of Upper Cretaceous and Early Tertiary age (100-61 Ma) with wide distribution in the North West Europe. The Maastrichtian Chalk of North West Europe has been deposited in a seaway covering from the West Atlantic, throughout the North Sea into the east of Poland (Håkansson et al., 1974). The Ekofisk field area is situated in the Central Graben to the south of the North Sea in Norwegian sector of Maastrichtian Chalk (Skovbro et al. 1983). The Ekofisk Chalk Group produced hydrocarbon is the Ekofisk and Tor formaition which are in Danian and Maastrichtian age respectively (Edwin Van den Bark et al. 1981).

The chalk from Ekofisk field is mainly composed of the skeletal remains of coccolithophores that are occasionally found intact but disaggregated into the distinctive, button-shaped grains with less than 20 microns in size (Figure 2.1 is a typical SEM image of outcrop chalk). The porosity of the chalk can reach as high as 70% initially, however, the porosity of chalks will be reduced to 50% due to the mechanical and chemical compaction accompanied with the grain-to-grain framework formation. Chalk with porosity less than 10% at depths over 2000 m is typically encountered under normal pressure areas. Whereas, it is found in the North Sea reservoir areas that the chalk holds porosities of 15-50% because of the overpressured formation at the depths ranging from 2500 to 3500 m. The process of early oil migration with the following reservoir overpressurization caused by the overburden pressure

increase contributes to the high porosity of the chalk reservoir.

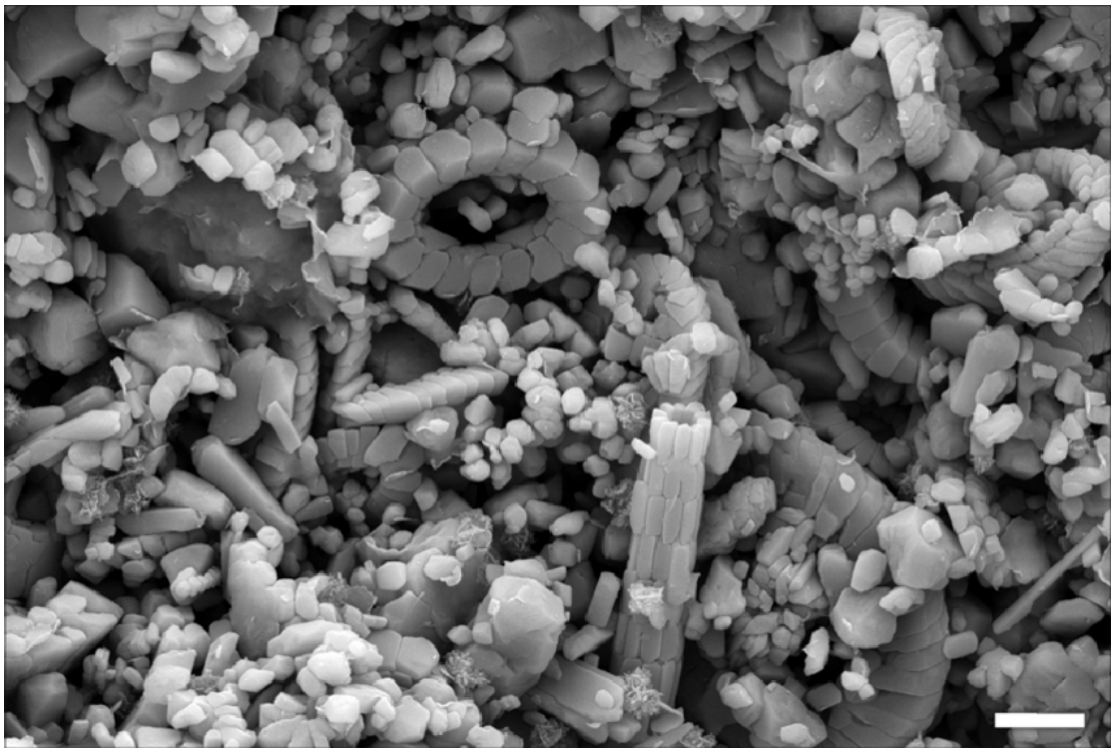

Figure 2.1 SEM image of outcrop chalk (Wang et al., 2016)

The cores taken from the Ekofisk field indicate that the chalk reservoir is naturally fractured, resulting in the reservoir scale permeabilities up to 100 mD despite the fact that the measurements performed in the laboratories demonstrate a permeability range of 0.1 to 10 mD (Thomas et al., 1981). Three major chalk fractures are documented: healed, tectonic and stylolite-associated fractures (Feazel and Farrell, 1988). Due to these natural fracture systems in the chalk reservoirs, the effective porosity of chalk appears much higher compared to the range obtained in the laboratory (Sulak et al., 1989).

2.2 Mechanical concepts and definitions

Rocks under stress will experience deformations from which most of them have the ability to resist or recover. This ability of rock to return to its original shape or size after the removal of applied deforming force is called elasticity. The elasticity of a rock is generally dependent on the stress and strain, whereas, the elastic response of porous rocks may also be dependent on the time. Within the rock elastic response range, strain

is reversible and the rock can return to the original state. However, a permanent change in shape or size may occur when the rock is subject to relatively high stresses and rock failure can be triggered. This rock phenomenon is considered of great importance in the sense that it is the result of inherent property changes as well as the cause of many problems like solids production.

2.2.1 Stress

Stress is the force that acts on a rock unit to change its shape or size causing strain or deformation. Considering a cross section with the perpendicular force F acting on the surface, then the stress σ is defined as

$$\sigma = \frac{F}{A} \tag{2.1}$$

where:

σ	Stress, N/m^2, *Pa or psi*
F	Force, *N*
A	Cross section area, m^2

Rock beneath the Earth's surface can be subjected to several different categories of stress: the lithostatic (overburden) stress or the differential (deviatoric) stress.

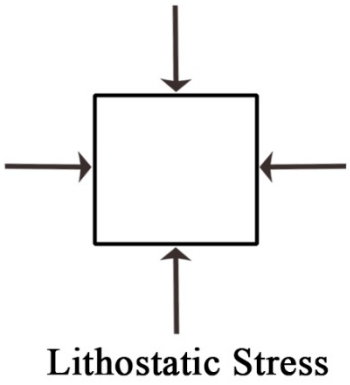

Figure 2.2 Illustration of lithostatic stress

Lithostatic stress illustrated in Figure 2.2, also known as the overburden stress or confining stress, is the equal stress or pressure from all directions imposed on the layer because of the weight of the overlying rock.

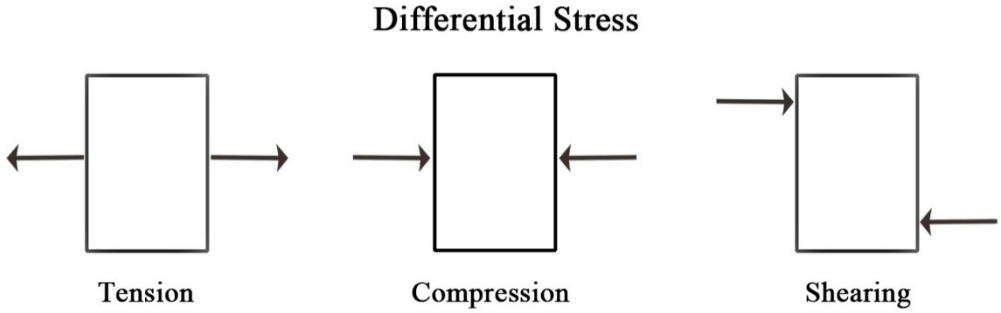

Figure 2.3 Illustration of differential stress

In other cases, rock may experience an additional, unequal stress due to tectonic forces. This stress is called a differential stress illustrated in Figure 2.3. Three kinds of differential stresses can occur: tensional stress, compressional stress and the shear stress. The tensional stress is also called extensional stress which acts normal to the stress area to stretch or lengthen the rock. The compressional stress tends to squeeze the rock with an action of coincident oppositely directed forces normal to the stress area, acting towards each other. Both the tensional and compressional stresses are normal to the plane which can donate normal stress and can be expresses as

$$\sigma_n = \frac{F_n}{A} \tag{2.2}$$

where:

σ_n Normal stress, *N/m^2, Pa or psi*

F_n Normal force component, *N*

The shear stress parallel to the plane may cause slippage and translation because of side-to-side shearing. This kind of stress commonly donates shear stress which can be expresses as

$$\sigma_p = \frac{F_p}{A} \tag{2.3}$$

where:

σ_p Shear stress, *N/m^2, Pa or psi*

F_p Parallel force component, *N*

2.2.2 Effective stress

The distribution of force and the transfer within the rocks is a very complicated scenario which is hard to predict. When the rock is loaded with stress, there is complex interactions between the particles of the rock and the pore fluids present in it. The concept of effective stress is given by Terzaghi (1923) in soil mechanics indicating that the behavior of a soil or a saturated rock rests on the effective stress defined as the difference between total stress and the pore pressure

$$\sigma' = \sigma - P_f \tag{2.4}$$

where:

σ' Effective stress, *N/m^2, Pa or psi*

P_f Pore pressure, *N/m^2, Pa or psi*

This equation was further studied by Skempton (1961) and Biot et al. (1962) with an introduction of a correction factor α, also recognized as Biot's factor or effective stress coefficient, to describe the relation.

$$\sigma' = \sigma - \alpha \cdot P_f \tag{2.5}$$

Study conducted by Handin et al. (1958) concludes that the mechanical properties of rocks are functions of effective stress on condition that the pore fluid is inert and the rocks are sufficiently permeable to allow free movement of pore fluids during deformation so that the pore pressure is able to remain constant and uniform.

Further study of effective stress law was carried out by Teufel and Norman (1990) for chalk experiencing deformation, demonstrating that the effective stress law for deformation is linear and a decrease in α from 1.0 to 0.8 respectively with porosities of chalk sample ranging from 36-15%. Whereas, α is approximately unity for chalks with high porosity.

2.2.3 Strain

With the applied stress on the rock, any deformation in the original shape or volume of an object in response to the stress is called strain. Lithostatic stress causes a rock to change size uniformly in all directions, whereas differential stress induces changes of shape.

Considering a piece of rock under isotropic condition where the response of the rock is independent of the orientation of the applied stress (Figure 2.4). The axial strain induced by stress deformation in the axial direction can be expresses as

$$\varepsilon_{ax} = \frac{L - L'}{L} = -\frac{\Delta L}{L} \tag{2.6}$$

where:

ΔL	Change in length, $m\ or\ ft$
L	Initial length, $m\ or\ ft$
L’	Length after deformation, $m\ or\ ft$
ε_{ax}	Axial strain, $dimensionless$

The radial strain induced by stress deformation in the radial direction can be expressed as

$$\varepsilon_{rad} = \frac{D - D'}{D} = -\frac{\Delta D}{D} \tag{2.7}$$

where:

ΔD	Change in diameter, $m\ or\ ft$
D	Initial diameter, $m\ or\ ft$
D’	Diameter after deformation, $m\ or\ ft$
ε_{rad}	Radial strain, $dimensionless$

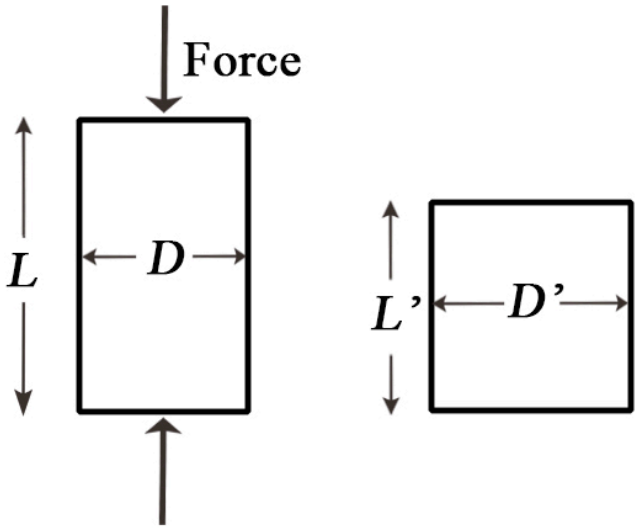

Figure 2.4 Axial and radial deformation

As noted from the general definition of strain, volumetric strain is the change of rock volume after deformation, which is commonly expressed as

$$\varepsilon_{vol} = \frac{V - V'}{V} = -\frac{\Delta V}{V} \tag{2.8}$$

where:

V	Initial volume, $m^3 or\ ft^3$
V'	Volume after deformation, $m^3 or\ ft^3$
ΔV	Change in volume, $m^3 or\ ft^3$
ε_{vol}	Volumetric strain, $dimensionless$

In a triaxial test, assuming that the core keeps a cylindrical geometry during the testing process, then the volumetric strain can be calculated from the axial and radial strain

from equation (2.6) and (2.7) (Nermoen et al, 2015).

$$\varepsilon_v = \varepsilon_{ax} + 2\varepsilon_{rad} + 2\varepsilon_{ax}\varepsilon_{rad} + {\varepsilon_{rad}}^2 + \varepsilon_{ax}{\varepsilon_{rad}}^2 \quad (2.9)$$

2.2.4 Deformation stages

Strain indicates the deformation of rocks subjected to increasing stress. Generally, the rock will experience three successive stages of deformation shown in Figure 2.5.

The first stage is elastic deformation where strain is reversible and the change in shape or size is not permanent. The rock deforms like a spring with small differential stress in this stage. Once the stress is released, the rock would return to its original shape and size.

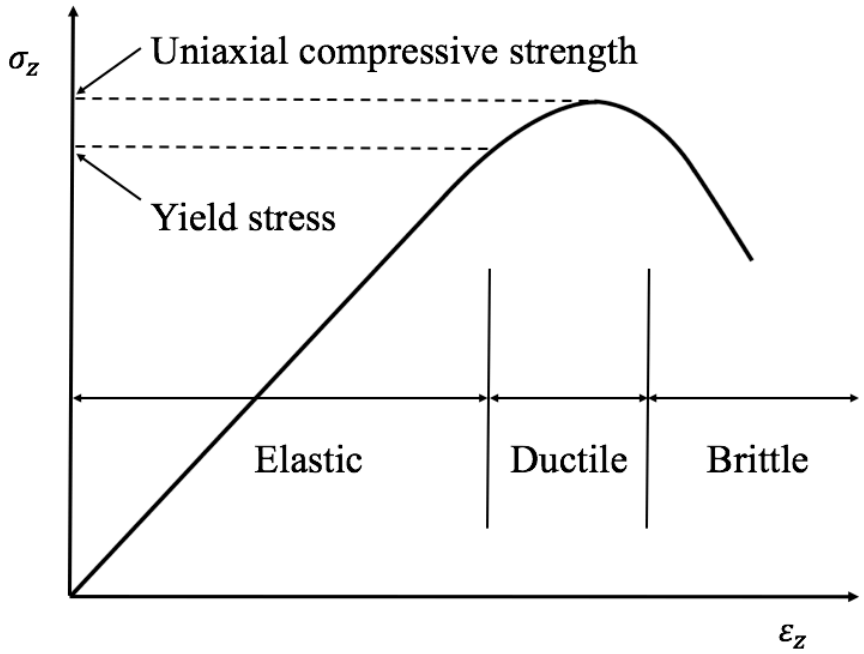

Figure 2.5 Typical stress stain curve during uniaxial or triaxial test

It is demonstrated by Robert Hooke that the relation between stress and strain behaves in a straight line within the elastic deformation model as shown in Figure 2.5 and it can be expressed by using the Hooke's Law

$$\sigma = E * \varepsilon \quad (2.10)$$

where:

ε	Strain, $dimensionless$
E	Young's modulus or Modulus of Elasticity, N/m^2, *Pa or psi*

However, there exists a limit stress known as elastic limit or yield stress beyond which permanent deformation will occur and the rock will no longer go back to its original size and shape.

The second stage is ductile (plastic) deformation (Figure 2.6) where strain is irreversible but the rock still holds the ability to support the load when the stress is released. The tremendous lithostatic stress makes it almost impossible to produce a fracture for rock buried deeper than 10-20 km, but the high temperature can make the rock softer and less brittle. The Rock undergoes plastic deformation when the applied differential stress is higher than the elastic limit. This occurs by the slippage of grains or small groups of grains past each other in the deformation rock, without losing the cohesion of the rock body.

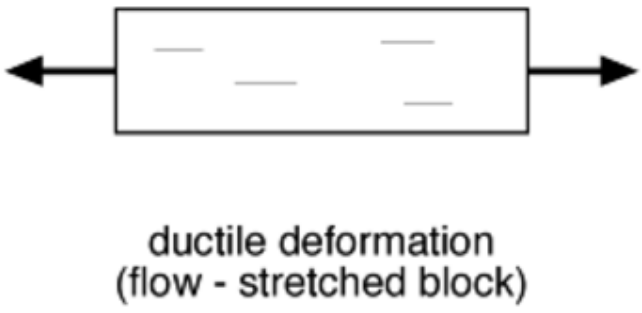

Figure 2.6 Illustration of ductile deformation

The third stage is brittle deformation or fracture (Figure 2.7). The brittle deformation or fracture occurs when the limits of elastic and ductile deformation are exceeded. Due to the loss of cohesion in the rock body under the influence of the deforming stress, rock will be deformed by fracturing or breaking, which usually occurs along the sub-planar Earth's surfaces that separate zones of coherent rock. Commonly the elastic and ductile deformation are exhibited before the ultimate breaking by brittle deformation.

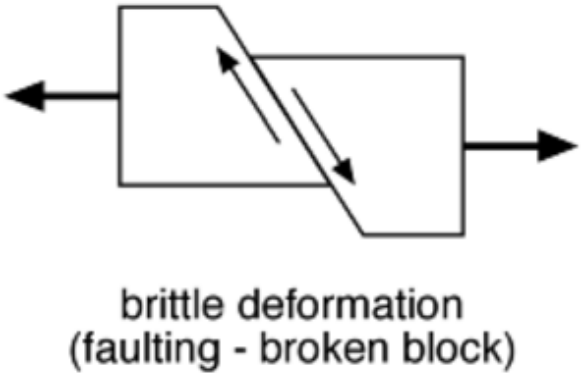

Figure 2.7 Illustration of brittle deformation

Based on the relative behavior of rocks under stresses, rocks can be classified into two categories: ductile rock and brittle rock. The ductile rock is able to deform significantly into the plastic deformation range prior to fracture with a small region of elastic behavior and a large region of ductile behavior. Whereas, brittle material yield very little before cracking and fail suddenly with no significant plastic deformation and low energy absorption. The way that the rock responds to stress is significantly affected by temperature, confining pressure, stain rate and the rock type.

a. **Temperature**. The chemical bonds of the molecules can stretch or move under high temperature, thus the rock results in behaving more ductile. Otherwise, rocks behave more brittle under low temperature.
b. **Confining pressure**. Rocks are less likely to crack or fracture at high confining pressure due to the fact that high pressure will squeeze the rock and hinder the fractures. With low confining stress, rocks tend to be more brittle and are likely to crack sooner.
c. **Strain rate**. Rocks at high strain rate is more likely to fracture. Whereas for rocks at low strain rate, ductile behavior is favored since lower stain rate makes it possible for the rock grains to move and stretch (Bordonaro et al., 1992). The strain in a triaxial test can be calculated by using the equation (2.11).

$$Strain\ Rate = \pm \frac{\varepsilon_{t+\Delta t} - \varepsilon_t}{\Delta t} \tag{2.11}$$

where:

$\varepsilon_{t+\Delta t}$	Strain at time $t + \Delta t, dimenssonless$
ε_t	Strain at time t, $dimensionless$
Δt	Time difference between $t + \Delta t$ and t, $dimensionless$

d. **Rock type**. Mineral compositions vary in different rocks. Minerals like quartz and feldspars are very brittle. Other minerals like mica and calcite are more ductile due to the chemical bonds. The appearance of water in the minerals may weaken the chemical bonds and form films around the mineral grains resulting in slippage. Therefore, wet rocks tend to behave more ductile while the dry rocks tend to behave more brittle (Zhu et al., 1997).

2.2.5 Time-dependent deformation

It is occasionally considered that any change in the applied loading stress will be followed by an instantaneous change in deformation correspondingly. Whereas generally speaking, the change in the applied stress will not result in a change in deformation instantaneously. This observed effect in the rock deformation is known as the time-dependent effect which is commonly divided into two groups: consolidation and creep (Fjær et al., 2008). The change of stress state such as an increase in loading stress may induce a corresponding change in pore pressure, resulting in the pore pressure gradient that caused the consolidation. In this process, the change in the stress load and the corresponding pore pressure strongly rest on the loading rate of the applied stress and sufficient time is needed to re-establish the pore pressure equilibrium.

However, the creep phase of a rock is less dependent on the loading rate compared to consolidation. It is more related to the visco-elastic behavior of the rock. This time-dependent deformation under constant applied load mostly occurs in situation where rocks become stretched, deformed at a given temperature. Creep deformation is commonly divided into three stages (Fjær et al., 2008) as showed in Figure 2.8.

1) **Primary creep or transit creep**. This process starts with a rather rapid rate and slowing down with time.
2) **Secondary creep or steady state creep**. This creep phase has a relatively constant deforming rate. Rocks are not able to return to the original shape even if the stress load is zero indicating a permanent deformation of the rocks.
3) **Tertiary creep or accelerating creep**. Accelerated creep rate is commonly observed in this phase until the rock breaks or fractures. This behavior is generally associated with both necking and formation of grain boundary voids.

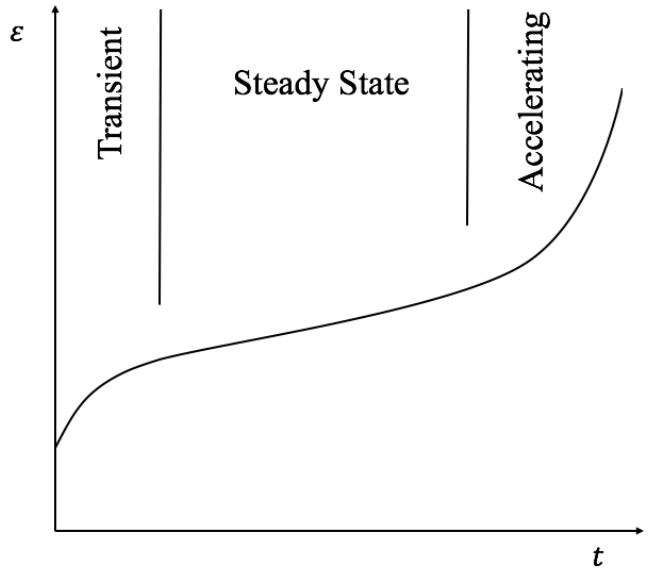

Figure 2.8 Strain versus time in creep phase

2.3 Failure mechanics

It is reported in literatures that rock failures are likely to occur for those subjected to relatively high stress load resulting in the deformation to somewhat extent that changes the rock shape permanently or further causing the rock to fall apart accompanied with loss of ability to support load. Rock failure is generally regarded as the cause of some severe problems such as solids production and bolehole stability. Thus being able to predict under what circumstances the rock is likely to fail will be of great significance.

2.3.1 Strength and laboratory tests

The ability of an object to resist deformation to the stress level where a rock fails is called strength of the rock. Tests commonly used in laboratories to test rock strength are uniaxial and triaxial tests, which can be used to illustrate the complexity of rock failure. Figure 2.9 illustrates a typical specimen used for these two tests with a rule of thumb length to diameter ratio of 2. Pistons above and below can apply stress or pressure to the end faces of the cylindrical specimen while the confining oil surrounding the specimen could provide stress needed to the circumference. Uniaxial stress test is conducted on condition that the confining stress is zero, whereas, triaxial test is performed under non-zero confining pressure.

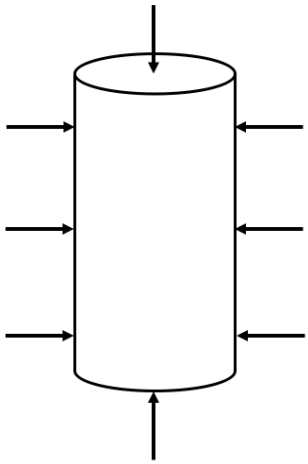

Figure 2.9 Typical test specimen for a uniaxial or triaxial test

2.3.2 Failure mode

The most commonly observed failure mode in a uniaxial or triaxial test is the shear failure mode (Figure 2.10), which occurs when the shear stress is sufficiently high that it exceeds a limit called shear strength.

Another failure mode is known as tensile failure (Figure 2.11), which is caused by excessive tensile stress that exceeds the critical limit called tensile strength (Fjær et al., 2008). Most sedimentary rocks hold a relatively low tensile strength, generally around a few MPa or even less (Lockner 1995). In addition, for rocks with low permeability or

low porosity, the tensile strength does not seem to be dependent on simple effective stress (Zoback, 2007). The tensile failure process is highly localized and inhomogeneous.

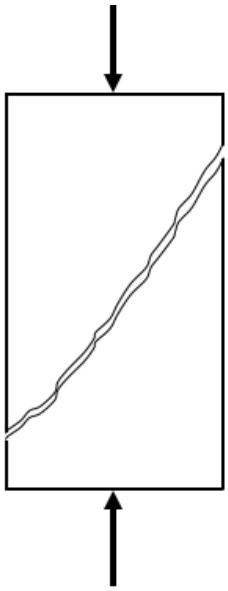

Figure 2.10 Shear Failure

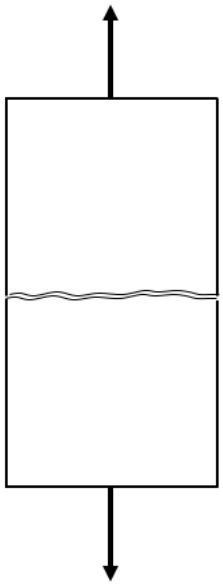

Figure 2.11 Tensile Failure

Another failure mode is called pore collapse or compaction failure appearing mostly in high porosity rocks where relatively open structure is formed by the grain skeleton. Under pure hydrostatic loading, due to the sufficiently high compressive stress from all directions acting on the specimen, pore collapse may occur resulting in splitting of the grain. However, microscopically speaking, the occurrence of pore collapse failure can be caused by the local excessive shear forces acting on the grains and contacts. This failure brings about permanent deformation or damage of the rock framework and can also happen under non-hydrostatic stress conditions which can be observed in triaxial tests under high confining stress.

2.3.3 Failure of Chalk North Sea

Chalk reservoirs in the southern part of the North Sea is thought to have a high porosity around 30-40% and matrix permeability ranging from 1 to 3 mD. Chalks with high porosity is seen to behave mechanically as frictional rocks, falling into the criteria of a shear failure mode. Whereas, the open structures formed by the grain skeleton gives

rise to another failure mode referred as pore collapse. Dasilva et al. (1985) indicating that the strength of chalks varies to great extent which is determined by the porosity and silica content. Chalks with porosity higher than 35% and silica content less than 5% are characterized as weak chalks. Risnes et al. (2000) performed research on the tensile failure in high porosity chalk demonstrates that the tensile strength is strongly dependent on the type of fluids in the pores. A close correspondence between tensile and shear failure is present in high porosity chalks. Laboratory tests carried out by Teufel et al. (1991) suggesting that during the primary production in the Ekofisk field, shear stresses have increased sufficiently to cause pore collapse and shear failure in high porosity chalk reservoirs due to the reduction in pore pressure.

2.4 Permeability measurements

Permeability is the capacity of a porous rock that allows fluids to pass through. The permeability of a rock is generally governed by the porosity, grain shape, capillary pressure and fractures. Over a century, the characteristic of the fluids flow through porous media has been the subject of a large amount of studies.

2.4.1 Darcy's law

A pioneering attempt was made by Darcy in 1856 to explain the fluid behavior in a porous media. Experiments were conducted in laboratory to determine the flow velocity of fluids through a vertical column of sand with known pressure gradient. Therefore, the well-known empirical formula named Darcy's law was derived based on the experiments with an introduction of permeability used to characterize the porous medium:

$$\nu = -\frac{k}{\mu} \cdot \Delta P \tag{2.12}$$

where:

ν Flow rate, *cm/sec*

k Matrix permeability, *darcys*

μ Viscosity, *cP*

ΔP Pressure gradient, *atm*

Assumptions made for the validation of this equation are that the porous medium is homogeneous and isotropic and the fluid flowing through the pores is Newtonian fluid and is chemically inert.

2.4.2 Permeability measurement methods

It is reported in literature that shear failure in chalk reservoirs may account for the continued productivity in Ekofisk field despite the compaction caused by depletion which is supposed to decrease the permeability (Tuefel et at. 1991). Due to the fact that permeability shows the productivity of a reservoir which varies depending on the reservoir geomechanical conditions, therefore, extensive studies have been carried out worldwide to investigate the permeability evolution in simulated reservoir conditions. The two most widely used methods for evaluating permeability are the steady state flow method and the transient pulse method.

For rocks with permeability above 10^{-3} mD (Read et al, 1989), the steady flow method can be used to measure the resulted differential pressure between the inlet and outlet by applying a constant flowrate of fluid flowing through the sample. The results obtained from the experiments can be used to calculate permeability using Darcy's law. In the application of this method, commonly a triaxial cell is needed with a cylindrical core sample connected to the inlet and outlet. Fluid can be flooded from the inlet and out from the outlet, creating a differential pressure in between which can be measured and further used for permeability calculation. If it is assumed that the change in core diameter and length is negligible, then the equation can be expressed as

$$k = \frac{4\mu LQ}{\pi D^2 \Delta P} \tag{2.13}$$

where:

Q	Flow rate, cm^3/sec
D	Diameter of the core sample, cm
L	Length of the core sample, cm

For rocks with relatively low permeability ranging from 10^{-2} to 10^{-9} mD (Read et al, 1989), the transient pulse method can be applied to measure the decay of a small step change of pressure in the sample so as to calculate the permeability by using the pressure decay measured (Brace et al., 1968). This method is based on the theory of one dimensional differential flow of fluid through a porous medium. The diffusion equation of Carslaw and Jaeger (1959) is used to calculate permeability

$$\frac{d^2P}{dx^2} = \frac{\mu BN}{k} \cdot \frac{dP}{dt} \tag{2.14}$$

where:

B	Fluid compressibility, $dimensionless$
N	Effective porosity, $dimensionles$
dP/dx	Pressure gradient, Pa/m
dP/dt	Pressure rate, Pa/s

2.5 Relationship between permeability and deformation

2.5.1 Permeability under compaction

Compaction is the process occurring when the compressive strength of the rock exceeds the limit leading to plastic deformation. This process of the reservoir going through deformation during exploitation generally results in an irreversible reduction of porosity and permeability since the rock is squeezed by the compressive stress

(Menghini et al., 1989, Powell et al., 1994).

Most laboratory experiments measure the stress-dependent permeability under hydrostatic (isotropic) loads. The laboratory experiment conducted by Kilmer et al. (1987) on the low-permeability sandstones indicating that permeability decreases with increasing confining pressure. Under hydrostatic loading with increasing confining pressure the ultimate strength of chalk is increased (Thomas et al., 1981). However, in most reservoirs, deviatoric stress state is more commonly observed than hydrostatic stress state. Permeability reduction induced by shear-enhanced compaction was investigated by Wong et al. (1997) indicating that before the critical stress is attained, the deformation induced by deviatoric stress is elastic with no impact on permeability. Whereas when the critical stress is exceeded, the deviatoric stress will result in inelastic compaction by grain crushing and pore collapse leading to decrease in permeability.

2.5.2 Permeability under shear deformation

The chalk reservoir of Ekofisk field is naturally fractured (Agarwal et al., 1997). Among these, only a minor proportion of fractures that occur mostly in fracture zones with a high fracture intensity will have an influence on stress field (Meling et al., 1993). These fractures are defined as major fractures. Study of permeability change during shear deformation in fractured rock by Teufel (1987) indicating a decrease of permeability across a fracture with increasing shear deformation due to the localized deformation along the fractures and the gouge zone development. Grain size and porosity decrease of the gouge during shear deformation account for the reduction in permeability through the fractures.

Chapter 3 Experimental Methodology

This chapter is presented with detailed description of the experimental methods for core preparation and triaxial cell setup. The successive steps for core preparation will be discussed in 3.1, followed by the preparation of inert NaCl brine in equilibrium with calcite in 3.1.3. Porosity calculations made by using the method of weighing samples before and after saturation is described in 3.1.4. The mechanical tests conducted in the triaxial cell using the prepared samples are described in detail.

3.1 Core sample and brine preparation

It is reported that Kansas chalk contains around 2.5% non-carbonate minerals, i.e. quartz, with porosities in a range of 30-40% and permeabilities ranging from 2 to 5 mD (Tang and Firoozabadi, 2001). For the purpose of investigating permeability changes of Ekofisk chalk reservoirs, upper Cretaceous chalks from Kansas in Niobrara US with similar porosities ranging from 38% to 40% are prepared and tested, based on the fact that these Kansas outcrop chalks corresponding to similar age and properties of the reservoir rock matrix of the North Sea fractured chalk reservoirs.

3.1.1 Core drilling

In order to achieve homogeneous and comparable test samples, cores are drilled in the same direction from the same block of Kansas chalk using the core drilling machine with an oversized bit shown in Figure 3.1. Cold water is used for circulation in the process of drilling and the drilling direction is marked on the core when it is drilled out from the block in order to ensure that the following experiments are conducted in similar orientations. The cored samples are placed in a laboratory oven at 120ºC to dry overnight.

Figure 3.1 Core drilling machine

Figure 3.2 Lache machine

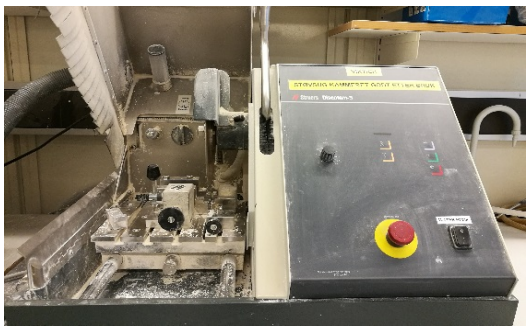

Figure 3.3 Core cutting machine

3.1.2 Core shaping

After the cored samples have been dried in the laboratory oven overnight, the lathe machine shown in Figure 3.2 is used to shape the diameter of the cores. A typical diameter for cores in the petroleum application is 38 mm (1 ½'') (Fjaer et al., 2008). Therefore, the cores used in this work are machined to 38.1 (±2%) mm respectively. Afterwards, these machined cores are cut using a diamond saw displayed in Figure 3.3 to the length approximately twice the diameter, a general rule of thumb in petroleum application (Fjaer et al., 2008). When this process is finished, the cores are put back again into the laboratory oven to dry overnight at 120ºC for further porosity measurements.

3.1.3 Fluids

An inert NaCl brine in equilibrium with calcite is used in this thesis for flooding. Distilled water (D.W.) is used for saturating the core samples. Before the preparation of brine, distilled water in equilibrium with calcite is prepared with a concentration of 0.002 mol/L (0.2 g/l) calcite. Afterwards, the milipore filtration apparatus (Figure 3.4)

is employed to remove the undissolved impurities by using the 0.65 μm filtrate paper. The pH of the calcite equilibrium water is measured before proceeding to the preparation of NaCl brine in equilibrium with calcite.

The NaCl brine used for the following experiments holds a concentration of 0.657 M (the concentration and ionic strength of the brine is listed in Table 3.1). In the preparation of the brine, 38.4 g Sodium Chloride (NaCl) is added into the pre-prepared calcite equilibrium water in a 1 L volumetric flask. The fluid is left to be mixed thoroughly using the magnetic stirrer before the initiation of the next step. After minimum 1 hour of mixing, the brine is transferred to the filtration apparatus (Figure 3.4) for filtrating. The pH of the NaCl brine is measured after the filtration step and a pH value above 7 should be guaranteed.

Table 3.1 Concentration and Ionic strength of NaCl brine

Ion	***Concentration*** (mol/L)
Na^+	0.657
Cl^-	0.657
Ionic strength	***0.657***

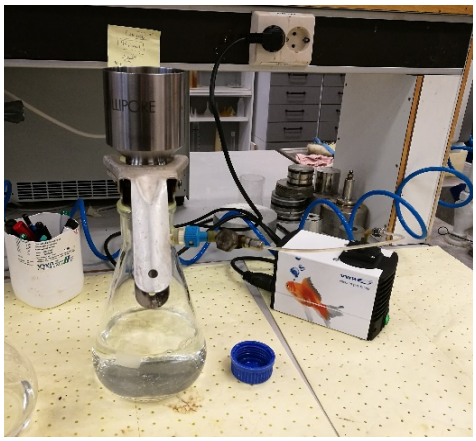

Figure 3.4 Filtration apparatus

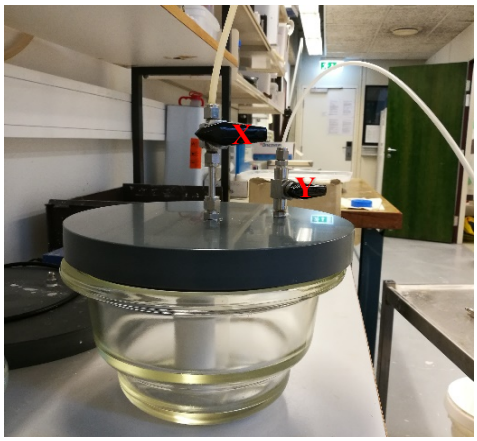

Figure 3.5 Vacuum apparatus

3.1.4 Core saturation

Cores are generally saturated before performing the further mechanical tests. In this work, the pre-dried cores are put into a vacuum chamber (Figure 3.5) to be saturated

with distilled water following the steps listed below:

1) The core is placed into the chamber with an O-ring and lid on top for sealing.
2) The valve (marked X on Figure 3.5) connecting to the atmosphere is then closed before opening the valve (marked Y on Figure 3.5) connecting the chamber to the vacuum pump.
3) Pump speed gear is switched to II to start vacuuming. The speed gear is changed from II to I and then to 0 respectively with a vacuuming time interval of 10-15 minutes at each speed.
4) When the chamber is appropriately vacuumed with inner pressure 4-5 Pa lower than the atmospheric pressure, the tube connecting the chamber and D.W. container is pre-flushed and then connected to the chamber.
5) The valve X is then opened until the water completely covers the core and the core is left for saturation for minimum 1 hour.

3.1.5 Porosity calculation

The porosities of the cores are measured and calculated by using the pore volume and fluid saturation method:

1) The length (L) and diameter (D) of the pre-dried core is measured for calculation of the bulk volume (V_b).

$$V_b = \frac{1}{4}\pi D^2 L \tag{3.1}$$

2) The weight of the core before (W_{dry}) and after saturation (W_{sat}) is measured in order to calculate the pore volume (V_p) since the density of the distilled water (ρ_{wtr}) is considered to be 1.0 g/cm^3. The pore volume can be calculated by using the equation (3.2).

$$V_p = \frac{W_{sat} - W_{dry}}{\rho_{wtr}} \tag{3.2}$$

3) Then, the porosity (φ) is calculated by

$$\varphi = \frac{V_p}{V_b} \tag{3.3}$$

The properties of the chalk cores used in this thesis are calculated and given in Table 3.2 below.

Table 3.2 Properties of the cores

Sample No.	***D*** **(mm)**	***L*** **(mm)**	W_{dry} **(g)**	W_{sat} **(g)**	V_b **(cm^3)**	V_p **(cm^3)**	φ **(%)**
K5	38.09	71.91	134.95	166.89	81.94	31.94	38.98
K6	38.09	72.94	137.79	169.90	83.11	32.11	38.63
K9	38.08	73.09	138.67	170.67	83.24	32.00	38.44
K10	38.09	72.57	135.76	168.25	82.69	32.49	39.29
K11	38.09	72.41	136.92	168.84	82.51	31.92	38.69
K12	38.09	73.57	138.88	171.39	83.83	32.51	38.78
K16	38.08	71.57	133.88	165.87	81.51	31.99	39.25
K19	38.09	70.85	133.59	164.76	80.73	31.17	38.61
K20	38.09	71.29	133.47	165.30	81.23	31.83	39.18
K24	38.09	72.46	135.57	167.87	82.57	32.30	39.12

3.2 Test equipment

All the mechanical experiments of this thesis are carried out in the triaxial cell schematically illustrated in Figure 3.6. The triaxial cell is equipped with three pumps to regulate pressure in the axial and radial directions as well as the flowrate. Changes of stress states are achieved by applying different test sequences.

3.2.1 Triaxial test cell

The standard triaxial test cell is the main test equipment operated hydraulically by three high-pressure piston pumps for pressure control. Typically, the test core is mounted between the upper and lower steel cylinders marked X and X on Figure 3.6. A heating skirt surrounding the core in the middle makes up the confining chamber and it can also be used to increase the temperature as required. The mounted core is separated from the confining fluid in the confining chamber by applying shrinking sleeve. Fluid is flooded from the inlet (upstream pore line) through the core and discharged from the outlet (downstream pore line). The top with piston chambers and piston assembling is placed on top of the heating skirt to complete the pressure vessel.

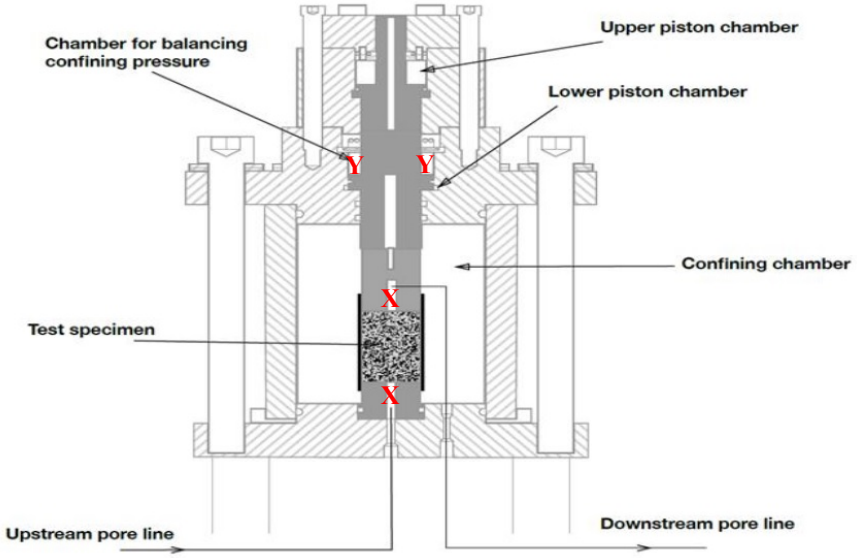

Figure 3.6 Triaxial cell Illustration (Kjørslevik and østensen, 2014)

The fluid inside the confining chamber is used to apply confining stress load. However, due to the design that the fluid in the confining chamber can move up into the chamber marked Y on Figure 3.6 to balance the confining pressure, therefore, when the confining stress load is applied, it applies both radially and axially. Additional axial load can be applied by the hydraulically operated piston assembling. The piston will be pushed down on condition that the pressure in the upper piston chamber is higher than that in the lower piston chamber, and the same way around for lifting up the piston. The piston friction caused during applying additional axial load is generally measured before

starting the experiment.

During the experiment, the deformation of the core is measured in two ways. A circumferential extensometer connected to a chain surrounding the middle of the core is used to measure the diameter during the test process, recording the expansion or contraction of the core in the radial direction. The axial movement is measured by the Liner Variable Displacement Transducer (LVDT) placed on top of the piston assembling, following the movement of the piston during the deformation of the core. The flooding rate for the injected brine sets up a differential pressure that is measured and used to calculate the permeability of the core.

3.2.2 Pumps

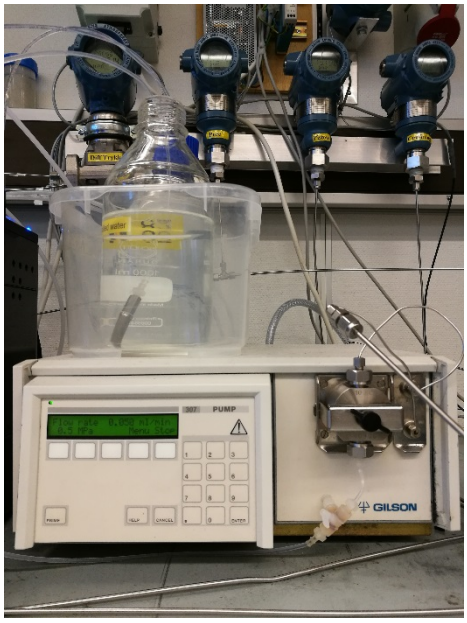

Figure 3.7 Gilson pump

Figure 3.8 Quizix pump

In order to regulate axial pressure (σ_{ax}) and radial pressure (σ_{rad}) as well as fluid flowrate (Q), two different kinds of pump setups are used in this thesis. The Gilson Pump (Model 307 HPLC) in Figure 3.7 is used to control the flowrate. This pump is connected to the upstream pore line for fluid injection noted on Figure 3.6. The other two pumps shown in Figure 3.8 are the Quizix Pump (Model QX-20000 HC) for regulating the axial pressure and confining pressure. The experimental setup allows an independent control of different pressures and stresses by operating the pumps

individually. The Quizix Pump is operated by the Vindum Pump Program, which is specially set up for this experiment.

3.2.3 Heating system

A proper heating system is of great necessity since the experiments in this thesis are all carried out at the temperature of 50ºC. The heating jacket making up the confining chamber of the triaxial cell is used for heating. The temperature inside the cell is measured by a Pt-100 (Resistance Temperature Detector) and the heating process is controlled by an external regulating system (Omron E5CN) to ensure stable temperature readings.

3.2.4 Pressure and temperature measurements

Pore pressure is applied by using the back pressure regulator (BPR-system) exhibited in Figure 3.9. One side of the system is connected to the downstream pore line and the other side is connected to a gas line for applying pressure as well as the maintenance of stable pore pressure ($\pm$0.1MPa). The piston and confining pressure along with pore pressure, differential pressure and test temperature are measured by the digital pressure gauges manufactured by Emerson Rosemount (Figure 3.10). The LabView (Laboratory Vitual Instrument Engineering Workbench) program is used to record the measurements, and also acts as a tool for monitoring, controlling parameters like flooding rate and recording time intervals.

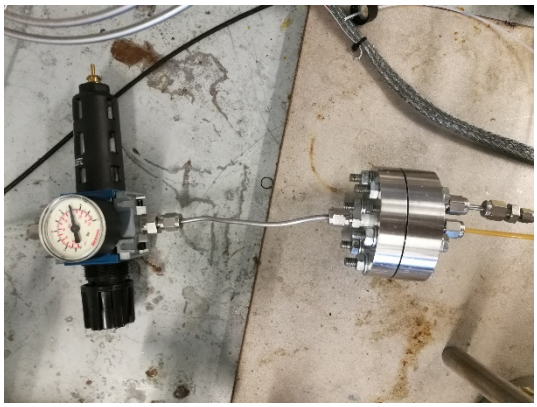

Figure 3.9 Back pressure regulator

Figure 3.10 Gauges

3.3 Hydrostatic and deviatoric test

Both hydrostatic and deviatoric tests are performed in the experiments with different sequences in order to simulate different stress states for investigating the permeability evolution.

3.3.1 Hydrostatic loading

Hydrostatic loading is where the core is exposed to an increasing equal stress load from all directions acting to squeeze the sample. By using the triaxial cell illustrated in Figure 3.6, the hydrostatic loading test is performed with increasing confining pressure controlled by the confining pump. A loading rate of 0.1 mL/min is applied in this thesis. Any deformation, i.e. change in the diameter and length of the sample, is recorded with the change in differential pressure. With the deformation in the axial direction during loading phase, the piston assembling is likely to experience friction while moving downward corresponding to the loading process, therefore, in order to overcome this friction during the experiment, an additional axial load around 1.2-1.8 MPa is applied during loading in this thesis work.

3.3.2 Deviatoric loading

Deviatoric loading is where the core is exposed to an increasing stress load from the axial direction and constant confining stress. By using the piston pump in Figure 3.7, the pressure applied on the piston assembling can be regulated during the deviatoric loading phase. In this loading phase, the core is more likely to experience shear failure, which could contribute to the continued productivity of chalk reservoir (Teufel et al., 1991). All the deviatoric loading tests in this thesis are conducted under a constant loading rate of 0.01 mL/min.

3.3.3 Creep phase

The creep phase is followed by the hydrostatic or deviatoric loading where the core

experiences deformation under a constant stress load. For further analysis, the deformation in the axial and radial direction are measured and recorded along with changes in differential pressure.

3.4 Test series

The laboratory experiments are carried out in five test series. Under each test series, at least two experiments are performed in order to check repeatability. Any change in permeability will be monitored and recorded during all the sequences in the test series.

Test Series 1. In this series, two reference mechanical tests are conducted to investigate the mechanical strength and permeability evolution during the hydrostatic loading. The core is loaded hydrostatically above yield strength and then is left to creep for 1-3 days.

Test Series 2. In this test series, the core is firstly loaded hydrostatically up to 3 MPa confining pressure. Afterwards, two deviatoric loadings are conducted at constant 3 MPa confining pressure.

1) **1st Deviatoric Loading and Creep Phase**. The 1st deviatoric loading is performed until a peak axial stress. After that, a fixed piston pressure is set for the core to creep.
2) **Unloading**. After the 1st creep phase, the piston pressure is unloaded back to 0.7 MPa with the ramping time same as the loading time in step 1). Core is left to rest after unloading.
3) **2nd Deviatoric Loading and Creep Phase**. The 2nd deviatoric loading is performed until a peak axial stress. After that, a fixed piston pressure is set for the core to creep.
4) **Unloading**. The piston pressure is unloaded back to 0.7 MPa and the core is left to rest.
5) **3rd Deviatoric Loading and Creep Phase**.

Test Series 3. In this test series, cores are firstly loaded hydrostatically to 3 MPa confining pressure. Two deviatoric loadings and one hydrostatic loading is performed

in this series.

1) **1st Deviatori Loading and Creep Phase**. The 1st deviatoric loading is performed until a peak axial stress, and after that, a fixed piston pressure is set for the core to creep.
2) **Unloading**.
3) **1st Hydrostatic Loading and Creep Phase**. A hydrostatic loading is performed above yield. After that, the core is left to creep at a constant confining pressure.
4) **Unloading**.
5) **2nd Deviatoric Loading and Creep Phase**.

Test Series 4. Two mechanical experiments are conducted in this test series with constant confining pressure maintained at 1.2 MPa during loading and unloading. Except for the difference in the confining pressure, the rest of the test procedures are the same as the ones in test series 2.

Test Series 5. Two mechanical experiments are conducted in this test series with the same procedure described in test series 3, except that the core is firstly loaded hydrostatically until 1.2 MPa confining pressure and the deviatoric loadings are conducted at a constant confining pressure of 1.2 MPa.

3.5 Test Procedures

Before initiating experiment in the triaxial cell for each series, Kansas chalk cores are saturated with distilled water as described in 3.1.4. All the tests conducted in this thesis are at 50ºC and 0.7 MPa (±0.05MPa) pore pressure with continuous flow of NaCl brine with a flooding rate of 0.05 mL/min.

3.5.1 Triaxial test cell setup

Initially, 0.657 M NaCl brine is pumped into the test system for flushing and filling all the lines with brine in order to avoid air existence in the tubes. Afterwards, filtrate paper and drainage disk is placed respectively on the steel cylinder in the base (Figure 3.11)

to ensure the flow of fluid is evenly distributed across the circumference cross-section of the core.

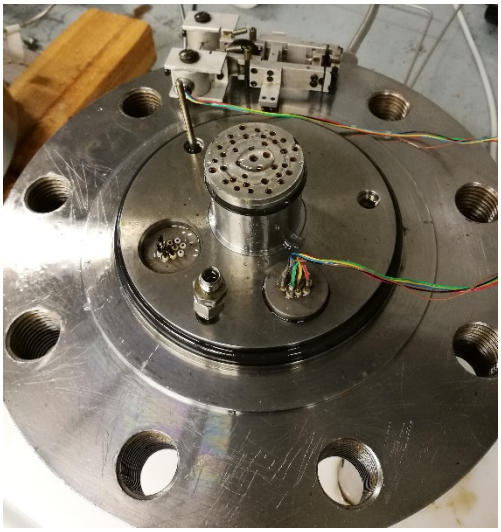

Figure 3.11 Core mounting process (a)

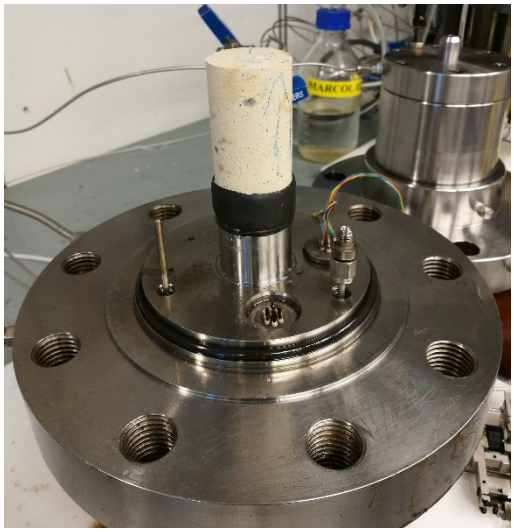

Figure 3.12 Core mounting process (b)

Before putting the core on top of the drainage disk, a specially polished rubber is placed in connection with the steel cylinder (above the O-ring) and the core with an intention to provide additional stabilization and sealing of the core besides the shrinking sleeve. After the completion of step exhibited in Figure 3.12, the other drainage disk, filtrate paper and a rubber seal are placed on the other side of the core. A thin layer of silicone grease is applied below the O-ring in the base cylinder and above the O-ring in the upper cylinder for the purpose of easier removal of the core during dismantle and preventing leakage.

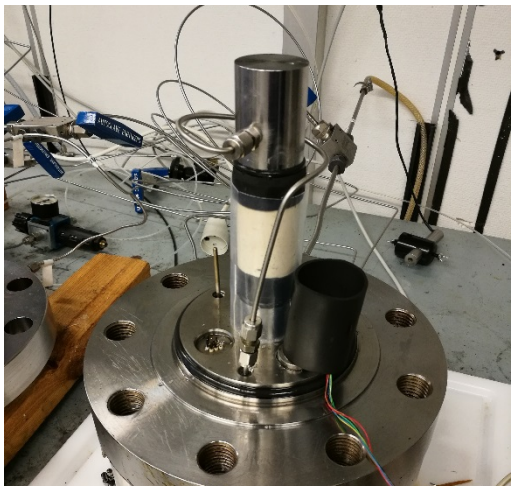

Figure 3.13 Core mounting process (c)

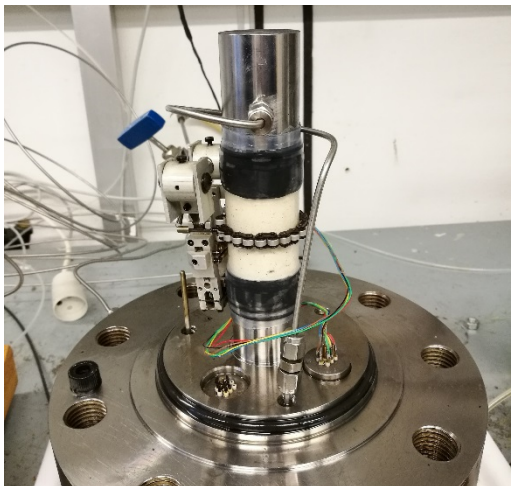

Figure 3.14 Core mounting process (d)

After this step, a shrinking sleeve covering both robber seals are placed around the core and the upper steel cylinder is placed on top of the drainage disk. Before softening the shrinking sleeve to jacket around the core, a rubber shown in Figure 3.13 is placed to cover the wires to avoid damage during the process of heating the shrinking sleeve. With the protection rubber in place, a heating gun is employed to heat and soften the shrinking sleeve so as to make it closer to the core and jacket around it to prevent the confining oil from entering as well as to stabilize the assembling. The following step is to connect the tube linking the upper steel cylinder to the downstream pore line so that fluid can flow through this tube by opening the bypass for building up pore pressure. The chain placed around the middle of the core is connected to an extensometer (Figure 3.14) for measuring the change in the radial direction.

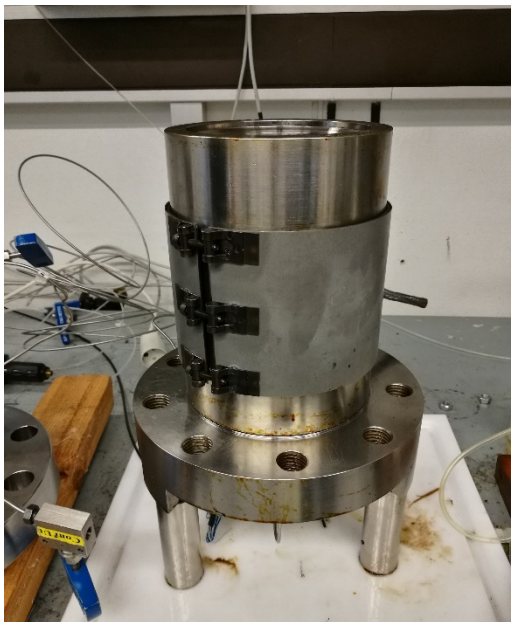

Figure 3.15 Core mounting process (e)

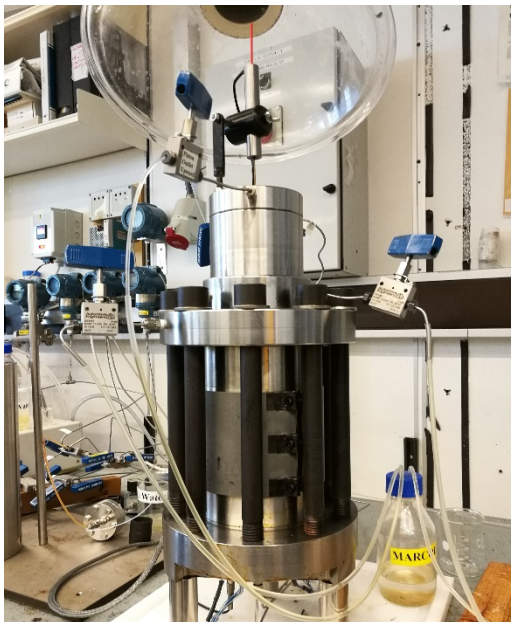

Figure 3.16 Core mounting process (f)

After the completion of these two steps, the heating skirt is ready to be put onto the base to make up the confining chamber (Figure 3.15). Before adding Marcol 82 oil into the confining chamber, the drainage valve should be closed. After the confining chamber is filled with oil, the top part of the triaxial cell is placed on top of the heating skirt with confining valve open and further aligned to insert the bolts shown in Figure 3.16. In the following process, a torque gun is employed with additional 200 mN torque to tighten the nine bolts placed in between the top and base, in order to seal the confining chamber. The last step for setting up the triaxial test cell is to place in the

LVDT for detecting changes in the axial direction and make sure that the transducer can move freely along the direction of the piston movement during the testing process.

3.5.2 Increasing confining pressure

Confining pressure inside the cell should be increased up to 0.5 MPa prior to flooding the brine into the system. The valve of the confining outlet marked (X) on Figure 3.17 should stay open in the beginning of the pressure build-up to avoid air existence inside the chamber. The oil is pumped from pump 2 (Figure 3.17) through the tubes to the confining pressure chamber and out from the confining outlet until constant dripping of oil is observed. The confining outlet valve should then be closed. The pump rate is lowered to constant 0.5 mL/min after closing the outlet valve. Pump mode is changed to maintain constant 0.5 MPa pressure after the confining pressure reaches 0.5 MPa.

3.5.3 Flooding brine

After the confining pressure have reached 0.5 MPa, the core is left to rest for some time before initiating flooding the brine. The purpose of this step is to displace the distilled water inside the pore spaces into desired NaCl brine.

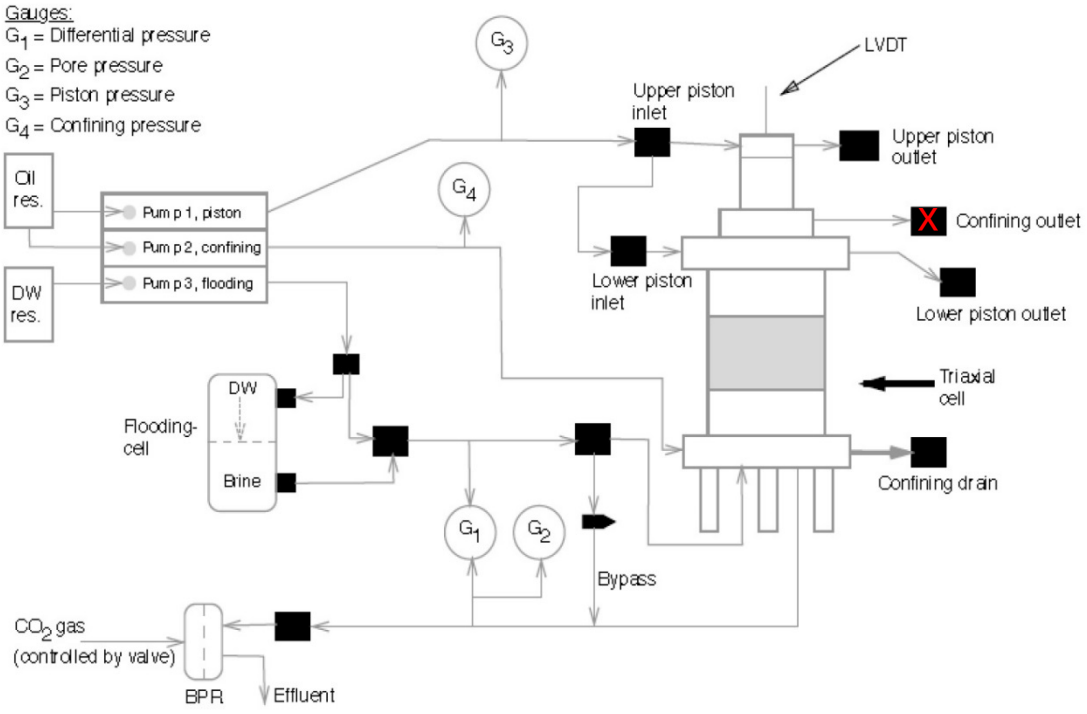

Figure 3.17 Illustration of experimental set-up (Kjørslevik and østensen, 2014)

As illustrated on Figure 3.17, distilled water is pumped from the container by pump 3, Gilson Pump, through the tubes to the upstream pore line, which is the inlet of the triaxial cell, flowing into the core sample and squeezing the previous fluid inside the pores out from the downstream pore line to the outlet. The pump operates at a constant pumping speed of 0.2 mL/min throughout the displacing process until the differential pressure measured between the inlet and outlet stabilizes. After the stabilization, pumping speed is lowered to 0.05 mL/min and experiment is proceeded until the differential pressure is stabilized.

3.5.4 Building up pore pressure

The pore pressure build-up process is initiated after the stabilization of differential pressure. The ultimate goal in this process is to build up the pore pressure to 0.7 MPa. In the meantime, the pumping speed of the confining pump and Gilson Pump is adjusted so that the confining pressure is increased simultaneously with the pore pressure with an almost constant difference of 0.5 MPa between the confining and pore pressure. Prior to start, the back pressure regulator is set to 0.7 MPa and the bypass is opened in order to speed up this process. After opening the bypass, flooding rate is increased to 2 mL/min and gradually following the successive decrease in the sequence of 1mL/min, 0.5 mL/min, 0.1 mL/min, 0.05 mL/min until the pore pressure reaches 0.7 MPa and confining pressure comes to 1.2 MPa. The bypass valve is then closed.

3.5.5 Increasing temperature

Heating process is started after the pore pressure stabilizes around 0.7 MPa and differential pressure is stabilized. Before increasing the temperature, the PID values are required to be set for the desired temperature of the experiment so as to control the heating process and maintain stable temperature at 50ºC throughout the experiment. An additional spring release valve which can stand pressure up to 20 MPa is connected to the confining outlet marked (X) in Figure 3.17 for regulating the confining pressure during the heating process due to the fact that oil will tend to expand when temperature increases, which will in turn increase the confining pressure in the sealed chamber. When the heating process is started, confining pump should be turned off and the

confining outlet valve has to be open. The confining pressure is controlled by the spring release valve throughout the process until the temperature is increased to a point that any adjustment in the spring cannot make a difference in the confining pressure. The confining outlet valve is therefore closed and the pump is turned back on to maintain constant pressure. After the temperature reaches 50ºC, the core is left to rest for some time before the differential pressure starts to stabilize and the temperature of the whole system becomes 50ºC with no temperature difference gradient.

3.5.5 Pushing down piston

When the differential pressure is fully stabilized and the temperature is evenly distributed, the next step is to push down the piston by applying pressure on the piston assembling using the pump 1 illustrated in Figure 3.17.

Prior to initiating the process, it is required to close the valve of lower piston inlet, and open the valve of upper piston and lower piston outlet as well as upper piston inlet. Piston pump 1 (Figure 3.17) is employed to apply pressure load on the piston assembling to push the piston down. The upper piston outlet valve should stay open in the beginning of the process until constant dripping of oil is observed with the intention to avoid air existence inside the piston chamber. The pump speed is lowered to 0.5 mL/min before closing the upper piston outlet valve. In order to ensure soft landing of the piston onto the core, the pump speed is lowered to 0.2 mL/min when the piston is about to hit the core. It is necessary to apply an additional 0.3 MPa piston pressure when the piston hits the core so as to make sure that the piston is landed on the core. However, the piston pressure should not exceed 0.7 MPa.

In all the experiments carried out in this thesis, the piston pressure is set to be 0.7 MPa after hitting the core. The core samples are left to rest for some time until the differential pressure reaches stabilization.

3.5.6 Permeability evolution tests

After the completion of the previous steps, the core is ready for the permeability

evolution tests performed accordingly as described in test series.

In total, ten cores with similar porosities in the range of 38-40% are used for the five test series in this thesis. The flow rate is kept constant at 0.05 mL/min and the deformation in the radial as well as axial directions are measured and recorded for further calculation and interpretation.

3.5.7 Dismantle of triaxial test setup

The flooding fluid is switched to distilled water at the end of the permeability evolution test in order to clean the core before dismantling. At least one pore volume of distilled water should be flooded through the core. Heating program is stopped before the initiation of flooding distilled water.

When the temperature is lowered to a desired value and the core is sufficiently clean enough, the piston will be moved up by pumping oil to the lower piston chamber. The Gilson pump is turned off and pore pressure is taken down before decreasing the confining pressure. The confining outlet valve is opened gently and slowly during the confining pressure release. When the confining pressure drops to zero, the drainage valve should be open and compressed air is used to squeeze out the oil inside the confining chamber. Afterwards, the core is taken out and dried.

3.6 Data processing

After the completion of the experimental work, the result data are processed. Effective confining and axial stress, as well as axial, radial and volumetric strain are calculated and employed to interpret the deformation of the core during different phases. Permeability is calculated by using the equation of Darcy's Law with a small modification in order to achieve better accuracy.

The effective confining stress (σ'_{conf}) is calculated from the confining pressure (σ_{conf}) and pore pressure (P_{pore}) by equation (2.4) in Chapter 2.

$$\sigma'_{conf} = \sigma_{conf} - P_{pore} \tag{3.1}$$

For core under constant confining pressure, the stress load is applied from all directions. If an additional axial stress is applied, then the stress in the axial direction (σ_{ax}) is calculated from the confining pressure (σ_{conf}), piston pressure (P_{pist}), friction pressure (P_{fric}) and an area factor (f_{area}) (Nermoen et al., 2015).

$$\sigma'_{ax} = \sigma_{conf} + f_{area} * \left(P_{pist} - P_{fric}\right) - P_{pore} \tag{3.2}$$

where $\sigma_{ax}{}'$ is the effective axial stress. The value of area factor (f_{area}) for the piston chamber is given as 1.27 (dimensionless). The piston friction (P_{fric}) within the triaxial cell is given as 0.4 MPa.

The axial strain (ε_{ax}), radial strain (ε_{rad}) and volumetric strain ((ε_{vol}) can be calculated by using equation (2.6), (2.7), (2.9) provided in Chapter 2.

The original equation of Darcy's Law is give in in Chapter 2 equation (2.12) with fixed value of diameter and length. However, the real situation for core undergoing deformation is that changes in both length and diameter are expected. The core length at all times during the experiments can be express as

$$L_{real} = L_{ini} + \Delta L \tag{3.3}$$

where L_{ini} is the initial length of the core, ΔL can be calculated from the change measured by LVDT and L_{real} is the length at the exact time that is used for the calculation.

Two cases need to be taken into account regarding the determination of the diameter at all times during deformation. For core under deviatoric loading, the tendency of the radial deformation is expansion, whereas, in hydrostatic loading, the tendency is radial contraction. Both circumstances are illustrated in Figure 3.18 and 3.19.

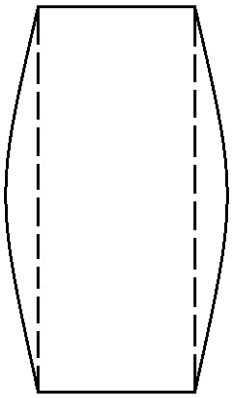

Figure 3.18 Diameter change during deviatoric loading

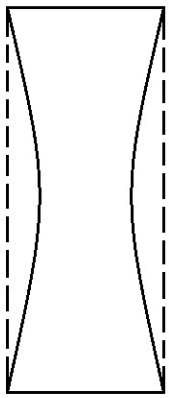

Figure 3.19 Diameter change during hydrostatic loading

As illustrated in Figure 3.18 and 3.19, if the change in core diameter is assumed to be a circular arc, thus, a simple estimation of the average change in diameter is calculated based on the extensometer measurements. The diameter at any time (D_{real}) during deformation can be expressed as

$$D_{real} = D_{ini} + \Delta D/2 \tag{3.4}$$

where D_{ini} is the initial diameter. ΔD is the difference between the value measured by extensometer at any time and in the beginning.

Based on these assumptions and estimations, the modified equation of Darcy's Law for calculating permeability can be expressed in equation (3.5) and this equation is used for the permeability calculation in this thesis.

$$k = \frac{4\mu L_{real} Q}{\pi {D_{real}}^2 \Delta P} = \frac{4\mu * (L_{ini} + \Delta L) * Q}{\pi * (D_{ini} + \frac{\Delta D}{2})^2 * \Delta P} \tag{3.5}$$

By using a brine density and viscosity calculator (Ettouny et al., 2002), the viscosity of the NaCl brine at 50ºC with a concentration of 0.657 M can be calculated. The dynamic viscosity is calculated to be 0.6 cP, which will be used in equation (3.5) for calculating permeability.

Chapter 4 Experimental Results

4.1 Test series 1

The porosities for sample K5 and K12 are respectively 38.98% and 38.78%. Both cores are firstly loaded hydrostatically above yield strength, and then followed by a deviatoric loading performed at 3 MPa confining pressure. Test series 1 will be used as a reference test for the interpretations and discussions of experimental results. Test schemes for the loading cycles are listed in Table 4.1.

Table 4.1 Test schemes for Core sample K5 and K12

Loading Cycle	***Confining Pressure (MPa)***		***Piston Pressure (MPa)***		***Creep Time (Days)***	
	K5	***K12***	***K5***	***K12***	***K5***	***K12***
1st HL	19.3 Max.	19.3 Max.	1.8 Max.	1.5 Max.	/	/
1st HC	19.3	19.3	1.8	1.5	0.9	2.8
1st DL	3.0	3.0	8.1 Max.	8.6 Max.	/	/
1st DC	3.0	3.0	7.8	7.6	0.04	0.02

**HL=Hydrostatic Loading, HC=Hydrostatic Creep, DL=Deviatoric Loading, DC=Deviatoric Creep.*

**Max.=Maximum*

4.1.1 Results

1st Hydrostatic Loading Phase. Both cores are loaded hydrostatically above yield strength to 19.3 MPa confining pressure as a reference for further experiments. The yield strength is identified while the stress-strain curve starts to deviate from the straight line on Figure 4.1.

Figure 4.1 shows that the initial permeability before increasing confining stress is just above 2 mD. With an increase in applied confining pressure, continuous decrease in permeability is observed throughout the loading process with a reduction factor of 2. This phenomenon is commonly observed with increasing overburden stress. The curve

of the hydrostatic compaction has a typical shape of sigmoidal function (David et al.,1994). After an axial strain of 0.82%, the two permeability-strain curves tend to converge at permeability of 0.89 mD.

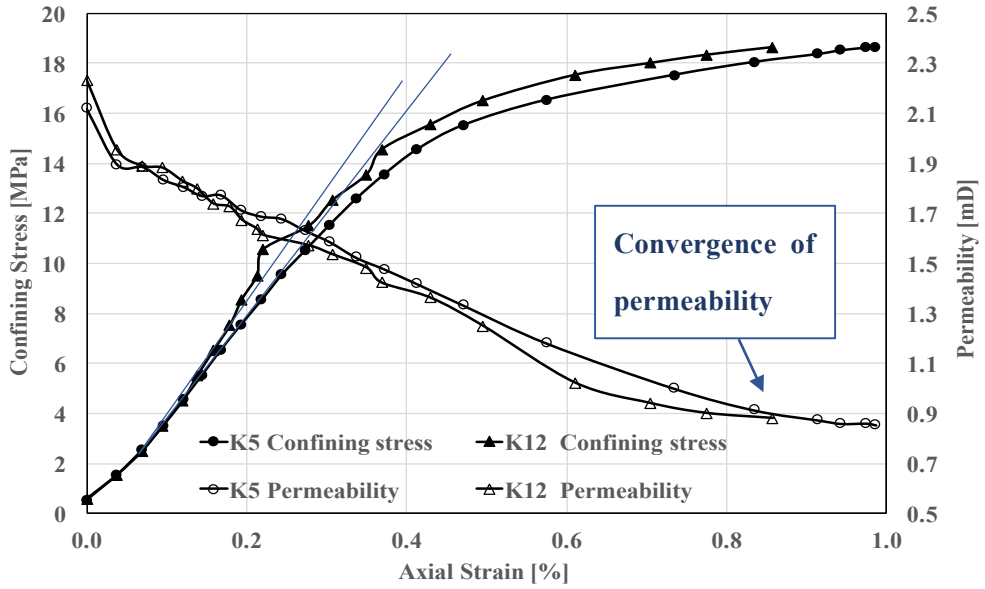

Figure 4.1 Hydrostatic loading for core K12 & K5 until 19.3 MPa confining pressure

1st Creep Phase. After the completion of the hydrostatic loading, K5 and K12 are left to creep under 19.3 MPa confining pressure for 0.9 and 2.8 days respectively.

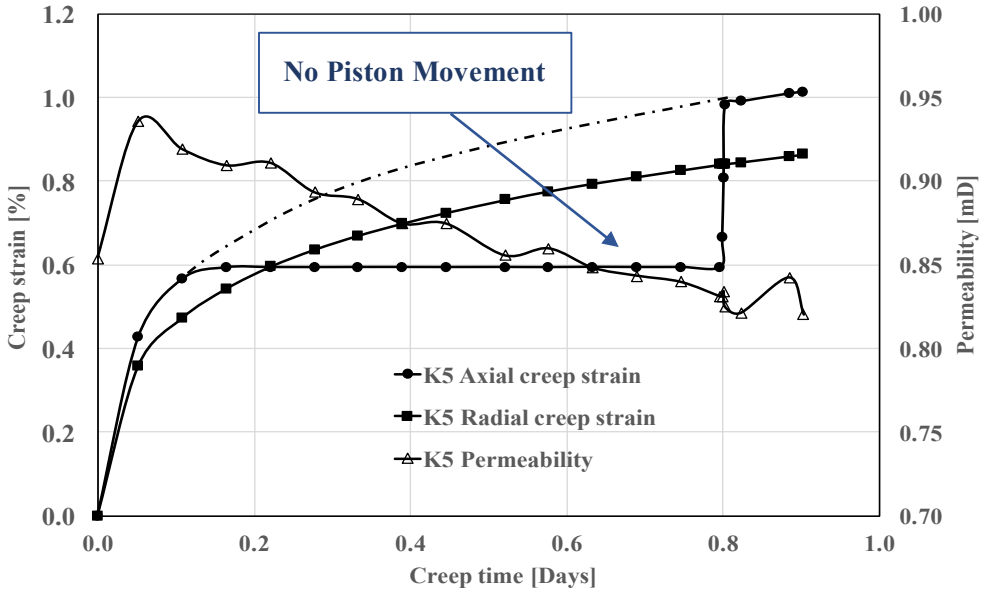

Figure 4.2 1st Creep phase for core K5 at 3 MPa confining pressure

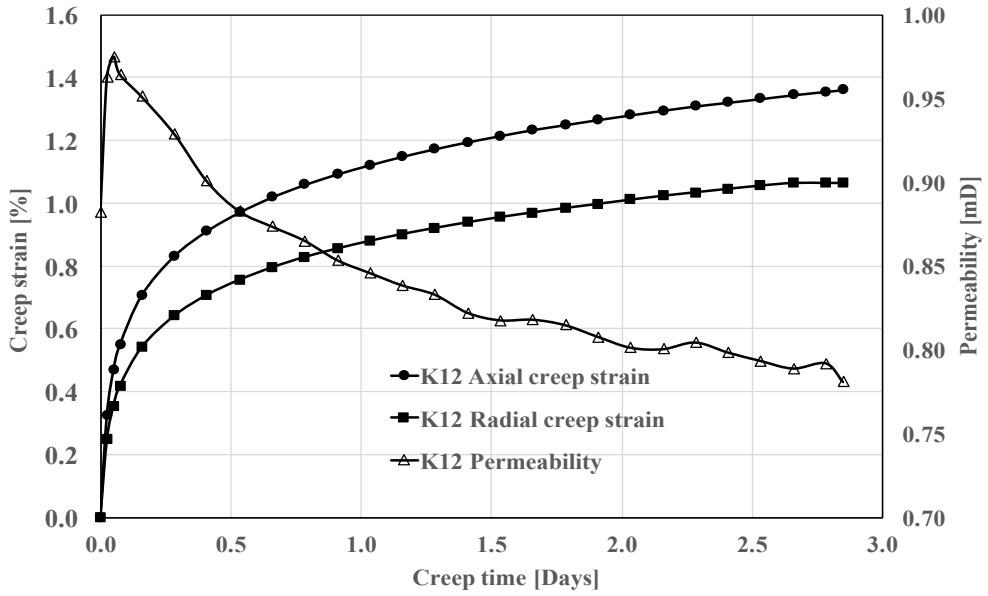

Figure 4.3 1st Creep phase for core K12 at 3 MPa confining pressure

Figure 4.2 and 4.3 show that the permeability of each sample decreases along the creep time. During the creep period, permeability of K12 decreases from 0.88 to 0.78 mD, and the reduction for K5 is from 0.86 to 0.81 mD. It is also shown that there exists a trend in the beginning of the creep phase that the permeability is suddenly increased up to around 0.95 mD for both samples and decreases gradually afterwards as creep continues. The dashed line on Figure 4.2 is an approximation for the data which was lost when the piston assembling inside the triaxial cell stopped moving.

Unloading. After the 1st creep phase, the confining pressure is loaded back to 3 MPa and samples are left to rest 24 hours before the initiation of the next deviatoric loading phase. Confining stress and permeability are plotted against the volumetric strain in Figure 4.4.

According to the unloading cycle in Figure 4.4, permeability increases from 0.8 to 0.92 mD and 0.86 mD respectively for K15 and K12 during unloading. Decrement of 0.7 mD for K5 and 0.4 mD for K12 is observed when resting at constant 3 MPa confining pressure. The unloading cycle does not bring the specimen back to its initial shape and permeability due to the plastic deformation caused by the hydrostatic loading above yield.

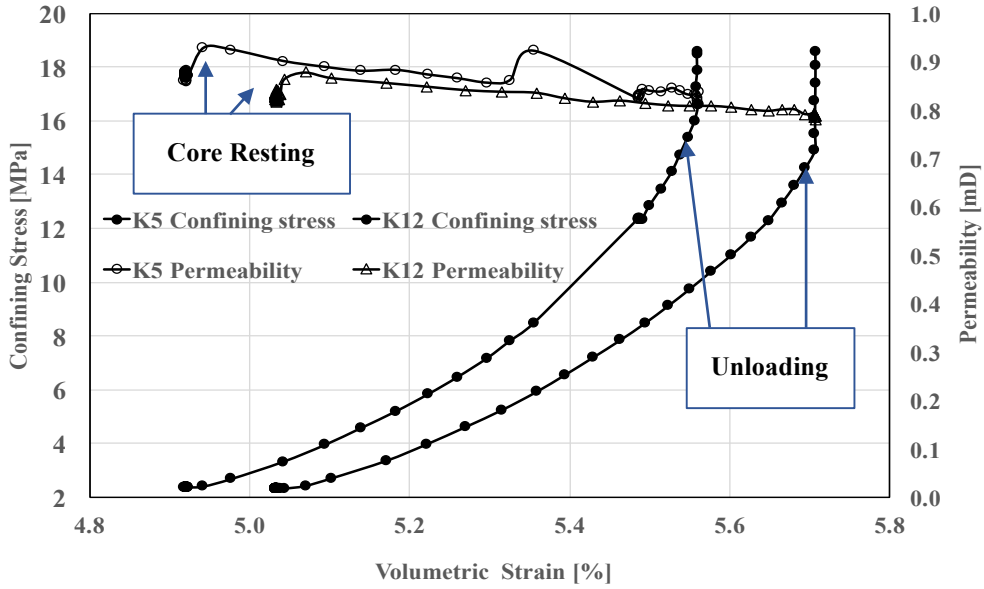

Figure 4.4 1st Unloading cycle for core K5 & K12

1st Deviatoric Loading. When the specimen has been rested properly, deviatoric loading is performed at constant confining pressure of 3 MPa. K5 and K12 are loaded deviatorically to an axial stress as high as 12.86 MPa and 12 MPa respectively. A fixed piston pressure, which is 0.3 MPa lower than the maximum piston pressure, is set after the appearance of peak axial stress. In order to prevent the core from failing, additional 1MPa piston pressure is taken down with constant ramping rate of 1MPa/min. Permeability is observed to be almost unchanged in this loading phase for both samples as seen from Figure 4.5.

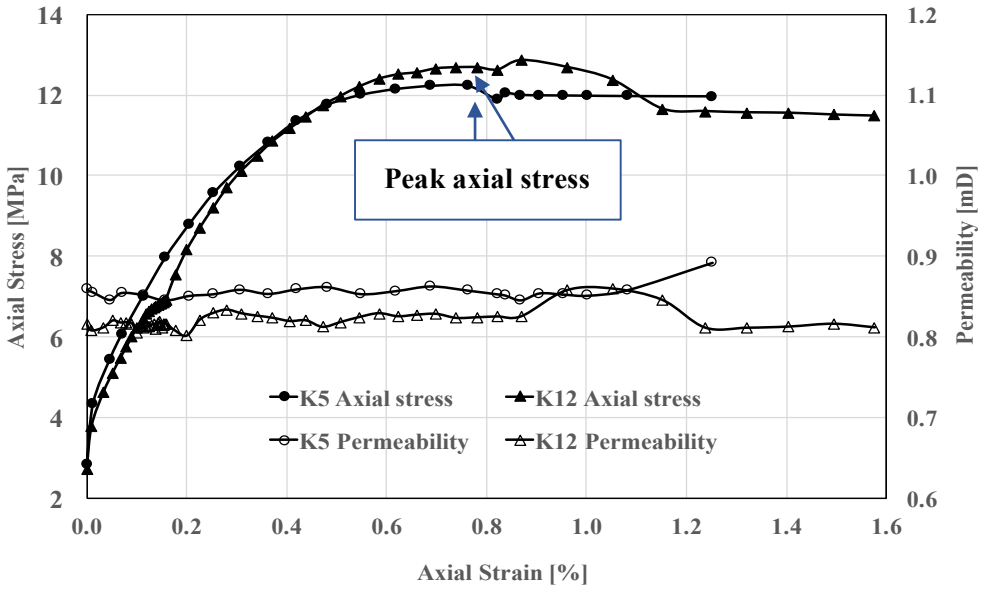

Figure 4.5 1st Deviatoric loading for core K5 & K12 at 3 MPa confining pressure

2nd Creep Phase. K5 is set to creep at a fixed piston pressure of 7.8 MPa for 1 hour and K12 is set to creep at constant 7.6 MPa piston pressure for 0.5 hour. Accelerating creep appears in the early creep stage for both samples. Figure 4.6 and 4.7 are plotted within the testing range of the extensometer, showing the permeability, axial creep strain and radial creep strain along the creep time.

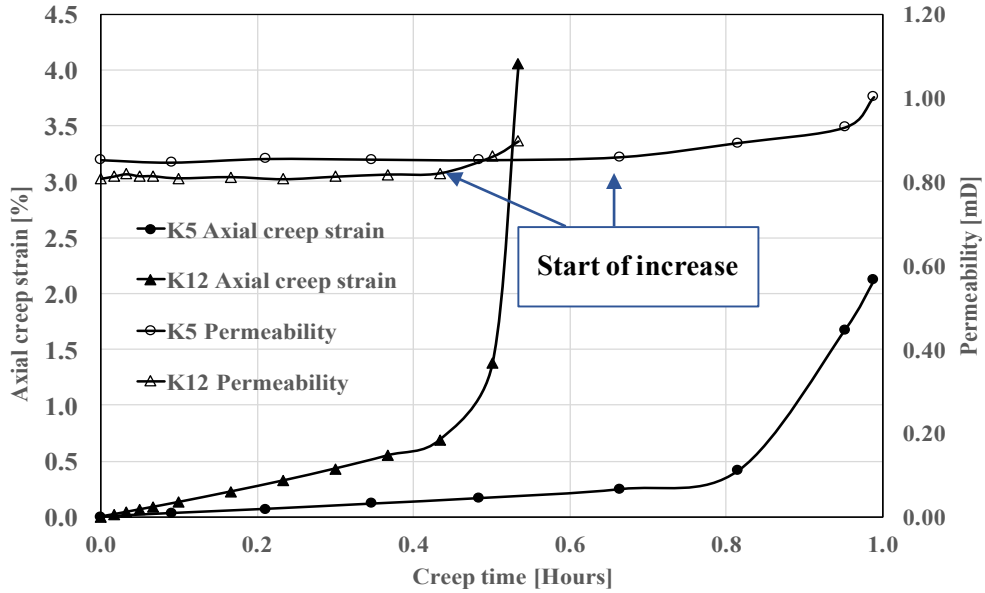

Figure 4.6 2nd Creep phase for core K5 & K12 at 3 MPa confining pressure

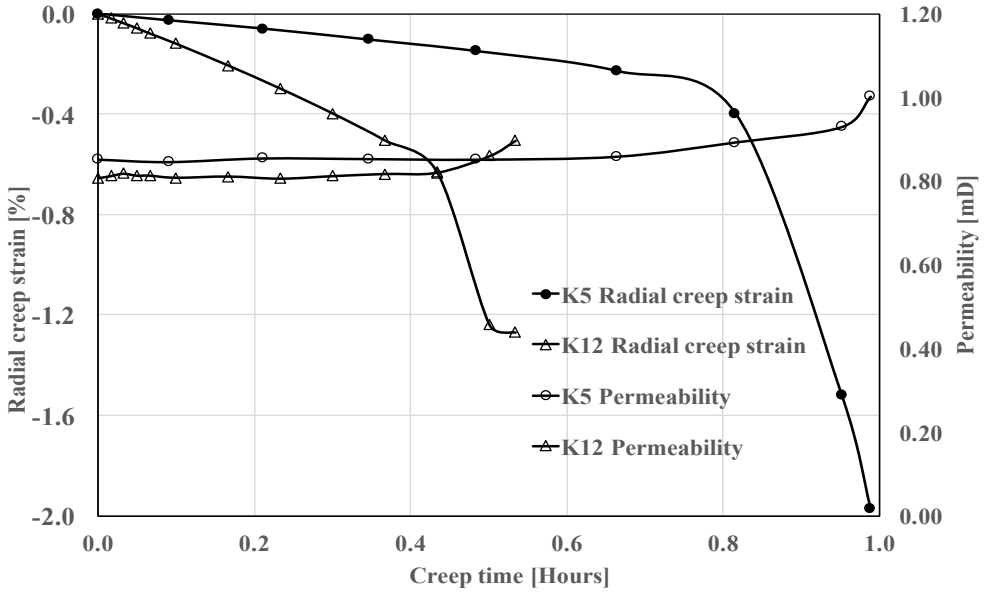

Figure 4.7 2nd Creep phase for core K5 & K12 at 3 MPa confining pressure

Permeability remains constant in the early 0.64 hour and 0.42 hour for K5 and K12 respectively. After this time, an abrupt increase in both radial and axial strain is

observed as the accelerating creep occurs. The increase in permeability is initiated at the same time as the occurrence of accelerating creep. These points where permeability increase starts are shown on Figure 4.6.

4.1.2 Conclusion

In this reference test, permeability undergoes continuous reduction with increasing confining pressure, acting to squeeze the pore spaces of chalk samples. The reduction in permeability of K5 and K12 in 1st hydrostatic loading is listed in Table 4.2.

Table 4.2 Permeability change in hydrostatic loading

Sample No.	Ini. Perm. (mD)	End Perm. (mD)	Reduction (%)
K5	2.12	0.86	60%
K12	2.23	0.88	60%

**Ini. Perm.=Initial Permeability, End Perm.=End Permeability*

In the 1st creep phase, K5 and K12 experience 14% and 4% reduction in permeability respectively compared to the initial creep permeability. No significant changes in permeability are observed in the unloading cycle.

In the deviatoric loading phase, permeability stays almost constant. Both samples failed in the early creep time. Figure 4.8 and 4.9 are the images of the failed samples in this test series, showing evident X-shape shear bands after brittle failure.

Figure 4.8 Core K12 after creep failure

Figure 4.9 Core K5 after creep failure

4.2 Test series 2

The porosities of core K6 and K9 used in this mechanical test series are respectively 38.63% and 38.44%. Both samples are firstly loaded hydrostatically to 3 MPa confining pressure, and then followed by two successive deviatoric loading cycles for K6 and three loading cycles for K9. The test schemes are listed in Table 4.3.

Table 4.3 The test schemes of core sample K6 and K9

Loading Cycle	***Confining Pressure (MPa)***		***Piston Pressure (MPa)***		***Creep Time (Days)***	
	K6	***K9***	***K6***	***K9***	***K6***	***K9***
1st DL	3.0	3.0	8.8 Max.	8.5 Max.	/	/
1st DC			6.7	7.2	2.8	2.8
2nd DL			8.8 Max.	8.9 Max.	/	/
2nd DC			8.6	7.6	0.006	0.9
3rd DL	/	1.2	/	4.6 Max.	/	
3rd DC			/	3.8	/	2.8

4.2.1 Results

1st Deviatoric Loading Phase. In the first deviatoric loading phase, K6 and K9 are loaded deviatorically up to a peak axial stress of 12.9 MPa and 12.6 MPa respectively prior to setting a fixed piston pressure, which is 0.3 MPa lower than the maximum piston pressure. Afterwards, in order to avoid cores from failing, 2 MPa and 1 MPa of piston pressure is taken down respectively from K6 and K9 with constant 1 MPa/min ramping rate.

Permeability and axial stress are plotted against the axial strain and radial strain in Figure 4.10 and 4.11, showing that with increasing axial stress, permeability undergoes continuous decrease from 1.97 to 1.62 mD for K6 and from 1.9 to 1.51 mD for K9. There exists a certain point where the permeability is prone to stay stable and unaffected by the increase of axial stress for K9 in the range of axial strain between 0.68-0.79%. Good repeatability is shown for these two samples in the 1st deviatoric loading phase

while comparing the stress-strain and permeability-strain curves plotted in Figure 4.10 and 4.11.

As seen from Figure 4.10, from the initial stress until 6 MPa axial stress, the deformation in the radial direction is negligible. As the loading continues, the expansion in the radial direction is accelerated. Before K9 reaches the peak axial stress, the stress and strain curve coincides exactly in Figure 4.11.

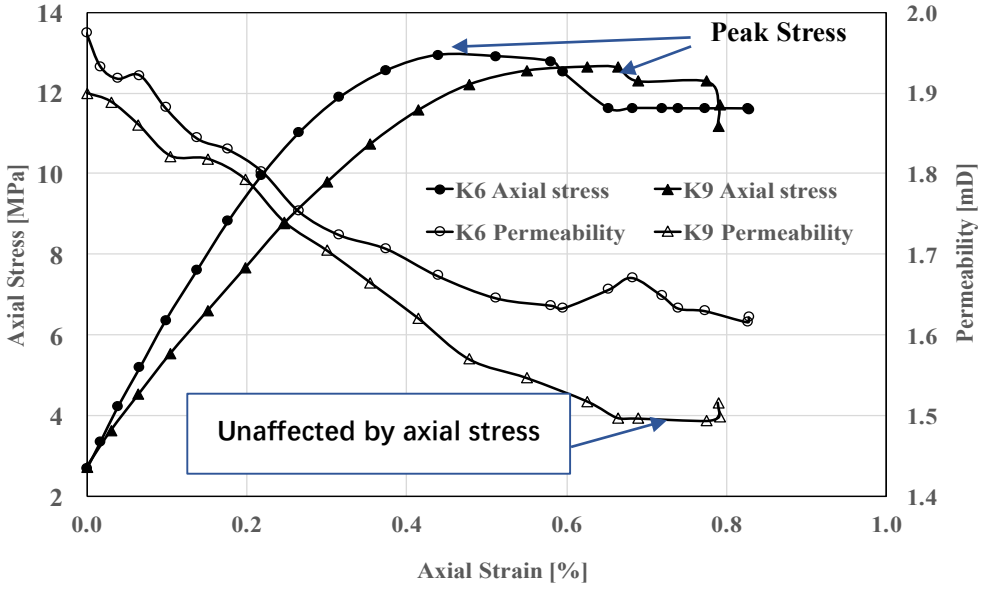

Figure 4.10 1st Deviatoric loading for core K6 & K9 at 3 MPa confining pressure

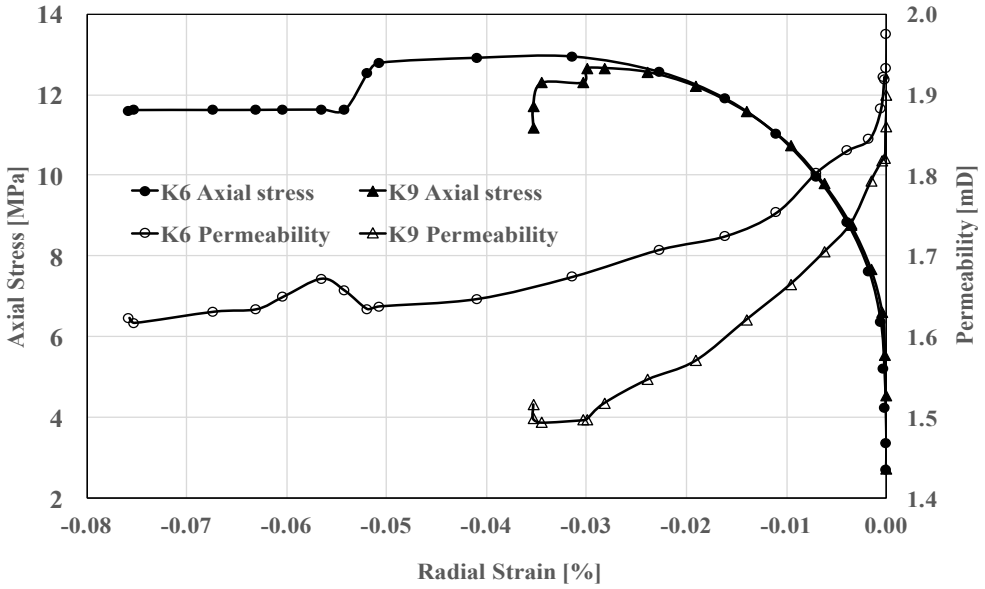

Figure 4.11 1st Deviatoric loading for core K6 & K9 at 3 MPa confining pressure

1st Creep Phase. K6 and K9 are left to creep at constant piston pressure of 6.7 MPa and 7.2 MPa respectively for 2.8 days. The permeability changes of the K6 and K9 are investigated along the axial and radial strain under constant axial stress load.

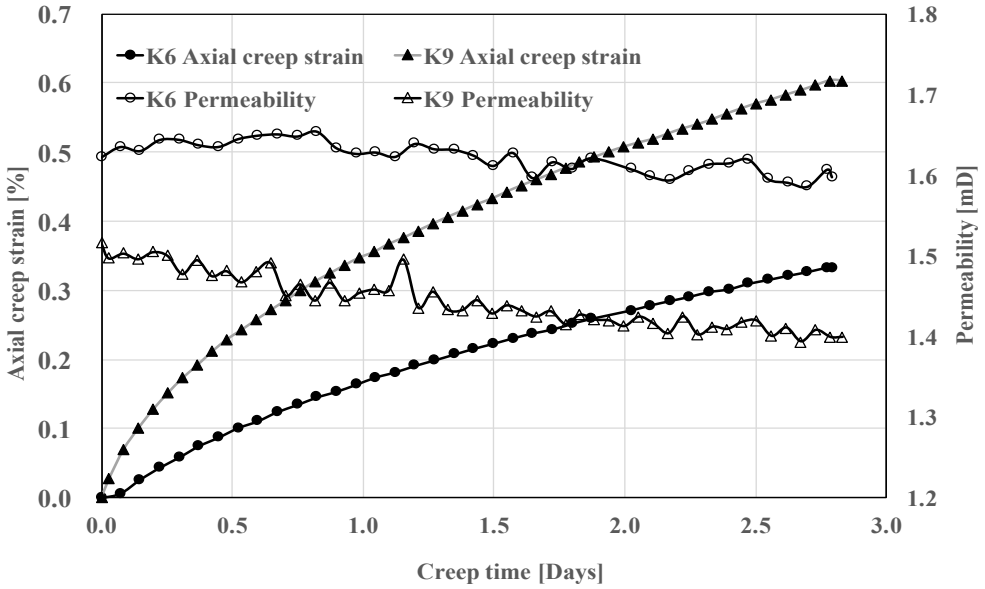

Figure 4.12 1st Creep phase for core K6 & K9 at 3 MPa confining pressure

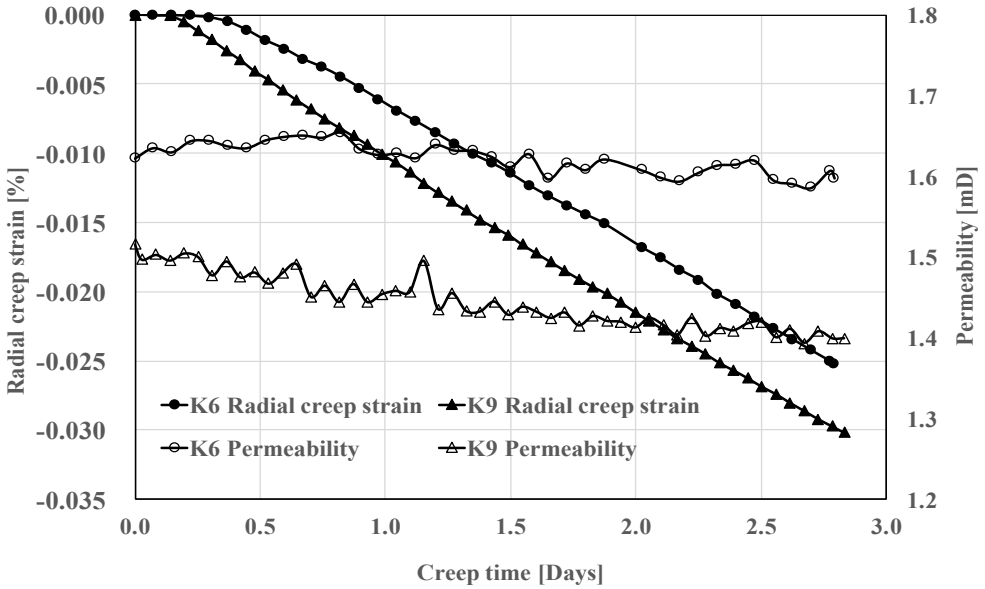

Figure 4.13 1st Creep phase for core K6 & K9 at 3 MPa confining pressure

K6 starts with a permeability of 1.62 mD and ends up with 1.60 mD, showing negligible 0.02 mD decrease in permeability, whereas, the reduction in permeability for K9 is more evident, showing 0.1 mD decrease at the end of 1st creep phase (Figure 4.12).

Figure 4.12 shows that axial strain of K9 is around 2 times higher than that of K6 at identical creep time. According to Figure 4.13, the deformation of K9 in the radial direction also appears to be greater than K6.

Unloading. As seen from Figure 4.14, permeability remains almost constant during the process of unloading and resting.

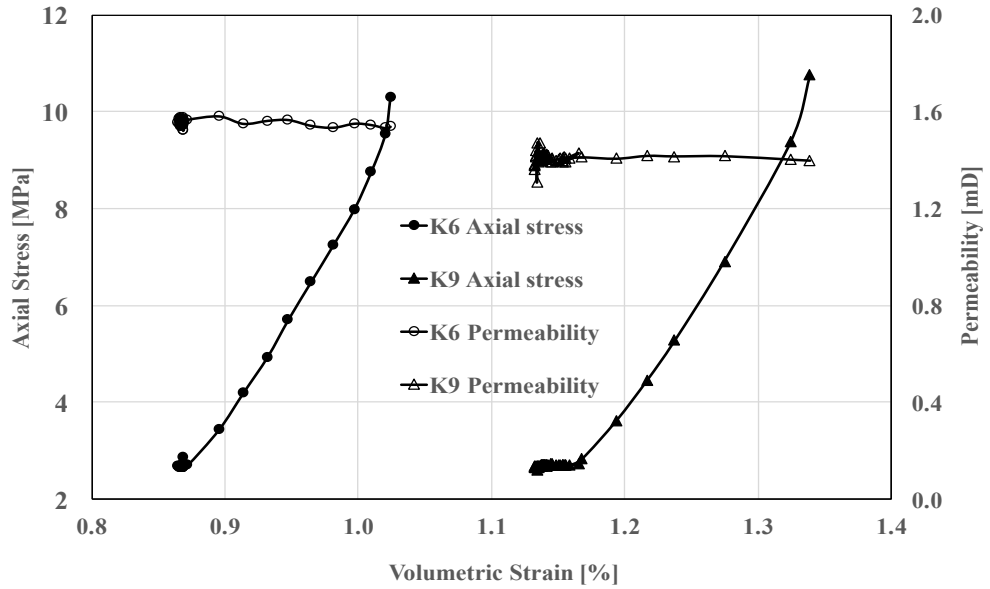

Figure 4.14 Unloading cycle for core K6 & K9

2nd Deviatoric Loading Phase. The second deviatoric loading is performed up to a peak axial stress of 13 MPa for both samples before setting a fixed piston pressure, which is 0.3 MPa less than the maximum piston pressure to prevent cores from failing. K6 failed in the process of lowering the piston pressure, therefore, the permeability-strain curves for K6 is plotted in Figure 4.15 and 4.16 before the core fails. Additional 1 MPa piston pressure is reduced from K9 before initiating the creep phase.

From the beginning of this loading until 6 MPa axial stress, the deformation in the radial direction can be negligible. After 6 MPa axial stress, change in radial strain is increased. No significant change in permeability is observed for K6 and K9 throughout this loading phase.

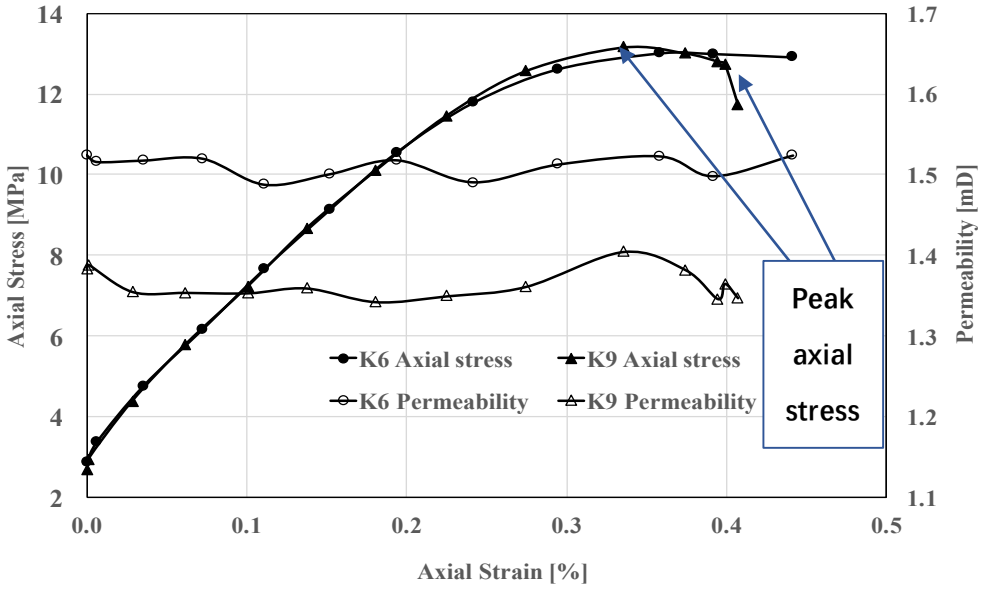

Figure 4.15 2nd Deviatoric loading for core K6 & K9 at 3 MPa confining pressure

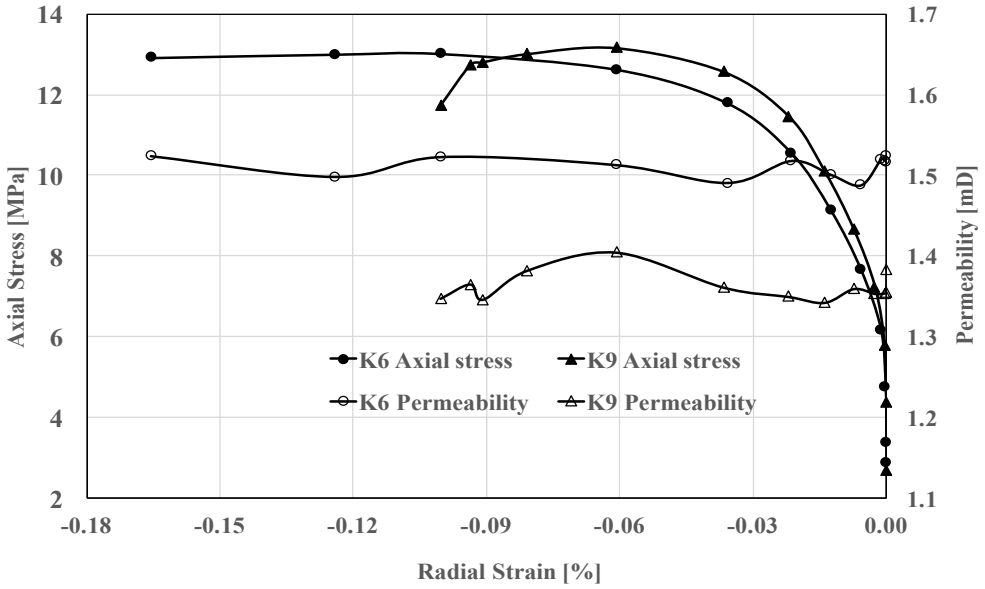

Figure 4.16 2nd Deviatoric loading for core K6 & K9 at 3 MPa confining pressure

K6 Failure. In general, when the core fails, the deformation in the radial direction will be accelerated drastically. As is exhibited in Figure 4.17 with radial strain and permeability plotted against time, a sharp increase of the radial strain is observed after 1.4 hours, resulting in an abrupt decrease in permeability. Figure 4.18 shows the image of undried core sample K6 after failure.

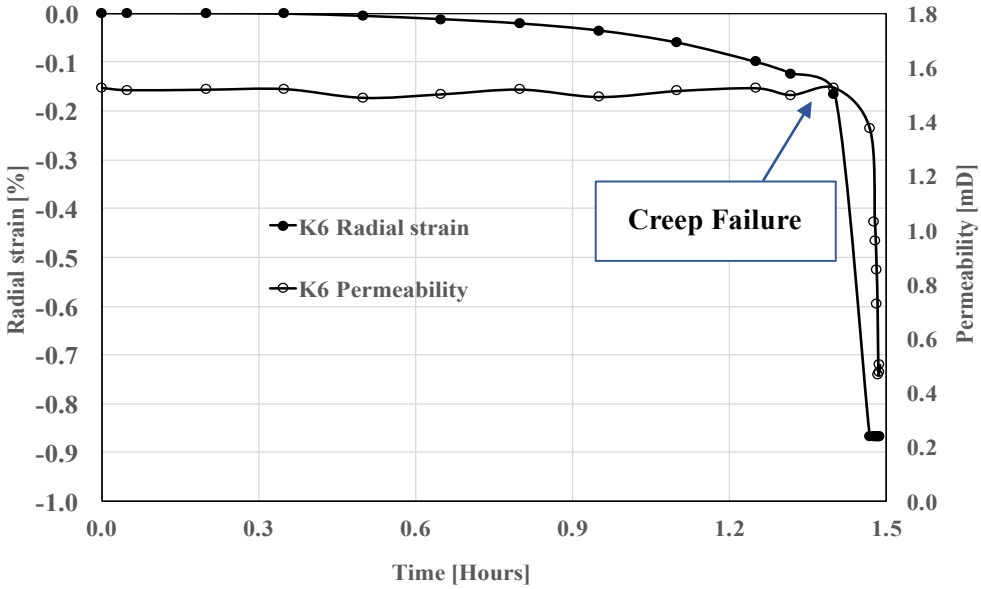

Figure 4.17 Radial strain and Permeability change with time for core sample K6

Figure 4.18 Core K6 after failure

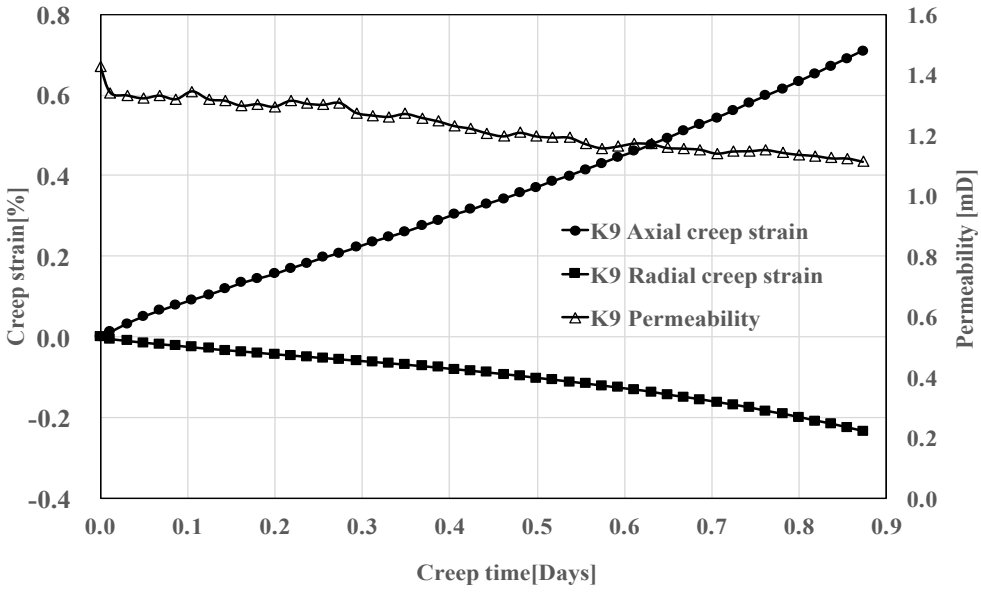

Figure 4.19 2nd Creep phase for core K9 at 3 MPa confining pressure

2nd Creep Phase. K9 is left to creep at 11.5 MPa axial stress for 0.89 days. A slight decrease of 0.3 mD is observed (Figure 4.19).

Unloading. K9 is unloaded back to 0.7 MPa piston pressure and the confining pressure is reduced to 1.2 MPa after unloading. Flooding brine is switched to distilled water since the prepared brine has been run out. In the process of this unloading cycle, no significant change in permeability is observed.

3rd Deviatoric Loading Phase. A third deviatoric loading is performed up to 6 MPa axial stress, which is around half the value of that in the 1st and 2nd deviatoric loading, since the core is loaded at a lower constant confining pressure. After reaching the peak axial stress, a fixed piston pressure is set to be 0.3 MPa lower than the maximum piston pressure at the axial strain of 0.3% (Figure 4.20). From the beginning to 0.3% axial strain, permeability is increased by a factor of 1.1.

In order to avoid core from failing, 1 MPa of the piston pressure is taken down gradually with a constant ramping rate of 1 MPa/min prior to the creep phase.

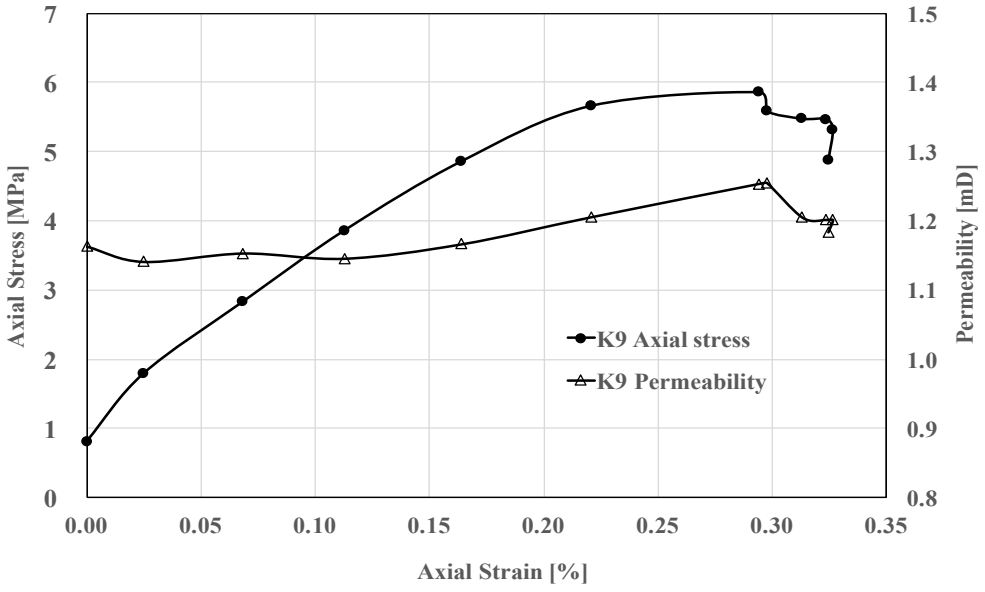

Figure 4.20 3rd Deviatoric loading for core K9 at 1.2 MPa confining pressure

3rd Creep Phase. K9 is left to creep at 4.8 MPa axial stress for 0.84 day. The relationship of permeability, creep strain and creep time is plotted and studied. As showed in Figure 4.21, permeability of the K9 remains almost constant at 1.2 mD in

this phase with changes of 0.14% in axial strain and 0.16% in radial strain.

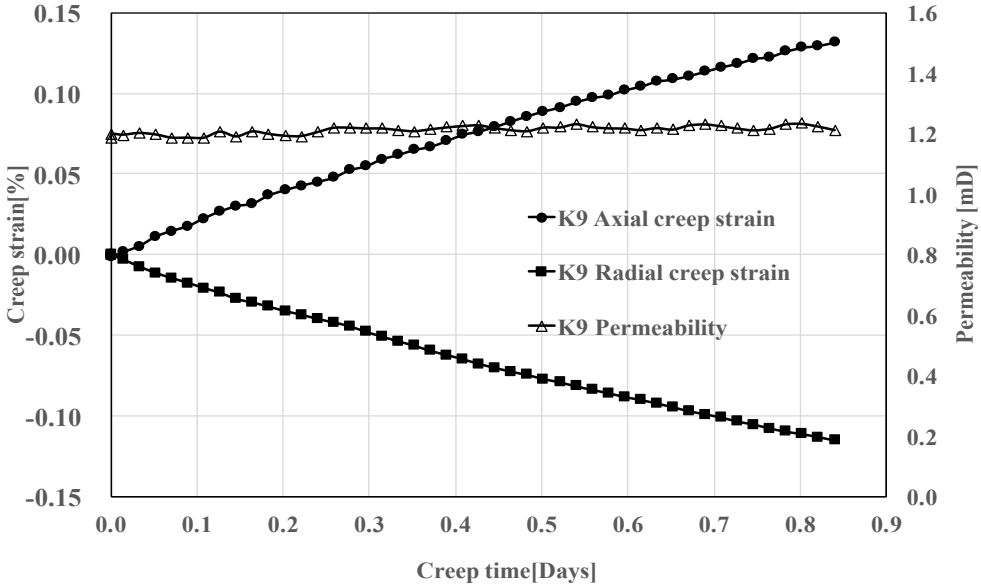

Figure 4.21 3rd Creep phase for core K9 at 3 MPa confining pressure

Relation between Permeability Evolution and Strain Rate. An interest phenomenon observed (Figure 4.22) in the three successive deviatoric loadings for core K9 is that the time for the chalk core to experience shear failure is lessened after each loading phase. There exists a critical point where the radial strain rate becomes greater than the axial strain rate. This critical point is accompanied with an increase in permeability.

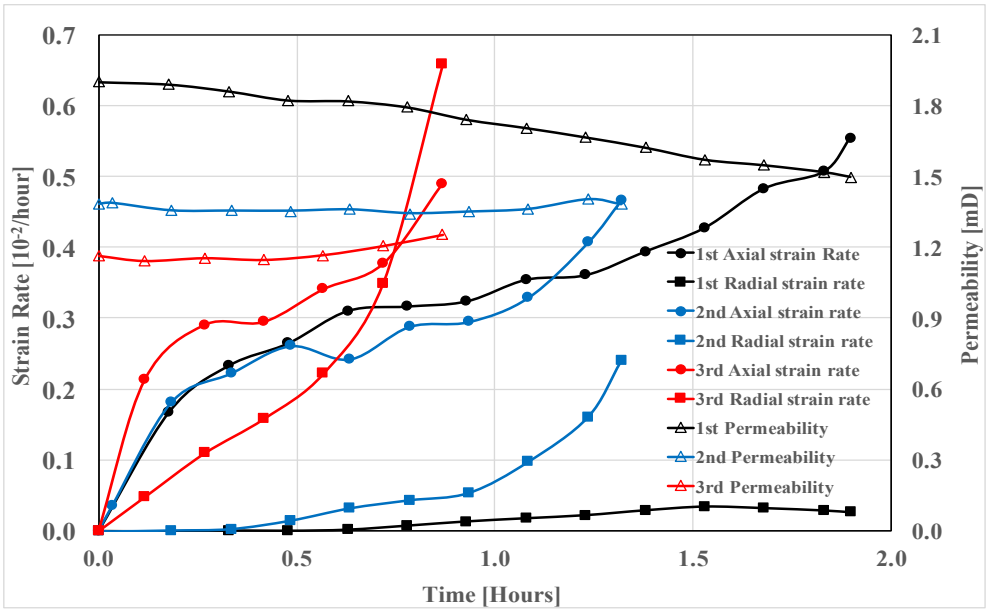

Figure 4.22 Permeability evolution vs. strain rate for core K9

Assumptions are made that this critical point can be used as a symbol to recognize the occurrence of shear failure. A further observation on the image of K9 at the end of the experiment proves the assumption with an evident appearance of single shear-band failure (Figure 4.23).

Figure 4.23 Image of core K9 after experiment

As is shown in Figure 4.22, the critical point is attained when the radial strain rate exceeds the axial strain rate, indicating that the expansion in the radial direction is greater than the compression in the axial direction. In the 1st deviatoric loading phase, the axial strain rate is more than 10 times higher than the radial strain rate and permeability experiences continuous decrease. In the 2nd deviatoric loading phase, as the difference between the radial and axial strain rate is decreased significantly, permeability remains almost constant. In the 3rd deviatoric loading phase, permeability increase is observed with an occurrence of shear failure.

4.2.2 Conclusion

Table 4.4 Permeability reduction in 1st deviatoric loading

Sample No.	Ini. Perm. (mD)	End Perm. (mD)	Reduction
K6	1.97	1.62	17%
K9	1.90	1.51	21%

Table 4.4 shows the permeability reduction in the 1st deviatoric loading. Comparing the permeability reduction in 1st deviatoric loading with the 1st hydrostatic loading in test series 1, permeability reduction caused by deviatoric loading is 30-40% lower.

In the 2nd loading, deformation in the radial direction is accelerated with increasing axial stress, however, the change in the axial strain is less than that in the 1st loading. Table 4.5 shows the comparison between the radial and axial strain in 1st and 2nd deviatoric loading before lowering piston pressure.

Table 4.5 Comparison of radial and axial strain in deviatoric loadings

Loading No.	Axial Strain (%)	Radial Strain (%)
K6 1st	0.6	0.05
K6 2nd	0.4	0.15
K9 1st	0.8	0.03
K9 2nd	0.4	0.09

Assumption is made based on Figure 4.22 that shear failure occurs at the point where the radial strain rate exceeds the axial strain rate. The occurrence of shear failure is accompanied with an increase of 0.1 mD in permeability in the 3rd deviatoric loading.

4.3 Test series 3

Core K11 with porosity of 38.69% and K16 with porosity of 39.25% are used in this mechanical test series. Both samples are loaded hydrostatically to 3 MPa confining in the beginning and then followed by a hydrostatic and deviatoric loading respectively. The test schemes are listed in Table 4.6.

For core K16, besides the test schemes listed in the Table 4.6, an additional deviatoric loading and creep is conducted to verify the assumptions made while analyzing the trend.

Table 4.6 The test schemes of Core sample K11 and K16

Loading	*Confining Pressure (MPa)*		*Piston Pressure (MPa)*		*Creep Time (Days)*	
Cycle	*K11*	*K16*	*K11*	*K16*	*K11*	*K16*
1st DL	3.0	3.0	8.4 Max.	7.6 Max.	/	/
1st DC			7.1	6.3	0.7	2.6
1st HL	18.3 Max.	17.3 Max.	1.7 Max.	1.85 Max.	/	/
1st HC	18.3	17.3	1.7	1.85	2.8	0.8
2nd DL	3.0	3.0	8.7	7.9 Max.	/	
2nd DC			7.4	6.6	0.7	0.9

4.3.1 Results

1st Deviatoric Loading Phase. K11 and K16 are loaded deviatorically up to 12.5 MPa and 11.5 MPa peak axial stress respectively, after which a fix piston pressure is set to be 0.3 MPa lower than the maximum piston pressure. In order to avoid failure, additional 1 MPa piston pressure is decreased before the initiation of creep phase. Permeability evolution and axial strain as well as radial strain are plotted in Figure 4.24 and 4.25, showing that permeability decreases with increasing axial stress before ramping down 1 MPa piston pressure. The permeability evolution in this deviatoric loading phase is similar to the 1st deviatoric loading in test series 2.

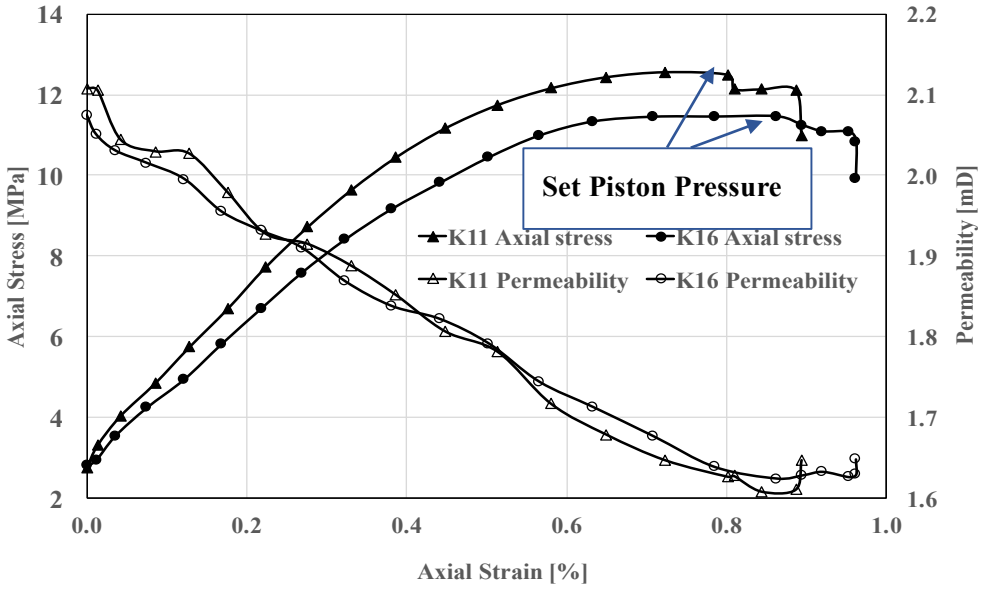

Figure 4.24 1st Deviatoric loading for core sample K11 & K19 at 3 MPa confining pressure

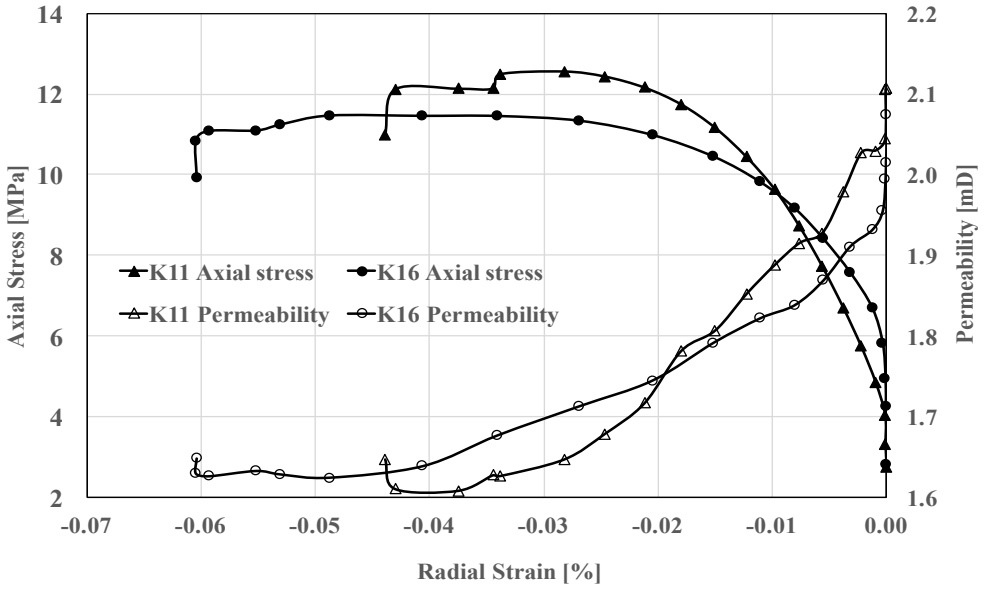

Figure 4.25 1st Deviatoric loading for core sample K11 & K19 at 3 MPa confining pressure

1st Creep Phase. K11 and K16 are left to creep at 11 MPa and 10 MPa axial stress respectively (Figure 4.26 and 4.27). Permeability decreases slightly along the creep time and in total 0.13 mD reduction is observed for both samples.

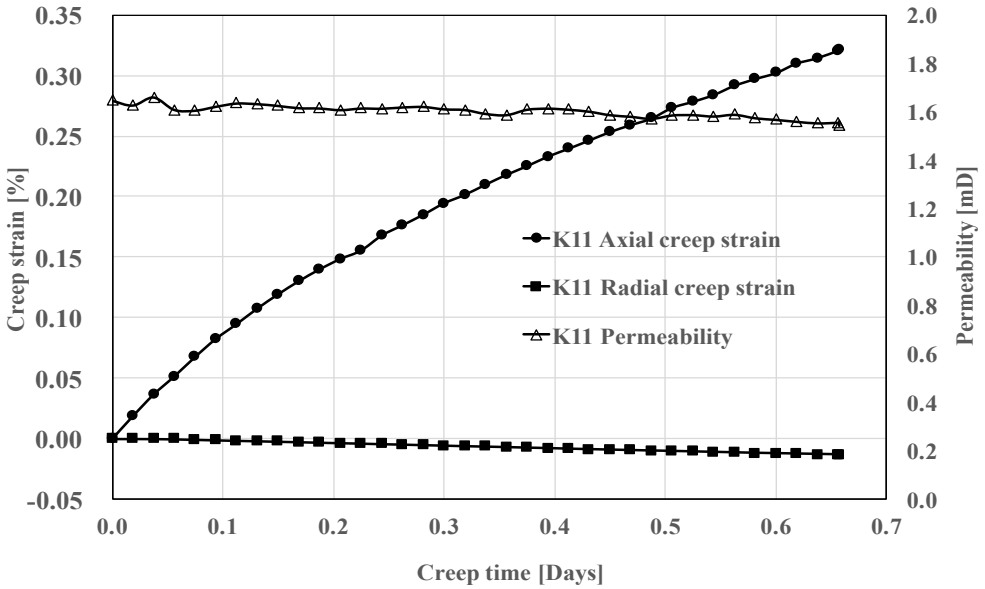

Figure 4.26 1st Creep phase for core K11at 3 MPa confining pressure

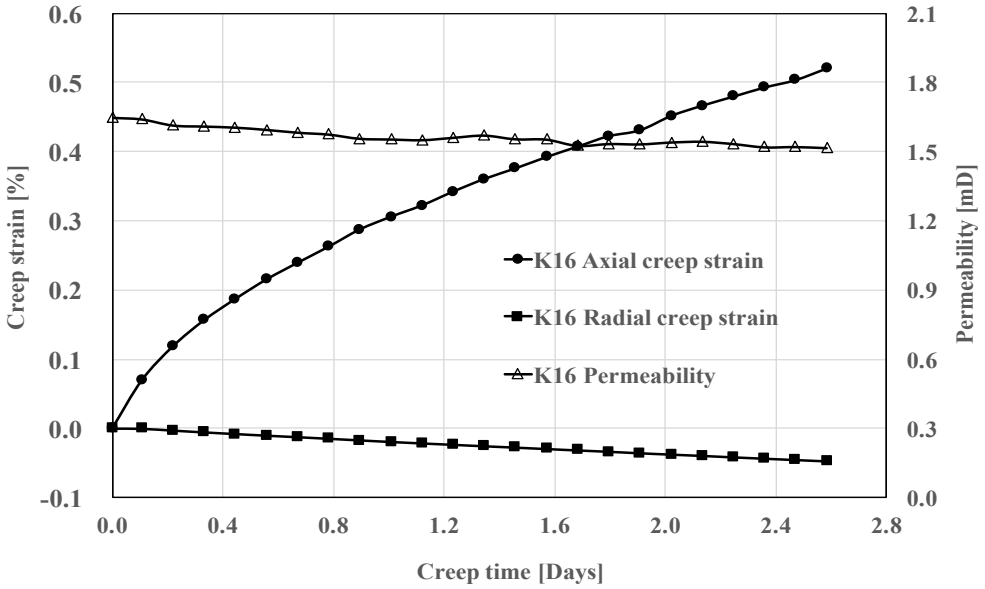

Figure 4.27 1st Creep phase for core K16 at 3 MPa confining pressure

Unloading. After the creep phase, piston pressure is loaded back to 0.7 MPa, K11 and K16 are left to rest 24 hours before proceeding to the next loading cycle. Figure 4.28 shows the permeability evolution in the unloading and resting processes. No significant changes in permeability are observed.

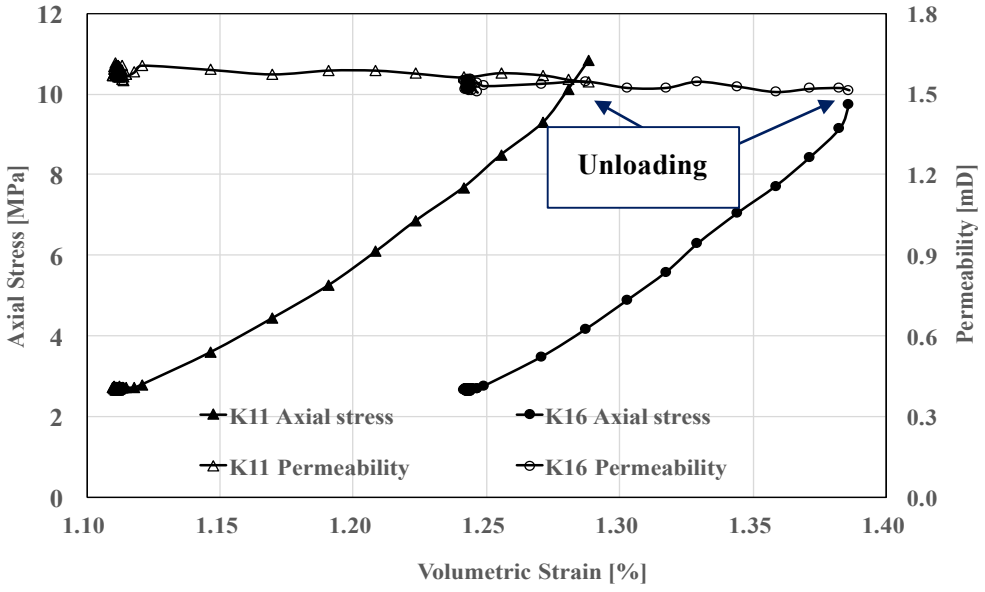

Figure 4.28 1st Unloading cycle for core K11 & K16

Hydrostatic Loading Phase. Core K11 and K16 are loaded hydrostatically up to 17.5 MPa and 16.5 MPa confining stress respectively. Effective confining stress along with permeability are plotted against the axial strain and radial strain in Figure 4.29 and 4.30.

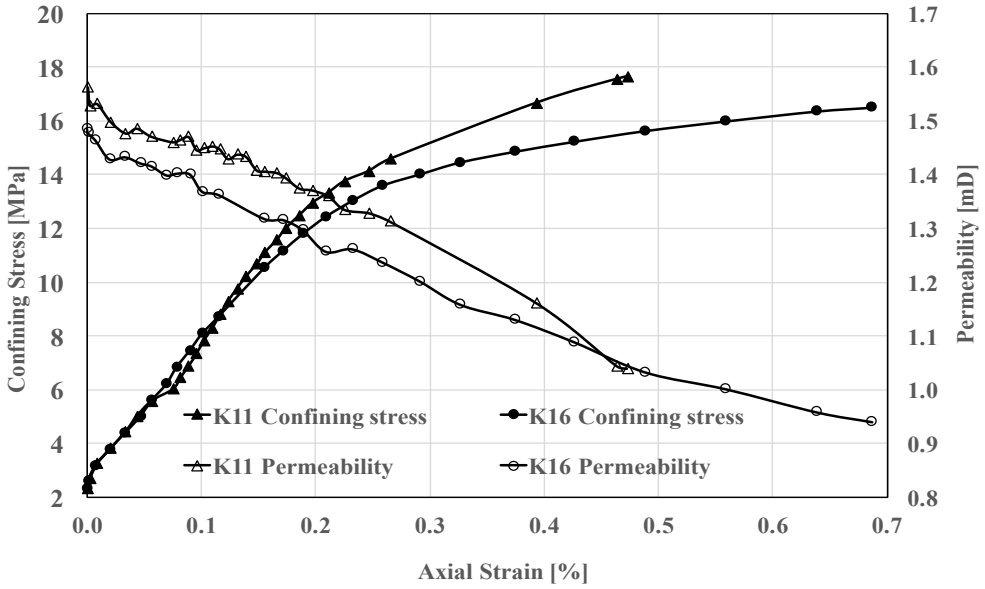

Figure 4.29 1st Hydrostatic loading for core K11 & K16

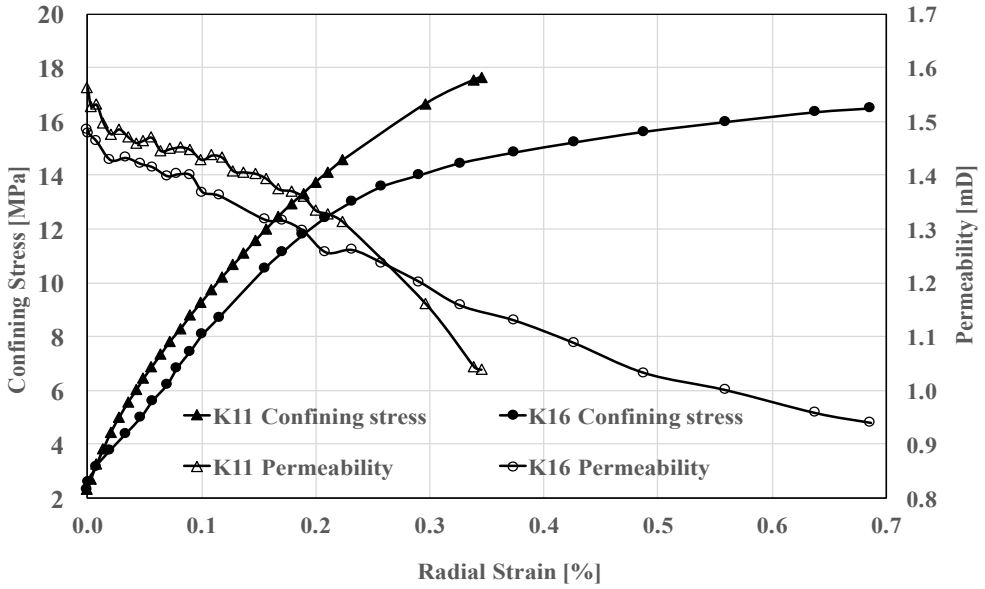

Figure 4.30 1st Hydrostatic loading for core K11 & K16

With increasing confining stress acting to squeeze the pore spaces from all directions, the permeability experiences a reduction around 0.5 mD at the end of the loading. The end permeability of K16 is 0.94 mD, which is close to the value (0.88 mD) obtained in the hydrostatic loading performed in test series 1. However, the initial permeability of K16 in this loading phase is 1.5 mD, which is 1.4 times lower compared to the initial value (2.1 mD) in test series 1. This lower initial permeability of K16 is due to the influence of the 1st deviatoric loading in this test series. Regardless of the difference in

initial permeability, the end permeability of K16 is almost the same as the end permeability of K5 and K12 in the test series 1, indicating that the 1st deviatoric loading performed prior to hydrostatic loading has minor effect on the end permeability.

2nd Creep Phase. After the hydrostatic loading, a fixed confining pressure of 17.3 MPa and 16.3 MPa for K11 and K16 is set respectively prior to the 2nd creep phase.

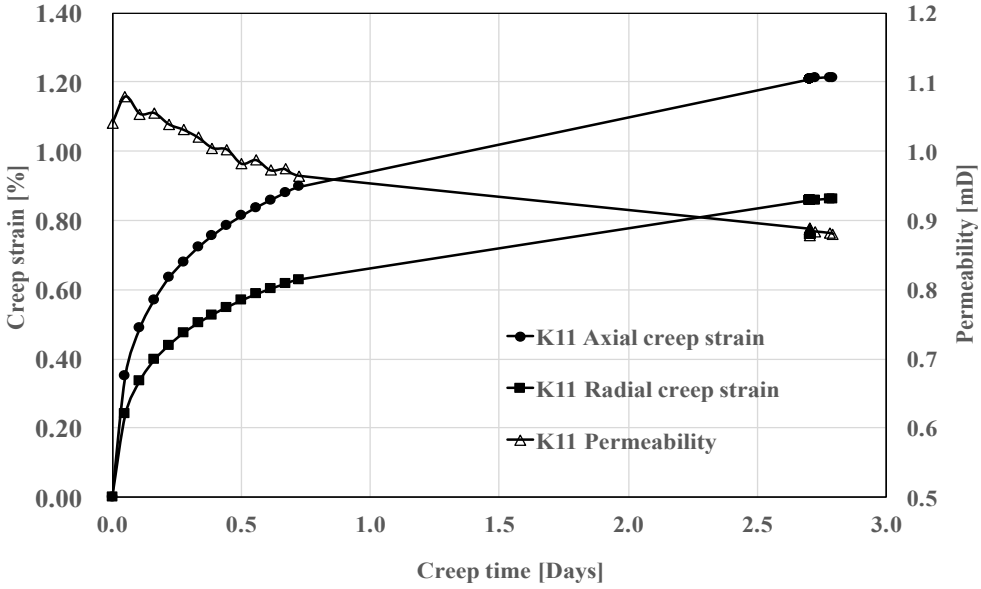

Figure 4.31 2nd Creep phase for core K11 at 18 MPa confining pressure

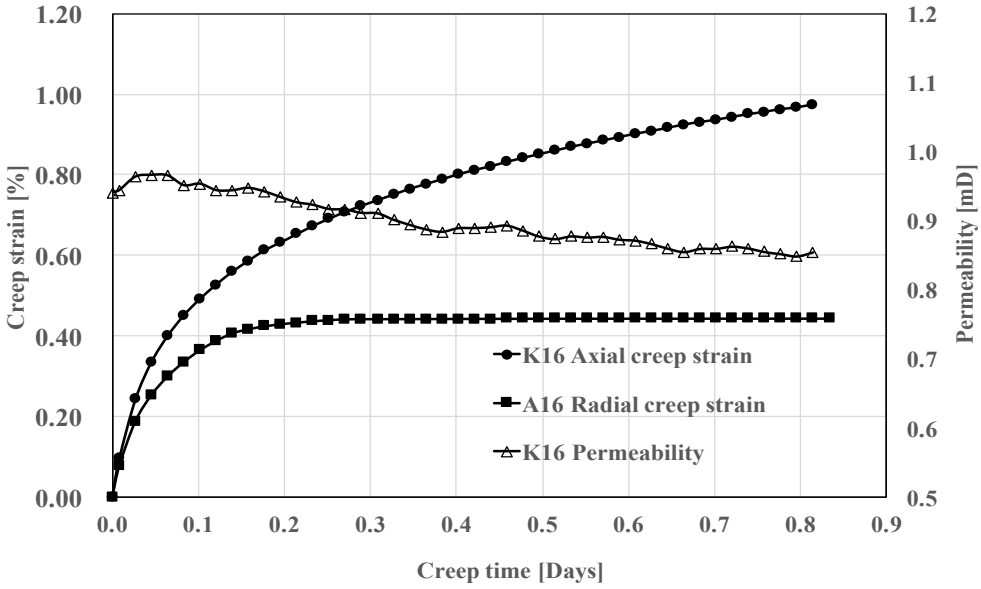

Figure 4.32 2nd Creep phase for core K16 at 17 MPa confining pressure

Axial creep strain and permeability are plotted against creep time in Figure 4.31 and 4.32. The big gap without data points on Figure 4.31 is due to a non-operating state of the LabView system, thus, the measurement data was lost in this period.

In this creep phase, permeability of K11 is reduced from 1.12 mD to 0.88 mD in 2.8 days and permeability of K16 is reduced from 0.98 mD to 0.9 mD in 0.85 days.

Unloading. After the 2nd creep phase, confining pressure is unloaded back to 3 MPa. Permeability remains almost constant in this unloading cycle.

2nd Deviatoric Loading Phase. Another deviatoric loading is conducted by increasing the applied axial stress up to 12.8 MPa for K11 and 11.9 MPa for K16, after that a fixed piston pressure, which is 0.3 MPa lower than the maximum piston pressure, is set.

Figure 4.33 shows no significant change in permeability with increasing axial stress. After experiencing the 1st deviatoric and hydrostatic loading in sequence, permeability of the two samples tend to become unaffected by the increase of axial stress in the 2nd deviatoric loading.

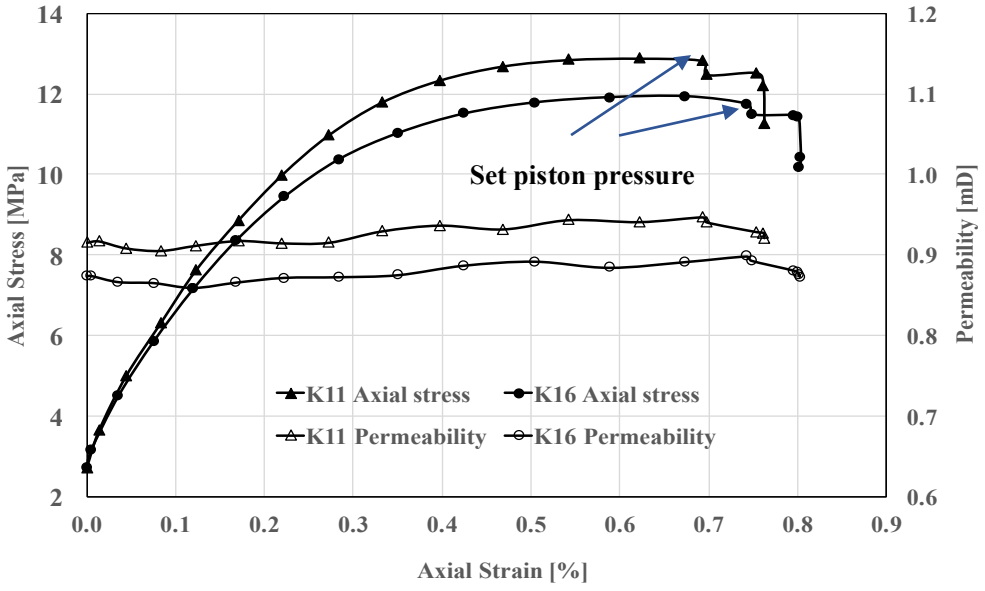

Figure 4.33 2nd Deviatoric loading for core K11 & K16 at 3 MPa confining pressure

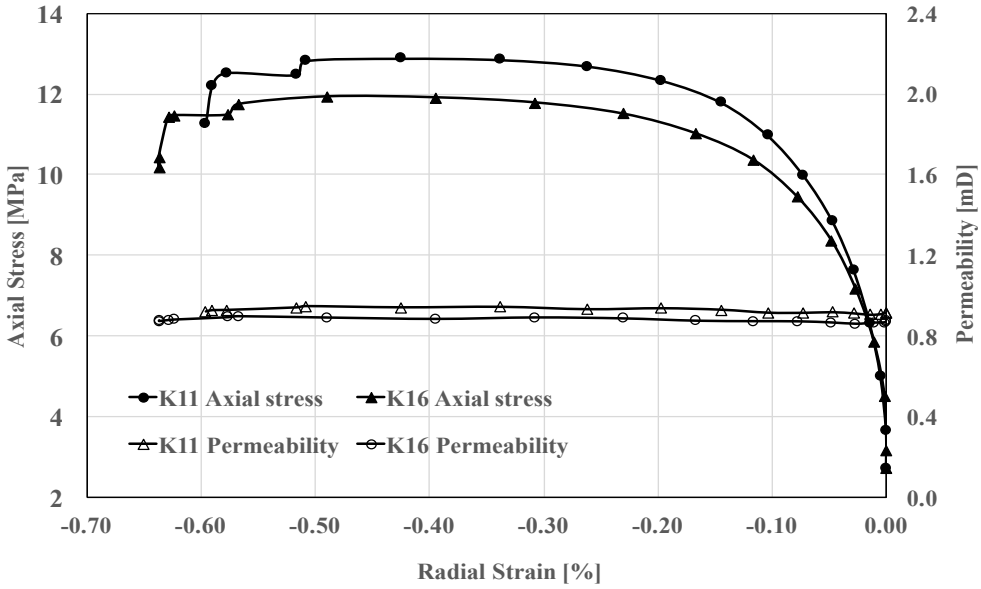

Figure 4.34 2nd Deviatoric loading for core K11 & K16 at 3 MPa confining pressure

In order to avoid the core from failing, piston pressure is reduced by 1 MPa prior to the 3rd creep phase. It is observed from Figure 4.34 that the radial strain at the end of the 2nd deviatoric loading is -0.65%, which is 10 times greater than the value (-0.06%) from the 1st deviatoric loading (Figure 4.25), however, the end axial strain is the 1st and 2nd loadings is almost the same (0.8% on Figure 4.34).

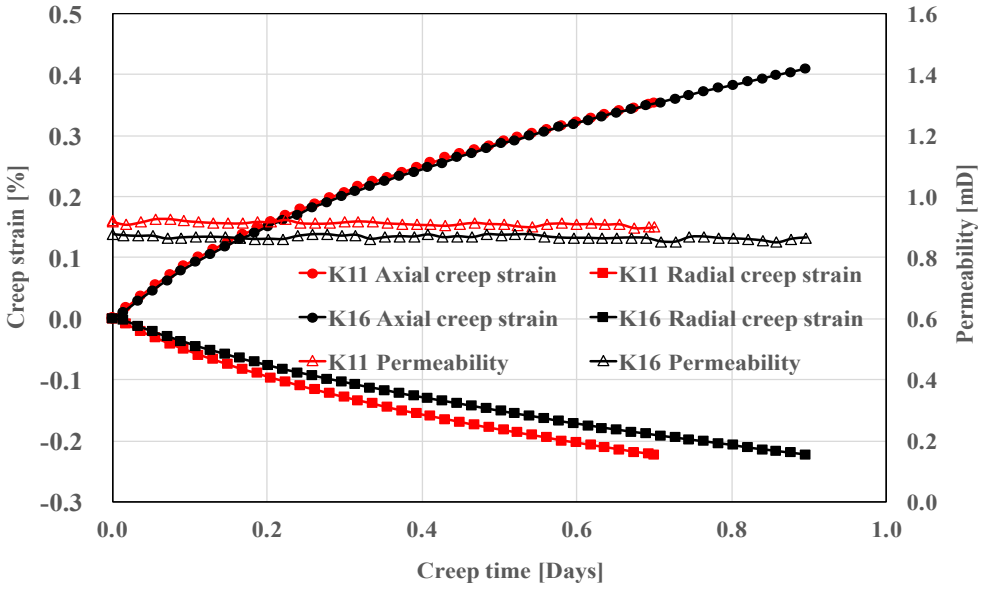

Figure 4.35 3rd Creep phase for core K11 & K16 at 3 MPa confining pressure

3rd Creep Phase. Figure 4.35 exhibits the relationship of axial and radial creep strain as well as permeability with creep time. The deformation of K11 in the axial direction

coincides perfectly with the curve of K16. Permeability remains almost constant.

3rd Deviatoric Loading Phase. A third deviatoric loading is performed on K16 in order to verify that after the previous sequences of loading cycles, permeability is likely to remain constant during deviatoric loading. K16 is loaded deviatorically up to 8.2 MPa axial stress prior to setting a constant piston pressure. It is observed from Figure 4.36 that permeability stays unchanged during loading, which proved the assumption.

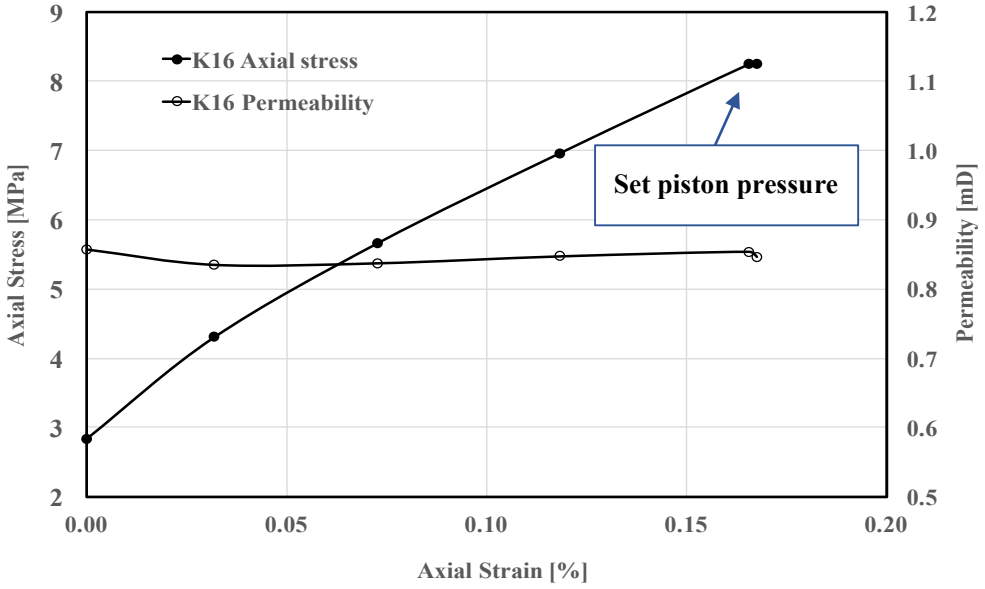

Figure 4.36 3rd Deviatoric loading for core K16 at 3 MPa confining pressure

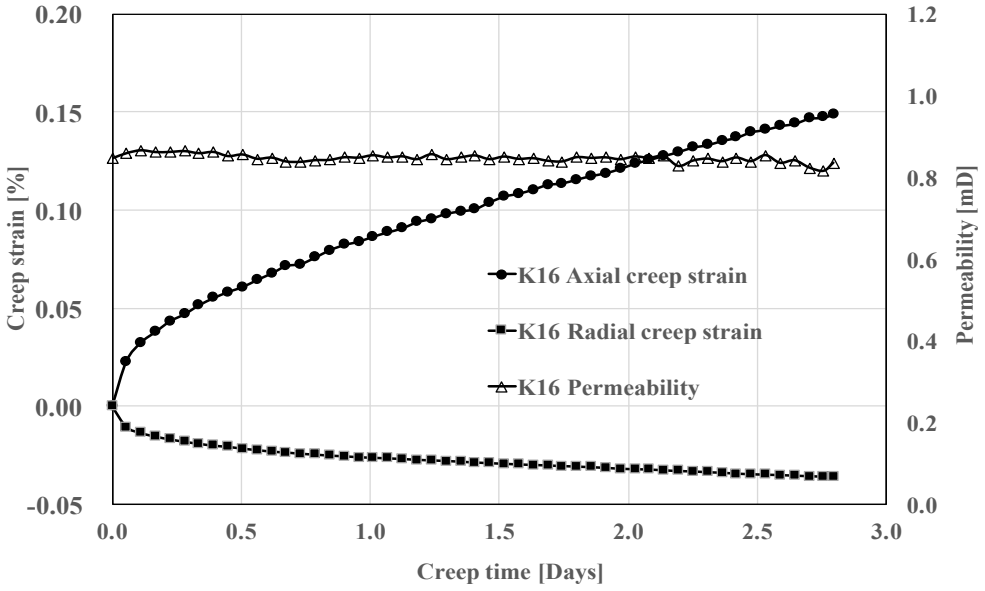

Figure 4.37 4th Creep phase for core K16 at 3 MPa confining pressure

4th Creep Phase. K16 is left to creep at a constant piston pressure of 5 MPa. No significant change in permeability is exhibited in this creep phase. (Figure 4.37).

Relation between Permeability Evolution and Strain Rate. In order to verify the characteristics of the relationship between strain rate and shear failure, the strain rate and permeability are plotted against the loading time for both samples in Figure 4.38 and 4.39.

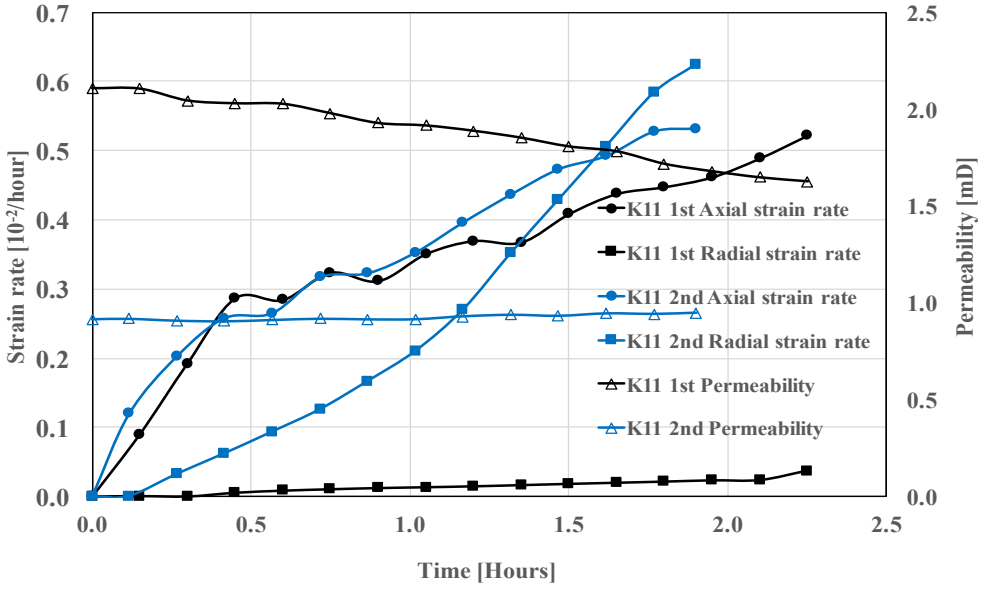

Figure 4.38 Permeability evolution vs. strain rate for core K11

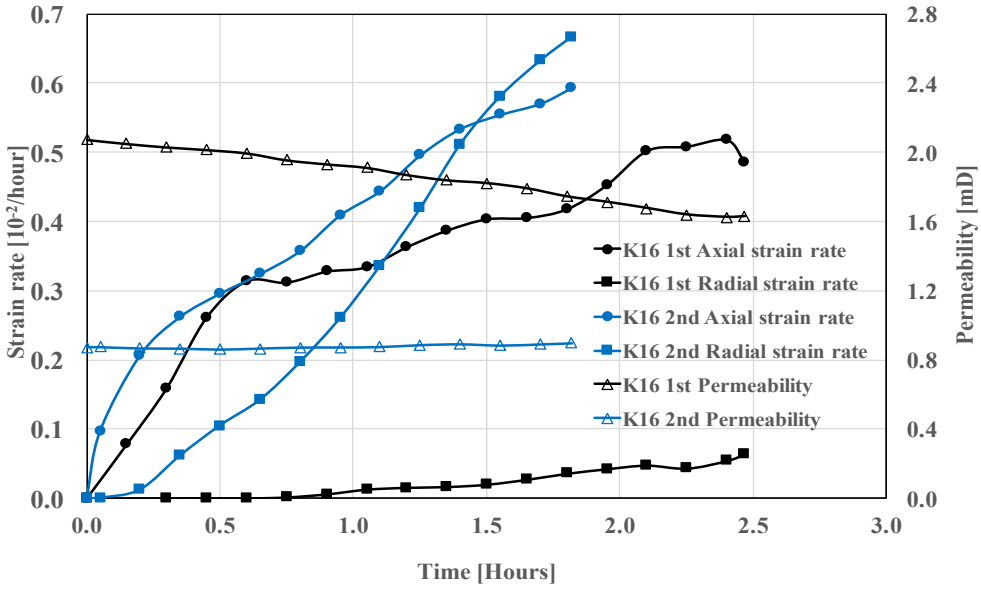

Figure 4.39 Permeability evolution vs. strain rate for core K16

Similar behavior compared to Figure 4.22 is observed for core K11 and K16 in Figure 4.38 and 4.39. The intersection point of radial and axial strain rate in the 2nd deviatoric loading indicates the occurrence of single-band shear failure, which is accompanied with an increase in permeability by creating new microcracks.

4.3.2 Conclusion

In the 1st deviatoric loading, permeability decreases with increasing axial stress. This behavior is similar to the 1st deviatoric loading in test series 2. Good repeatability is exhibited for samples in test series 2 and 3 in the 1st loading. The reduction of permeability in this loading phase is listed in Table 4.7.

Table 4.7 Permeability reduction in 1st deviatoric loading

Sample No.	Ini. Perm. (mD)	End Perm. (mD)	Reduction
K11	2.10	1.62	23%
K16	2.08	1.61	23%

In the next hydrostatic loading, permeability of K11 and K16 experiences continuous decrease. The reduction in permeability is listed in Table 4.8.

Table 4.8 Permeability reduction in subsequent hydrostatic loading

Sample No.	Ini. Perm. (mD)	End Perm. (mD)	Reduction
K11	1.55	1.02	34%
K16	1.50	0.94	37%

Compared to the reference hydrostatic loading in test series 1, the end permeability for K11 and k16 are similar to K5 and K12, indicating that the effect of the 1st deviatoric loading does not influence the end permeability in the subsequent hydrostatic loading.

In the 2nd deviatoric loading, permeability remains almost constant due to the occurrence of shear failure. The end permeability after the 2nd devaitoric loading cycle is 0.92 mD for K11 and 0.88 mD for K16. This result demonstrates that despite the enhancement of shear failure on permeability, the end permeability after the three

successive loading cycles is much lower than the initial permeability.

4.2.4 Test series 4

For the purpose of obtaining a better understanding of the chalk behavior at low confining pressure, chalk cores are initially loaded hydrostatically to 1.2 MPa and all the deviatoric loading tests are conducted at 1.2 MPa confining pressure in this test series. The two samples used in this section are K10 and K20 with porosities of 39.29% and 39.18% respectively. The test schemes are listed in Table 4.9.

Table 4.9 Properties and test schemes of Core K10 and K20

Loading	***Confining Pressure (MPa)***		***Piston Pressure (MPa)***		***Creep Time (Days)***	
Cycle	***K10***	***K20***	***K10***	***K20***	***K10***	***K2-***
1st DL	1.2	1.2	5.5 Max.	6.6 Max.	/	/
1st DC			3.2	3.8	0.9	2.7
2nd DL			3.6 Max.	4.9 Max.	/	/
2nd DC			2.9	3.5	3.0	2.0
3rd DL			3.8 Max.	4.8 Max.	/	
3rd DC			3.3	3.5	1.0	3.0

4.4.1 Results

1st Deviatoric Loading Phase. For the 1st deviatoric loading performed at lower confining pressure, the ability of the samples to resist load is significantly lower than the samples loaded at 3 MPa confining pressure. A sudden sharp increase in permeability is observed from the Figure 4.40 and 4.41 for K10 and K20 when failing in shear failure mode. In order to avoid the cores from failing, 1 MPa piston pressure is reduced before initiating the creep phase for K20.

Before reaching the peak axial stress, increase in radial strain is relatively low, whereas, after reaching the peak axial stress, the change in radial strain is accelerated, which is observed to be 0.12% between the points circled on Figure 4.41.

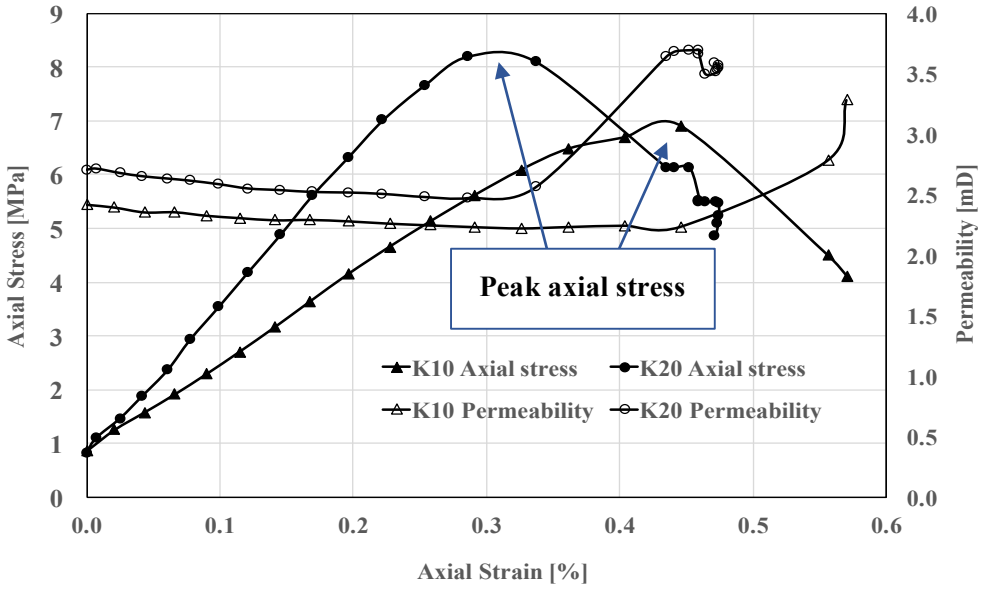

Figure 4.40 1st Deviatoric loading for core K10 & K20 at 1.2 MPa confining pressure

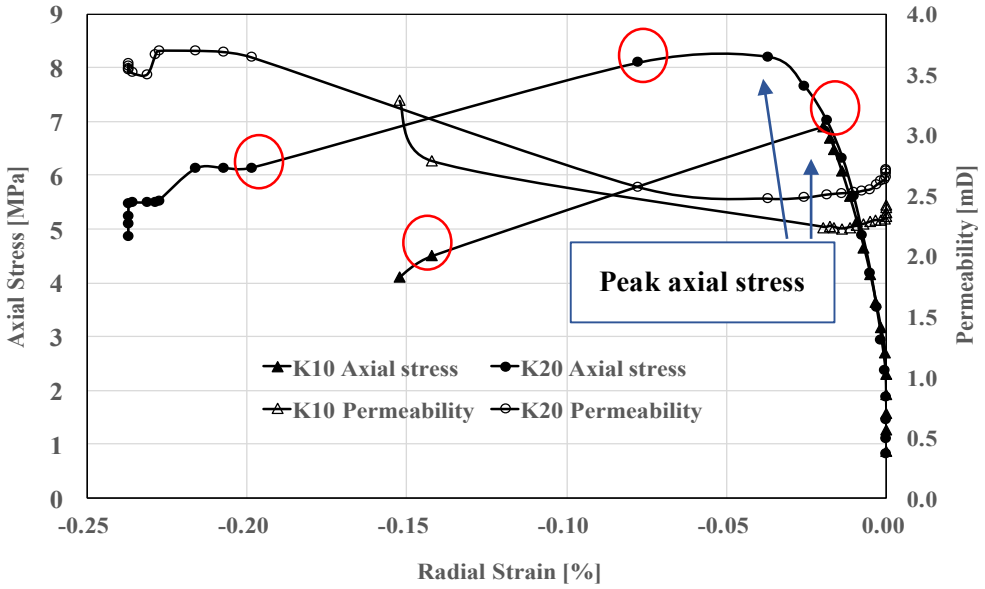

Figure 4.41 1st Deviatoric loading for core K10 & K20 at 1.2 MPa confining pressure

1st Creep Phase. In the following creep phase, the permeability for K10 remains almost constant at 3.1 mD (Figure 4.42), however, K20 experiences a slight decrease of 0.3 mD in permeability as a consequence of longer creep time and 0.5 MPa higher constant stress load.

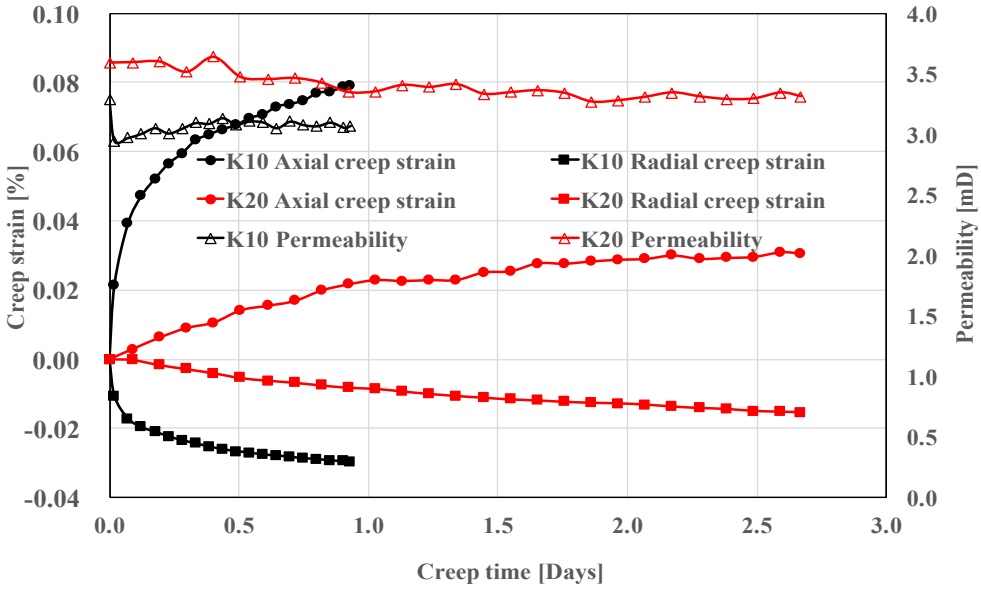

Figure 4.42 1st Creep phase for core K10 & K20 at 1.2 MPa confining pressure

2nd Deviatoric Loading Phase. In this loading phase, K10 and K20 are loaded deviatorically up to a peak axial stress, after which loading continues before setting a fixed piston pressure (circled on Figure 4.43). In order to prevent cores from failing, additional 0.5 MPa and 1 MPa piston pressure for K10 and K20 is reduced respectively before initiating the creep phase at the end of loading.

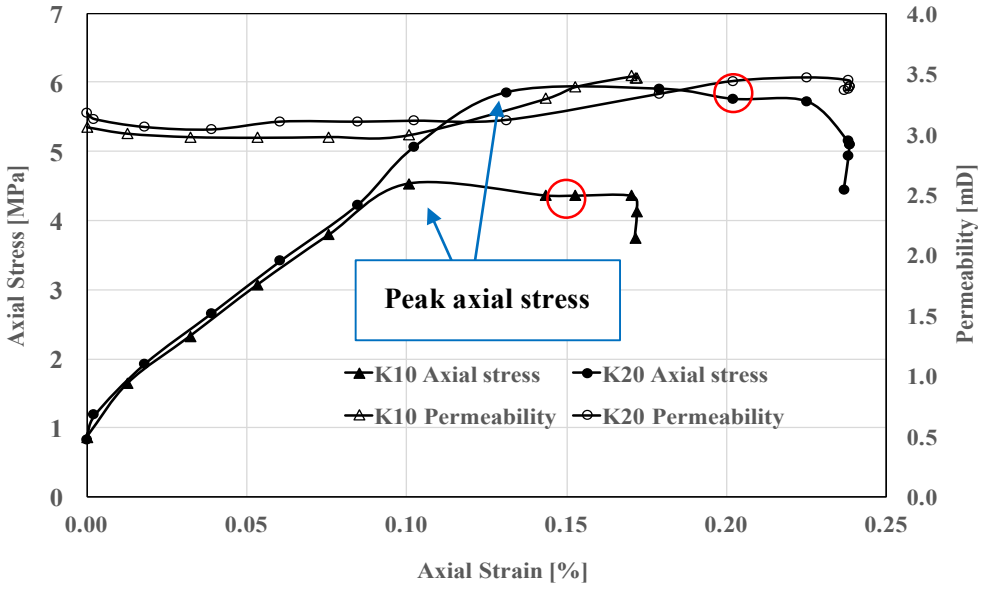

Figure 4.43 2nd Deviatoric loading for core K10 & K20 at 1.2 MPa confining pressure

Figure 4.43 shows constant permeability before reaching the peak axial stress. After the peak axial stress, a slight increase of 0.3 mD appears. This permeability increase is

observed at the axial strain of 0.10% for K10 and 0.13% for K20.

Before 2.5 MPa axial stress, the radial strain of K10 and K20 remains almost zero. (Figure 4.44). The changes in radial strain between the circled points for each curve are 0.04% and 0.08% for K10 and K20 respectively. However, in the 1st deviatoric loading, the numbers are around 0.12%.

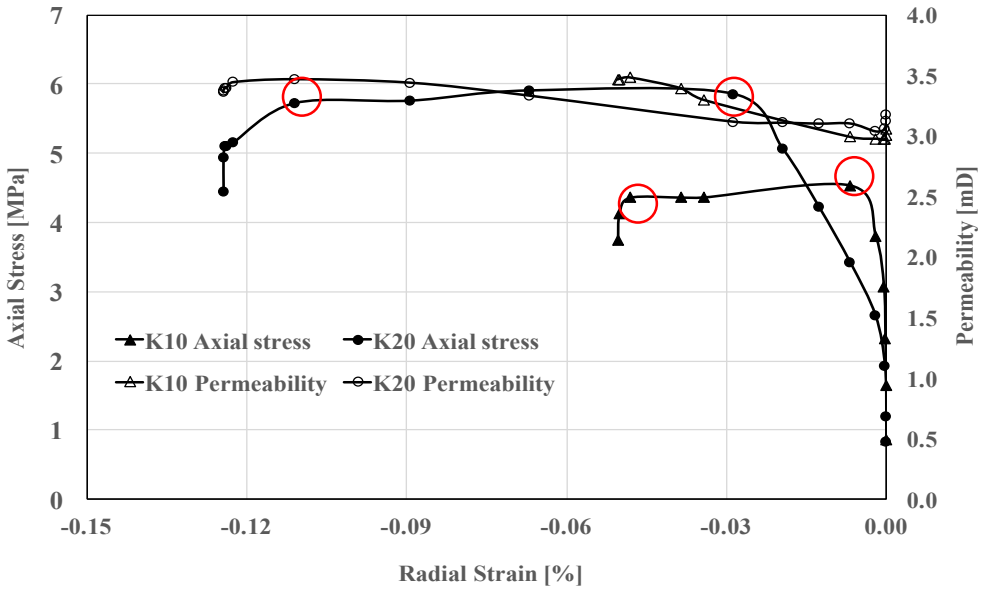

Figure 4.44 2nd Deviatoric loading for core K10 & K20 at 1.2 MPa confining pressure

2nd Creep Phase. K10 and K20 are set to creep at constant piston pressure of 2.9 and 3.5 MPa respectively (Figure 4.45).

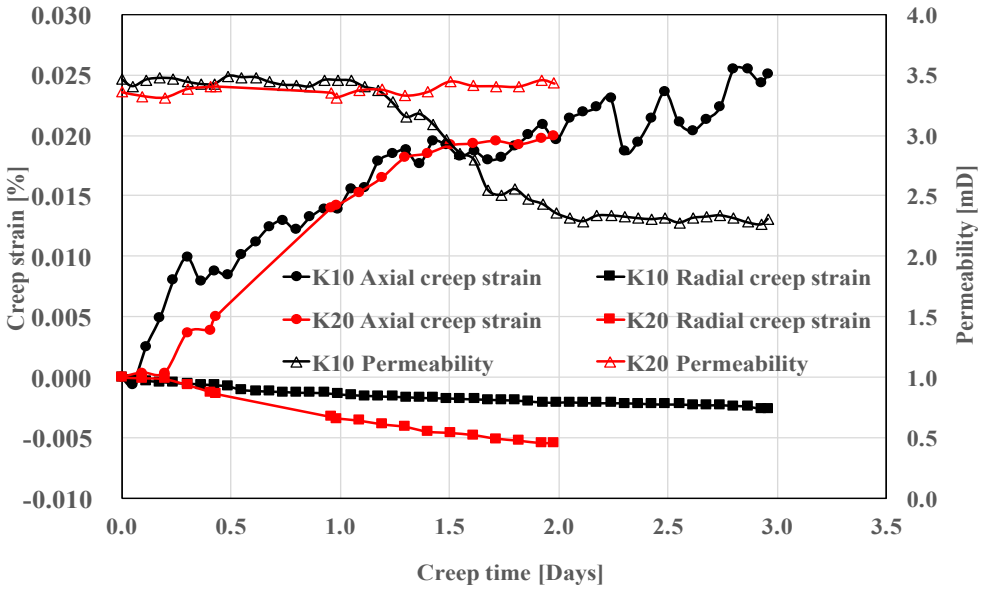

Figure 4.45 2nd Creep phase for core K10 & K20 at 1.2 MPa confining pressure

Permeability of K10 is almost constant in the first day of creeping. However, a gradual decrease of 1.2 mD appears in the second creep day and flattens out afterwards. On the other hand, K20 experiences no significant change in permeability during creep.

3rd Deviatoric Loading Phase. A third deviatoric loading is performed by applying axial stress up to 4.7 MPa and 6 MPa respectively for K10 and K20 (Figure 4.46 and 4.47). In order to avoid cores from failing, 0.5 MPa and 1 MPa of piston pressure for K11 and K20 are reduced respectively before the start of 3rd creep phase.

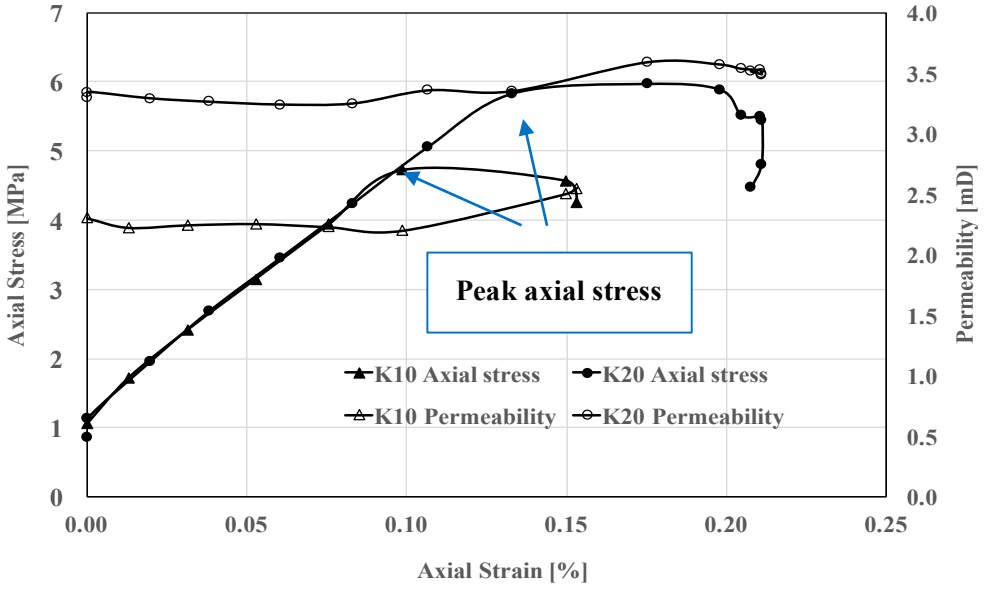

Figure 4.46 3rd Deviatoric loading for core K10 & K20 at 1.2 MPa confining pressure

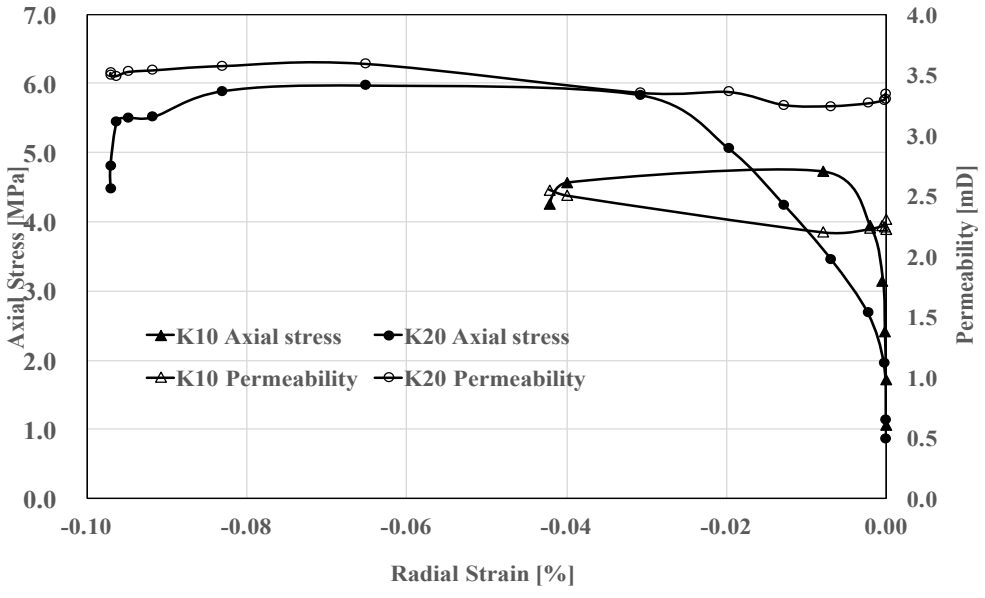

Figure 4.47 3rd Deviatoric loading for core K10 & K20 at 1.2 MPa confining pressure

Before reaching the peak axial stress, the axial stress and strain curve of K10 coincides well with K20 (Figure 4.46). The permeability evolution trend in this loading phase is similar to that in the 2nd deviatoric loading (Figure 4.43). Constant permeability is observed before the peak axial stress, whereas, increase in permeability is initiated up to 0.2 mD after the point of the peak axial stress.

3rd Creep Phase. No significant change in permeability is observed for both samples (Figure 4.48) in this creep phase.

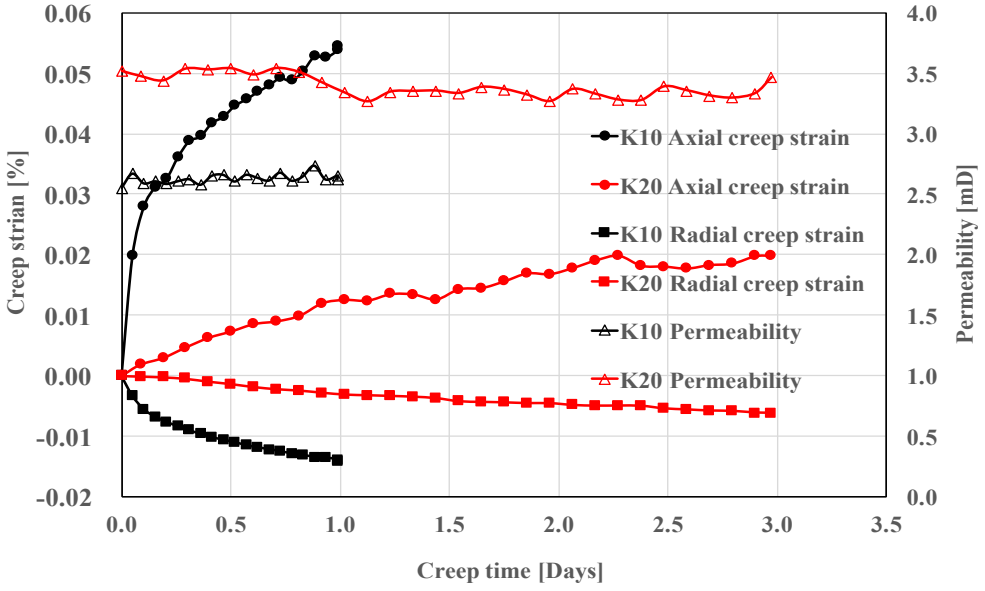

Figure 4.48 3rd Creep phase for core K10 & K20 at 1.2 MPa confining pressure

Relation between Permeability Evolution and Strain Rate. The strain rate effect on permeability during the three successive deviatoric loadings is studied (Figure 4.49 and 4.50).

Unlike the results observed in test series 2 and 3, the symbol of single shear-band failure for K10 appears in all the three deviatoric loadings. Permeability increase is observed at the point where the radial strain rate starts to increase rapidly.

As for K20, the intersection of strain rate curves appears in the first two deviatoric loadings. In the 3rd deviatoric loading, even though no intersection point is observed, the difference between the axial and radial strain is very small.

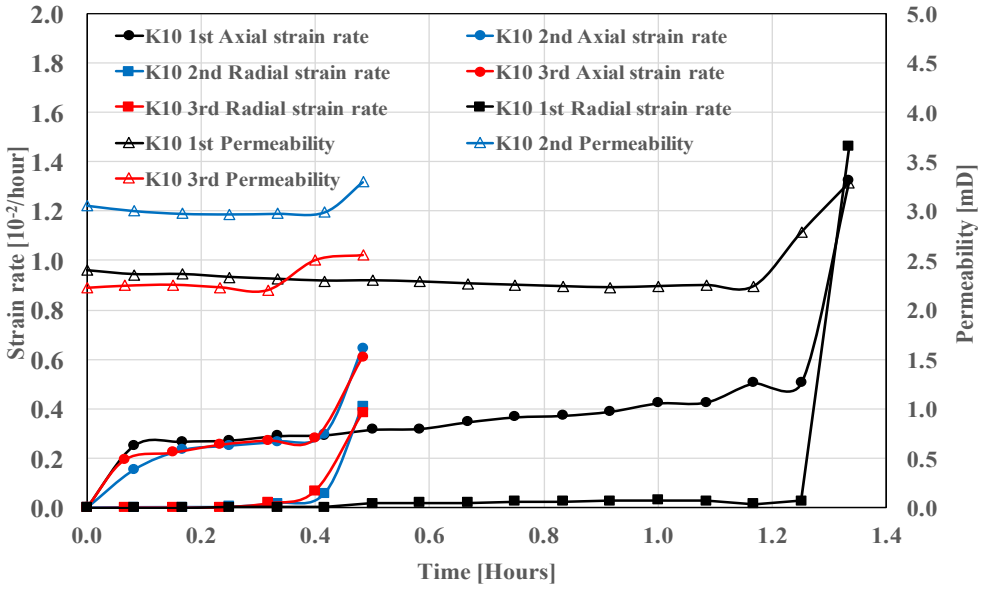

Figure 4.49 Permeability evolution vs. strain rate for core K10

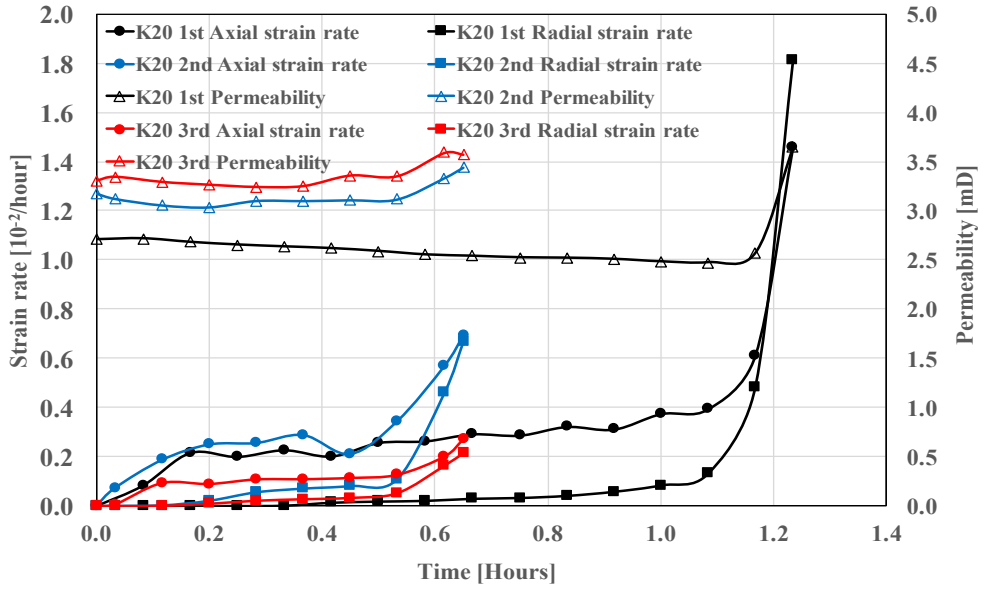

Figure 4.50 Permeability evolution vs. strain rate for core K20

4.4.2 Conclusion

The three successive deviatoric loadings are conducted at 1.2 MPa confining pressure, therefore, chalk samples behave more brittle in this test series. The similarity observed in the three successive deviatoric loadings is the permeability increases at the point where shear failure occurs. The initial and end permeability (before reducing piston pressure) in the three successvie loadings are listed in Table 4.10.

Table 4.10 Permeability reduction in 3 successive deviatoric loadings

Loading No.	Ini. Perm. (mD)	End Perm. (mD)	Increase
K10 1st	2.42	3.29	35%
K20 1st	2.71	3.70	37%
K10 2nd	3.06	3.47	13%
K20 2nd	3.18	3.46	9%
K10 3rd	2.36	2.55	8%
K20 3rd	3.33	3.57	7%

Consistent increase in permeability is observed in each loading phase. Table 4.10 also shows that the increment in permeability decreases after each loading cycle and both samples obtained higher end permeability than initial permeability.

The relation between permeability and strain rate suggests that chalk loaded at lower confining pressure is more likely to induce shear failure with increasing axial stress, which will in turn act to enhance the permeability.

4.2.5 Test series 5

Core K19 and K24 with porosities of 38.61% and 39.12% are used in this test series respectively. The test schemes are listed in Table 4.11.

Table 4.11 The test schemes of Core sample K24 and K19

Loading	***Confining Pressure (MPa)***		***Piston Pressure (MPa)***		***Creep Time (Days)***	
Cycle	***K19***	***K24***	***K11***	***K16***	***K11***	***K16***
1st DL	1.2	1.2	5.8 Max.	5.5 Max.	/	/
1st DC			3.9	3.5	2.8	1.9
1st HL	16.3 Max.	15.3 Max.	1.6 Max.	1.55 Max.	/	/
1st HC	16.3	15.3	1.6	1.55	1.8	0.8
2nd DL	1.2	1.2	5.0	4.5 Max.	/	
2nd DC			3.5	3.5	5.0	2.0

4.5.1 Results

1st Deviatoric Loading Phase. K19 and K24 and loaded deviatorically up to 6.9 and 7.2 MPa axial stress respectively (Figure 4.51 and 4.52).

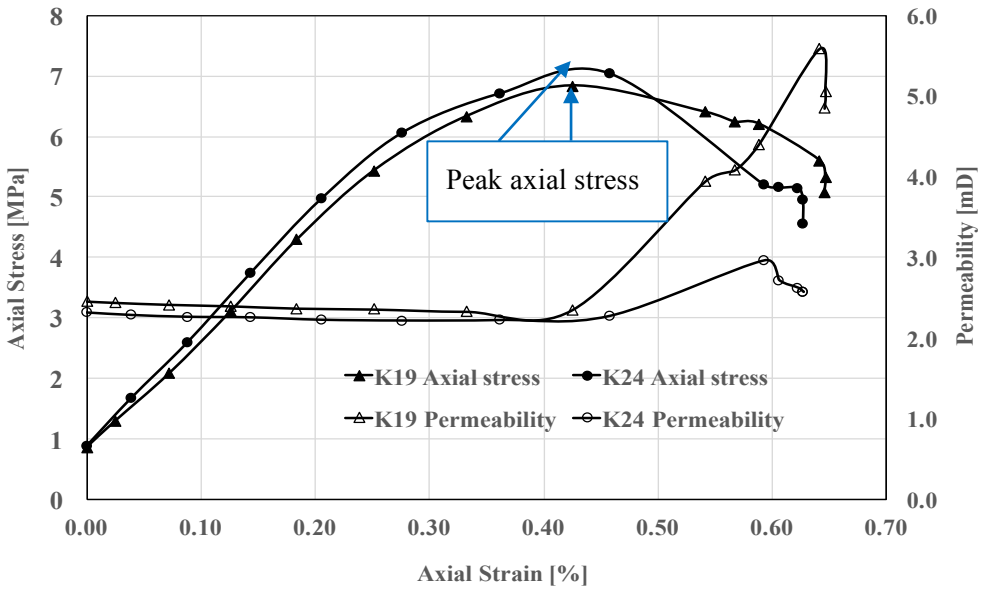

Figure 4.51 1st Deviatoric loading for core K19 & K24 at 1.2 MPa confining pressure

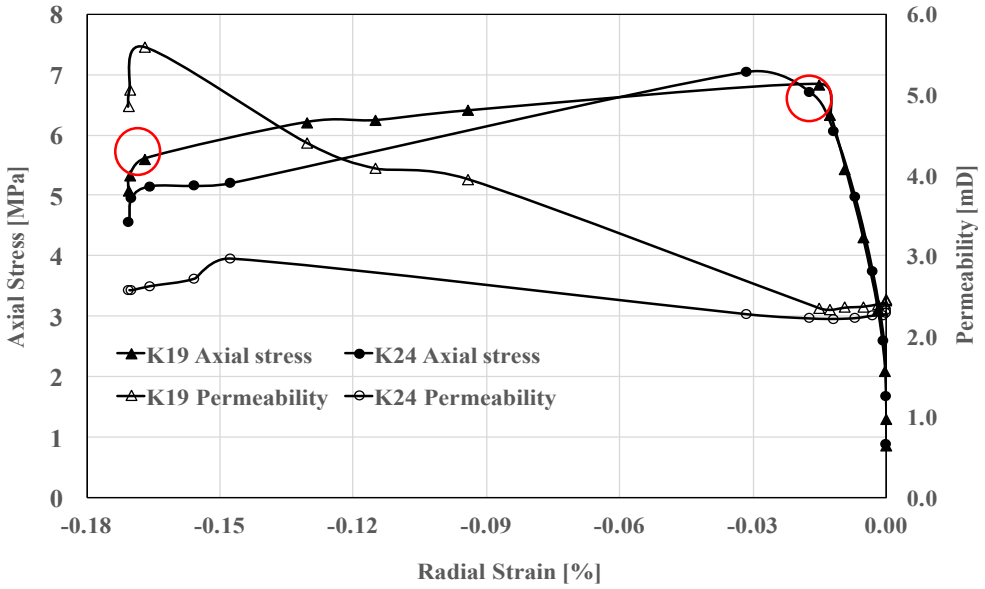

Figure 4.52 1st Deviatoric loading for core K19 & K24 at 1.2 MPa confining pressure

From the beginning until reaching the peak axial stress, roughly at 0.4% axial strain (Figure 4.51), permeability remains almost constant and the stress-strain curve of K19

coincides with K24 (Figure 4.52). After the peak axial stress, permeability is increased from 2.2 mD to 5.8 mD for K19 and 3.0 mD for K24. The drastic acceleration of deformation in the radial direction appears at around 0.03% radial strain (Figure 4.52), where permeability increase is observed.

1st Creep phase. K19 and K24 are set to creep at a fixed piston pressure of 4 and 3.5 MPa respectively. Figure 4.53 shows that permeability remains almost constant throughout the creep period.

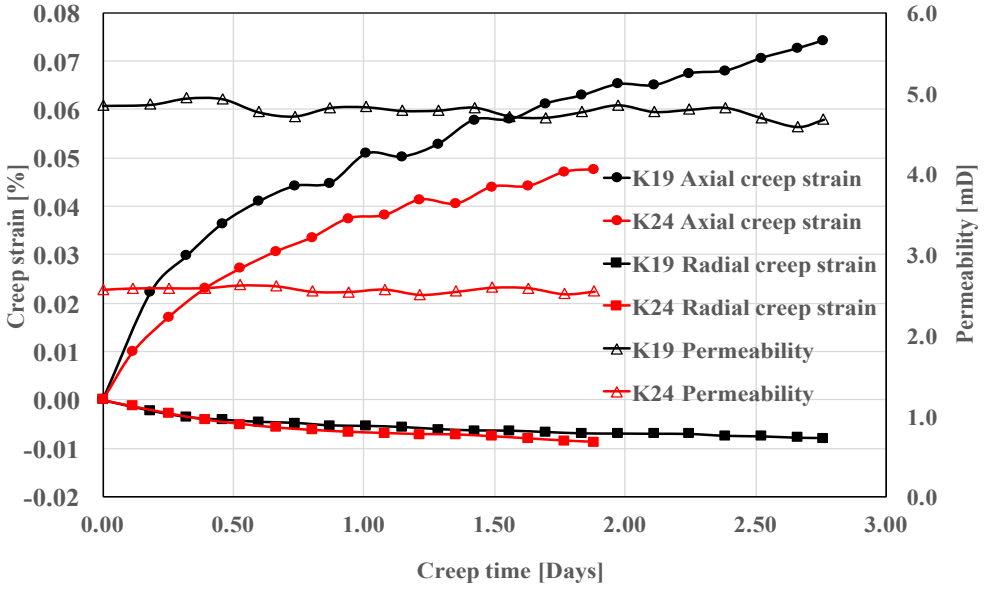

Figure 4.53 1st Creep phase for core K19 & K24 at 1.2 MPa confining pressure

Hydrostatic Loading Phase. In this loading phase, K19 and K24 are loaded hydrostatically up to 15.3 and 16.3 MPa confining pressure respectively.

Effective confining stress and permeability are plotted against axial strain in Figure 4.54, showing that the hydrostatic loading leads to a decrease in permeability. The end permeability for both samples is around 1.3 mD, which is close to the end permeability for sample K11 (1.04 mD), but 0.4 mD higher compared to K5, K12 and K16. The two permeability-strain curves converge at 6 MPa effective confining stress (Figure 4.55).

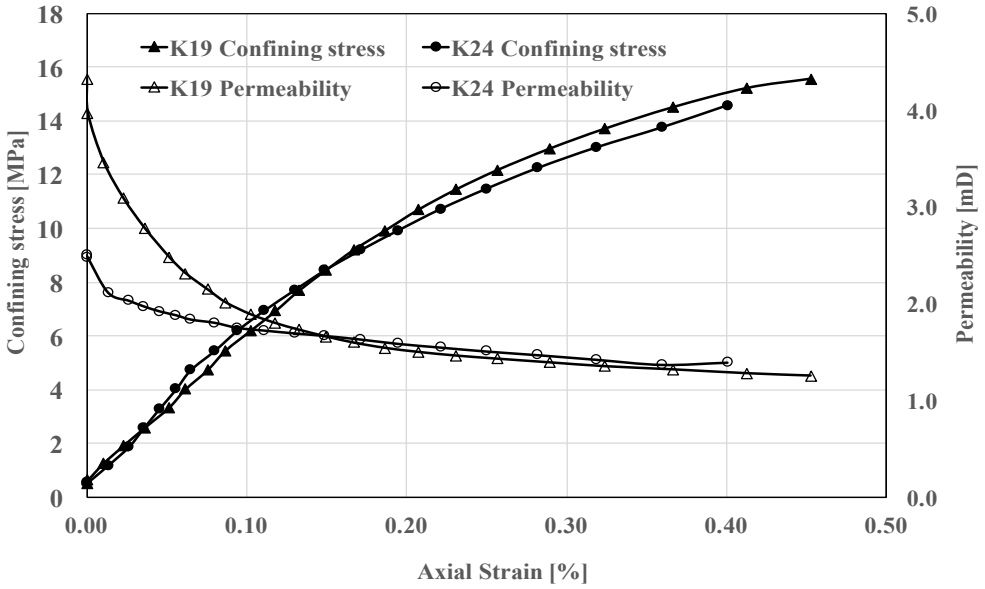

Figure 4.54 Hydrostatic loading for core K19 & K24 untill 16 & 15 MPa confining pressure

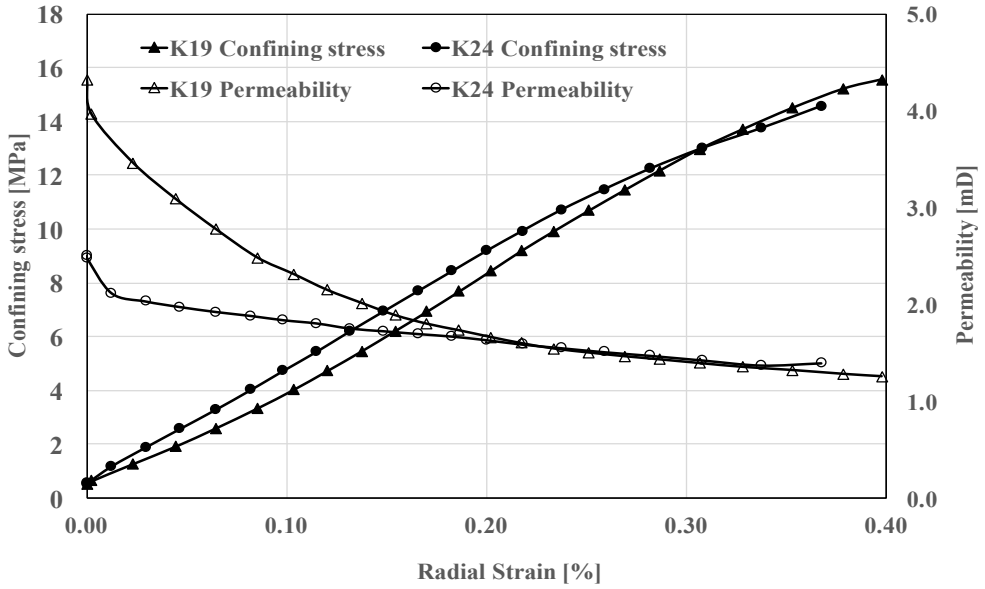

Figure 4.55 Hydrostatic for core K19 & K24 loading utill 16 & 15 MPa confining pressure

2nd Creep Phase. The creep phase of K19 and K24 is initiated when samples are set to creep at constant 16.3 MPa and 15.3 MPa confining pressure respectively. Figure 4.56 shows a decrease of 0.1 mD in permeability for both samples at the end of the creep phase.

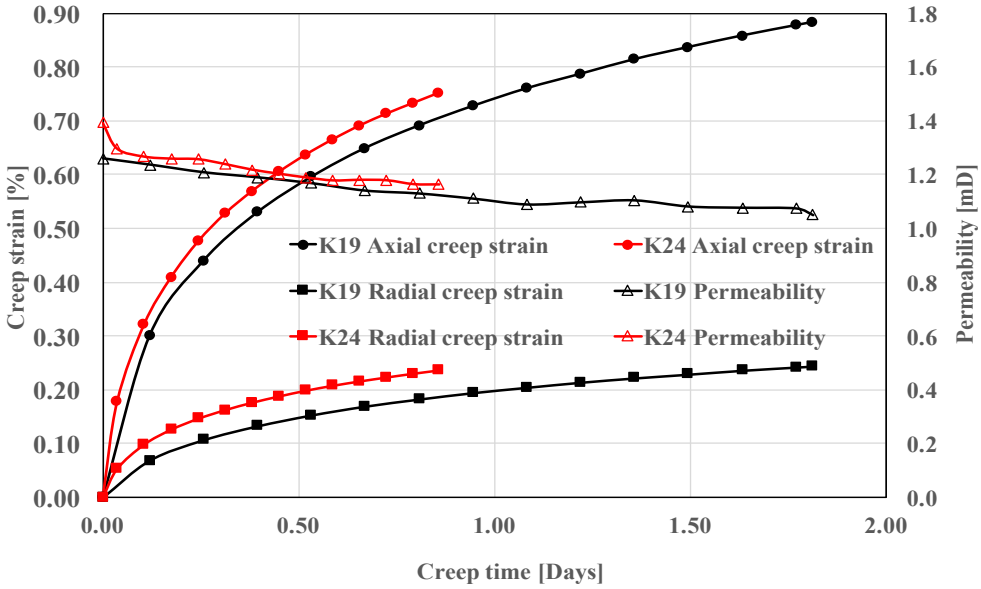

Figure 4.56 2nd Creep phase for core K19 & K24at 16 & 15 MPa confining pressure

2nd Deviatoric Loading Phase. After the samples have been rested for 24 hours, the 2nd deviatoric loading is performed. K19 and K24 are loaded deviatorically up to an axial stress of 6.0 MPa and 5.75 MPa respectively. After the peak axial stress, loading continues before setting a fixed piston pressure. Additional 1 MPa piston pressure for K19 and 0.5 MPa piston pressure of K19 is reduced gradually with a constant ramping rate of 1 MPa/min before initiating the creep phase for the purpose of preventing the cores from failing.

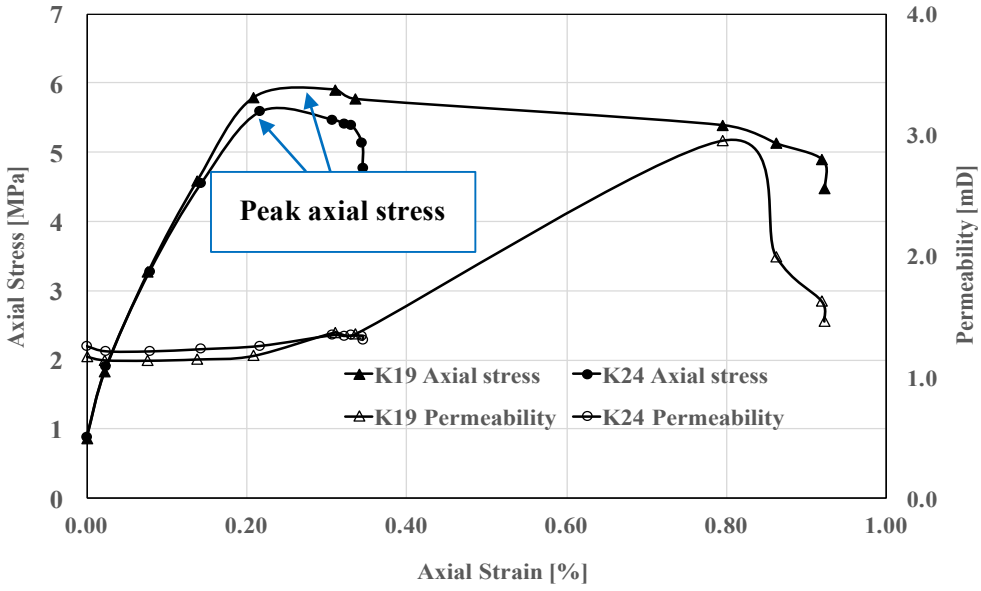

Figure 4.57 2nd Deviatoric loading for core K19 & K24 at 1.2 MPa confining pressure

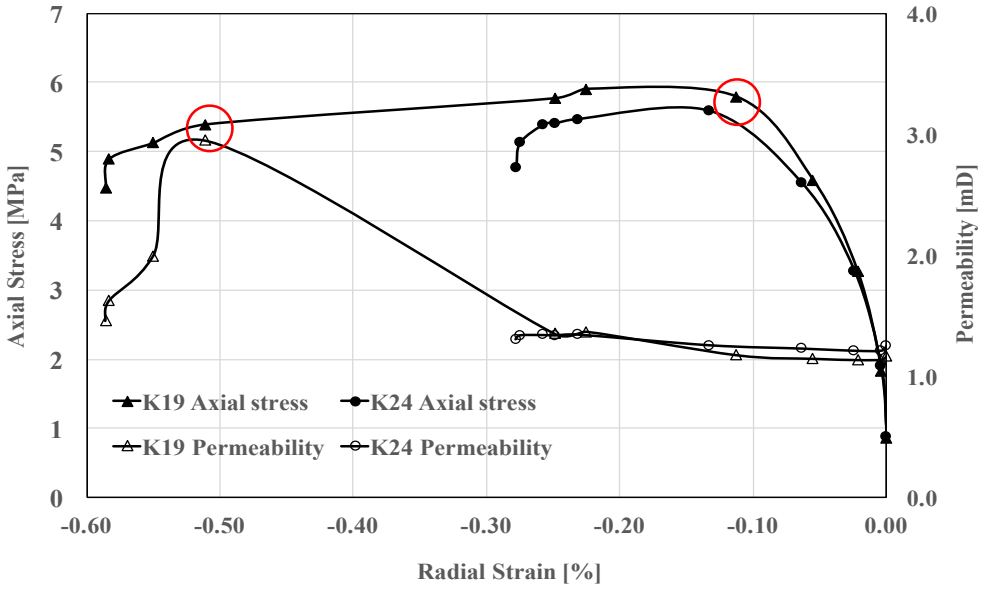

Figure 4.58 2nd Deviatoric loading for core K19 & K24 at 1.2 MPa confining pressure

Before the peak axial stress, permeability of K19 and K24 remains constant (Figure 4.57). After the peak axial stress, permeability of K24 is increased slightly, 0.13 mD, however, a sharp increase of 2 mD in permeability is observed for core K19. During the ramping period of 1 MPa piston pressure, permeability of K19 is decreased.

The two circled points on Figure 4.58 are the peak axial stress and initiation of ramping activity. The difference of radial strain between the two points is 0.4%, which is 2.5 times higher than the value in the 1st deviatoric loading for K19 (Figure 4.52).

In order to further investigate the sudden sharp increase in permeability, the radial strain and permeability are plotted against the loading time in Figure 4.59. It is observed that from 0.6 to 0.85 hour, core tends to deform more rapidly in the radial direction upon shear failure. As loading continues, a slight decrease of 0.05 mD in permeability is shown at approximately 0.86 hour, where the deformation in the radial direction is slowed down as well. This slight decrease in permeability is then followed by drastic increase in both radial strain and permeability at 0.9 hour. It is assumed that potential shear sliding along the shear band created by the shear failure accounts for the drastic increase in permeability.

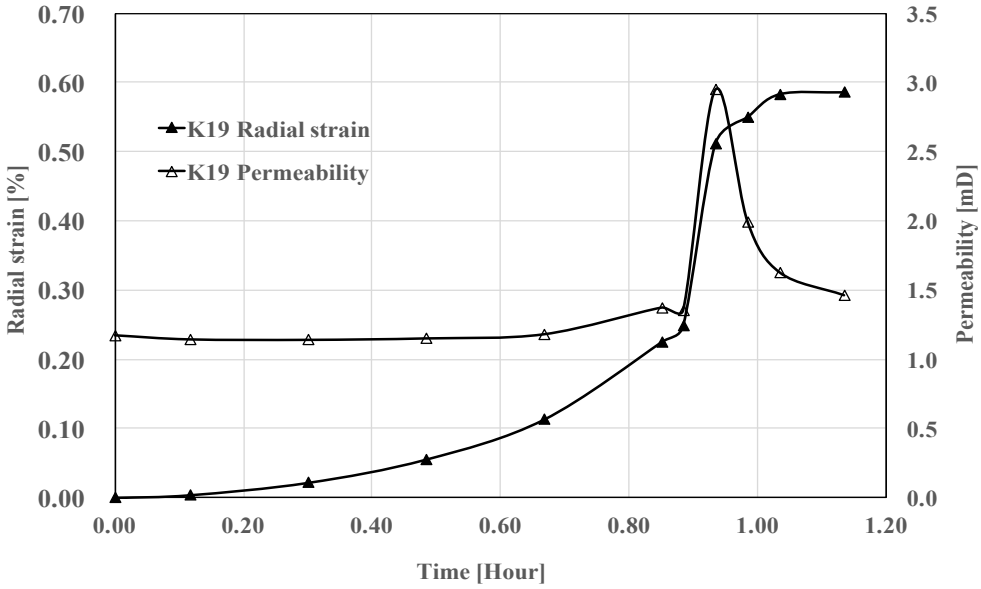

Figure 4.59 Radial strain and Permeability change with loading time for core K19

3rd Creep Phase. Figure 4.60 shows constant permeability along creep time. At the end of the creep phase, the flooding brine for K19 is switched to distilled water since the brine has been run out.

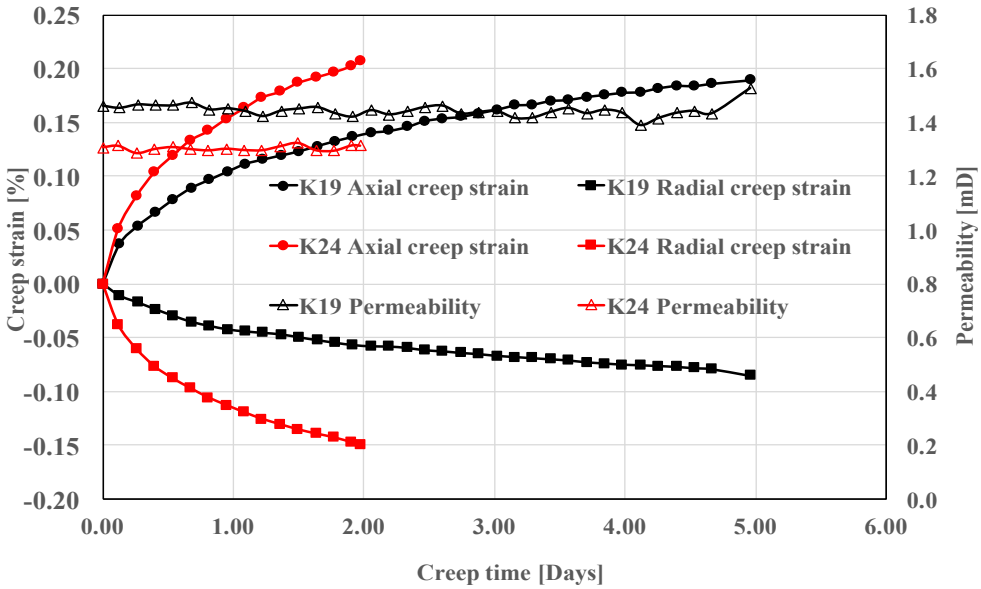

Figure 4.60 3rd Creep phase for core K19 & K24at 1.2 MPa confining pressure

3rd Deviatoric Loading Phase. A third deviatoric loading is performed for K19. No significant change in permeability is observed from Figure 4.61 in the loading period from 0 to 0.14% axial strain.

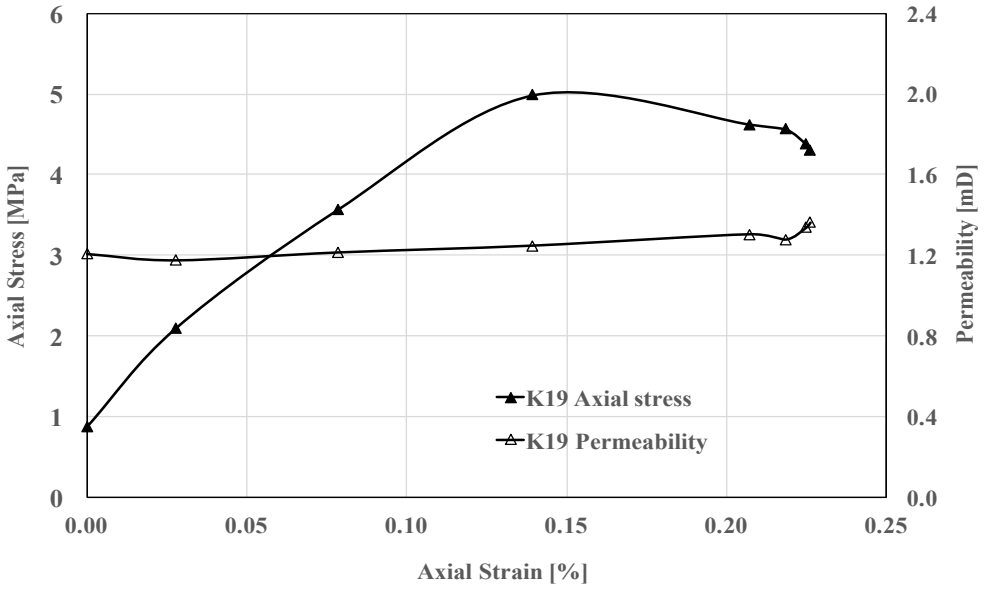

Figure 4.61 3rd Deviatoric loading for core K19 at 1.2 MPa confining pressure

4th Creep Phase. K19 is left to creep for three days. Permeability remains almost constant throughout this period (Figure 4.62).

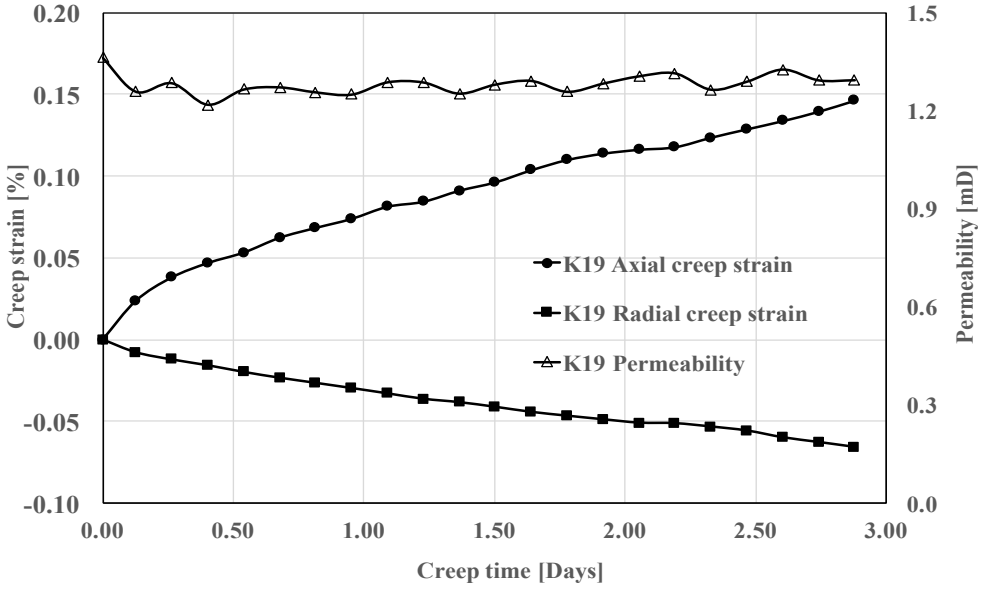

Figure 4.62 4th Creep phase for core K19 at 1.2 MPa confining pressure

Relation between Permeability Evolution and Strain Rate. Different behaviors are observed (Figure 4.63 and 4.64) in this test series compared to test series 4 that the occurrence of the critical point is in the 2nd deviatoric loading, rather than both loadings. Even though the radial strain rate is lower than axial strain rate in the 1st loading phase, the difference between these two strain rate is very small. Therefore, it can be assumed

that if the specimen is loaded more time before setting a fixed piston pressure, radial strain rate might end up surpassing axial strain rate.

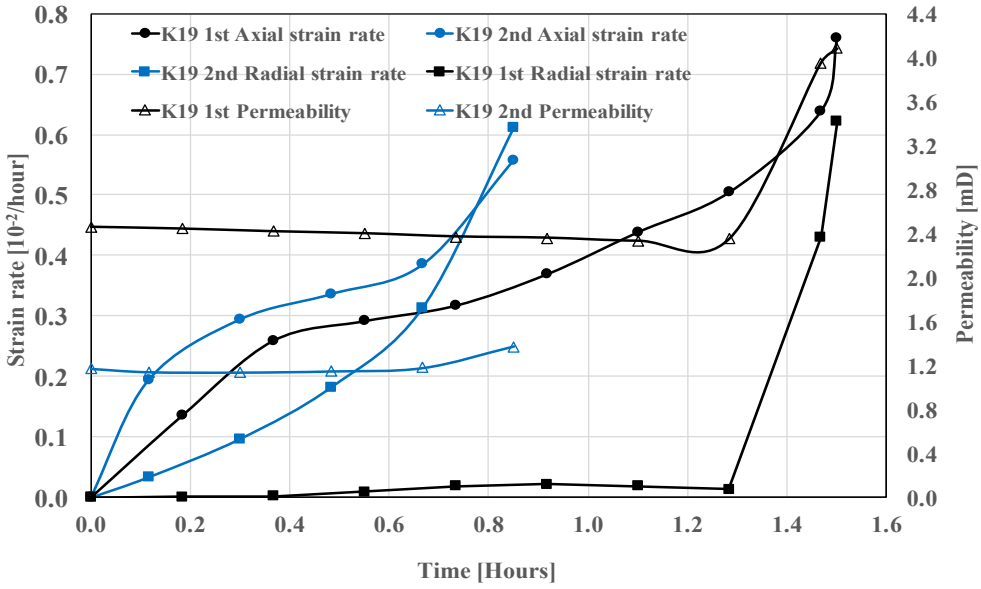

Figure 4.63 Permeability evolution vs. strain rate for core K19

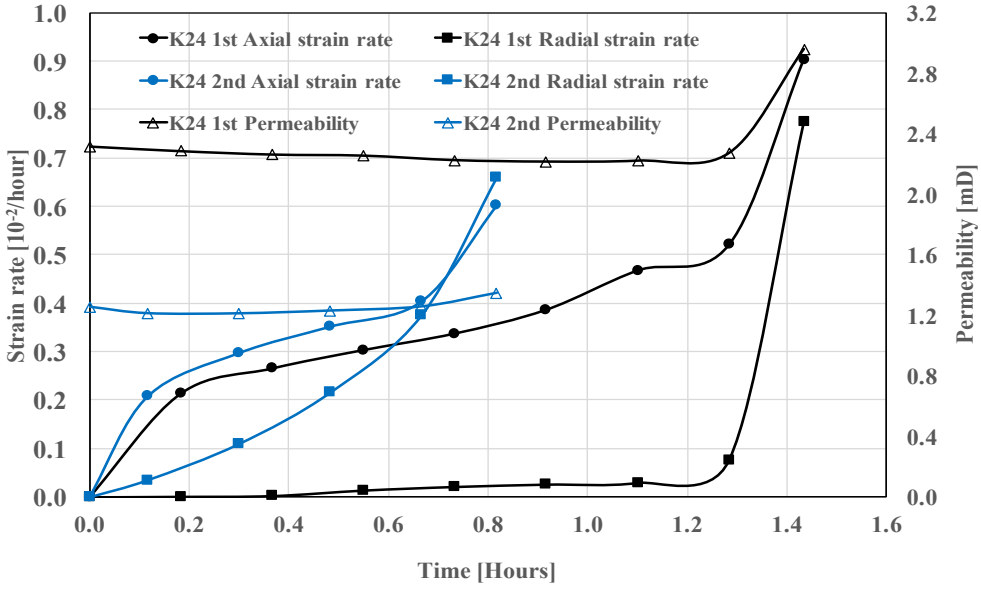

Figure 4.64 Permeability evolution vs. strain rate for core K24

4.5.2 Conclusion

Three successive loadings are performed in this test series. Table 4.12 summarizes the permeability evolution after each loading.

Table 4.12 Permeability evolution in 3 successive loadings

Loading No.	Ini. Perm. (mD)	End Perm. (mD)	Increase
K19 1st	2.46	5.58	127%
K24 1st	2.31	2.96	28%
K19 2nd	4.32	1.26	71% (Reduction)
K24 2nd	2.50	1.39	44% (Reduction)
K19 3rd	1.17	2.95	152%
K24 3rd	1.25	1.35	8%

The 1st deviatoric loading shows significant increase in permeability when shear failure occurs. The subsequent hydrostatic loading reduces the permeability down to 1.26 and 1.39 mD. Unlike the scenario in test series 3, permeability is increased in the 3rd deviatoric loading.

Assumptions of potential shear sliding after shear failure is made for core K19 during the 2nd deviatoric loading. This behavior is seen to contribute to the instant and sharp increase in permeability.

Figure 4.65 Core K19 after the test

The image of the core K19 after all test sequences is shown in Figure 4.65 with clear identification of singe shear-band failure and possible potential for slippage.

Chapter 5 Discussion

This Chapter highlights the discussions based on the laboratory results and comments in Chapter 4. The relation between the different test sequences, as well as each individual loading and its impact on permeability evolution are discussed. Appropriate approaches are attempted to explain the mechanical behaviors or phenomenon occurred in the experiments. A clearer understanding of the different stress states influences on permeability of chalk reservoirs should be established.

5.1 Effect of hydrostatic and deviatoric loading

The laboratory experimental results obtained in Chapter 4 provide realistic test numbers to establish an approach to explain how stress states and compaction influence the permeability by investigating the stain as a function of effective stress during each test sequences. In this section, the effect of hydrostatic loading and deviatoric loading on permeability is studied.

5.1.1 Hydrostatic loading

Permeability evolution and its dependence on effective stress has been documented by many studies (Fatt et al., 1952; McLatchie et al., 1958; Knutson et al., 1963; Brace et al., 1968; Vairogs et al., 1971). Among these, some suggested that the permeability of rock is only dependent on the effective stress, which is the difference between the confining pressure and pore pressure. It is commonly accepted that ductility increases with increasing confining pressure and temperature, which promotes the transition from brittle to ductile behavior (Zhang et al., 1990).

In the hydrostatic loading experiments, results obtained from test series 1, 3 and 5 show typical sigmoidal function shape of hydrostatic compaction stress-strain curves with continuous reduction in permeability along the axial strain (Figure 5.1). For all the samples plotted in Figure 5.1, there exists three evident permeability evolution phases:

1) In the first phase, with an increase in confining pressure, the microcracks are initially compressed to be closed, thus, permeability decreases rapidly along axial strain.
2) In the 2nd phase, the compression of the specimen becomes more difficult compared to the first phase, permeability sensitivity to stress is evidently reduced, whereas, the decrease in permeability continues. The behavior of the chalk is considered to be liner elastic in this phase.
3) The 3rd phase can be characterized as the development of inelastic deformation process such that the decreasing rate of permeability is slowed down when loaded above yield strength, resulting in slight growth and coalescence of microcraks and fractures. (Zhang et al., 2015).

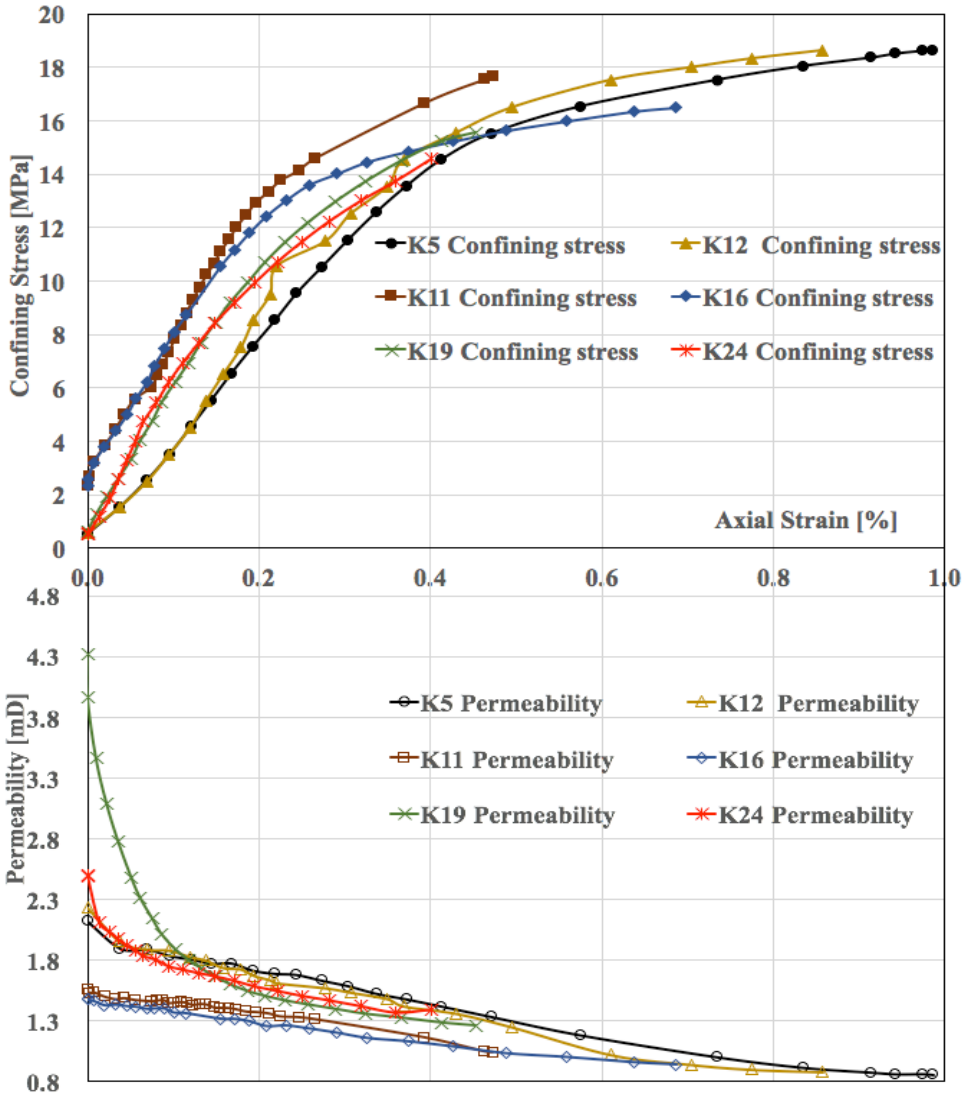

Figure 5.1 Comparison of all samples under hydrostatic loading

Due to the influence of the deviatoric loading performed prior to hydrostatic loading, the initial permeability of core K19 and K24 (1.2 MPa confining pressure) appears relatively higher than the other four samples, whereas, the permeability of K11 and K16 (3 MPa confining pressure) is relatively lower (Figure 5.1). The decrement of permeability of all the samples in hydrostatic loading generally increases with higher initial permeability. This behavior of chalk is in accordance with the work conducted by McLatchie et al. (1958) in sandstone. This discrepancy in permeability reduction can be explained that with lower initial permeability before the hydrostatic loading, the permeability is less sensitive to the applied overburden stress since the pre-existing fractures and microcracks are less and narrower, therefore, it becomes more difficult to squeeze the pore spaces and higher stress is required for further compaction.

Despite the differences in the initial permeability, the permeability-strain curves of all the 6 samples tend to converge as the loading continues (Figure 5.1). The convergence of the permeability-strain curves suggests that the permeability of chalk experiencing hydrostatic loading is highly dependent on strain. The initial deviatoric loading has minor impact on the end permeability in the subsequent hydrostatic loading. The study of Indraratna et al. (1999) on granite rocks with interconnected fractures also suggests the same that with confining pressure increasing to a certain value, the change of permeability becomes marginal in a permeability-stress curve.

5.1.2 Deviatoric loading

The effect of hydrostatic loading on permeability has been investigated that increasing confining pressure leads to a decrease in permeability. However, the effect of non-hydrostatic loading is considered to be more complicated. Unlike the permeability evolution under hydrostatic loading, both increase and decrease have been reported from laboratory experiments conducted under non-hydrostatic loading (Wong et al., 1997; Zhu et al., 1997; Korsnes et al., 2006; Zhu et al., 2008).

According to the results obtained in Chapter 4, both increase and decrease in permeability are reported in the 1st deviatoric loading. Table 5.1 lists the initial, minimum and maximum permeability for samples loaded at 1.2 MPa confining and 3

MPa confining pressure.

Table 5.1 Permeability in 1st deviatoric loading

Sample No.	**Conf. (MPa)**	**Ini. Perm. (mD)**	**Min. Perm. (mD)**	**Reduction (%)**	**Max. Perm. (mD)**	**Increase (%)**
K6	3.0	1.97	1.62	18.09	1.62	0.37
K9	3.0	1.90	1.49	21.37	1.52	1.47
K11	3.0	2.11	1.61	23.64	1.65	2.42
K16	3.0	2.07	1.62	21.70	1.65	1.48
K10	1.2	2.42	2.23	8.06	3.29	47.73
K20	1.2	2.71	2.47	8.72	3.70	49.66
K19	1.2	2.46	2.33	5.17	5.59	139.64
K24	1.2	2.31	2.27	1.82	2.96	30.24

**Conf. = Confining Pressure*

Based on the data listed in Table 5.1, permeability evolution in 1st deviatoric loading can be classified into two stages:

1) In the first stage, permeability undergoes a decrease to the lowest value.
2) After the lowest value of permeability, either a gradual or sharp increase is likely to occur.

As seen from Table 5.1, samples tested at 3 MPa confining pressure experienced more reduction in permeability in the first stage. The increase of permeability in the second stage can be negligible. The end permeability is 18-20% lower than the initial permeability.

For samples loaded at 1.2 MPa confining pressure, permeability decrease in the first stage is relatively small, whereas, a sharp increase in permeability is observed in the second stage. The samples ended up with a permeability value much higher than the

initial permeability due to the fact that rocks are more brittle under lower confining pressure and the opening-up of microcracks by shear failure can enhance the permeability more evidently. This behavior of shear dilation and permeability enhancement is in accordance with studies conducted by Chalaturnyk et al. (1995) and Collins et al. (2002) on the effect of shear dilation. Thus, it can be concluded that the end permeability in the 1st deviatoric loading is dependent on the confining pressure applied.

5.2 Effect of successive loadings

Each test series in this thesis is conducted using different test sequences designed to simulate the reservoir stress conditions. The impact of hydrostatic loading and deviatoric loading alone on permeability evolution has been investigated and discussed in 5.1, showing that hydrostatic loading leads to a decrease in permeability with closure of microcracks (Brace et al., 1978; David et al., 1994), and increase in permeability is more likely to be found in the deviatoric loading. It is reported in literatures that permeability tends to be dependent on loading path when effective stress is cycled in freshly cored intact crystalline rock samples (Bernabe, 1986). The study conducted by Morrow et al. (1986) on Westerly granite under cyclic loading indicates that the stress cycling has significant influence on the rock permeability and consistent decrease is observed with each hydrostatic loading phase. On the other hand, some laboratory results obtained from tight reservoir samples demonstrate that the performance of hydrostatic loading alone might be misleading in reservoir studies due to the over-estimating variations of rock properties induced by hydrostatic loading, thus, the hydrostatic compaction is less representative for the actual reservoir stress states conditions (Jaumouille et al., 1995). Therefore, the effect of successive deviatoric loadings as well as successive deviatoric and hydrostatic loadings are studied.

5.2.1 Impact of successive deviatoric loadings

The permeability evolution for samples experiencing two successive deviatoric loadings is plotted in Figure 5.2 along effective axial stress. No hydrostatic loading is carried out on these four core samples plotted in Figure 5.2.

Figure 5.2 shows two different permeability evolution paths for two loading scenarios: scenarios of deviatoric loadings performed at 3 MPa confining pressure and 1.2 MPa confining pressure.

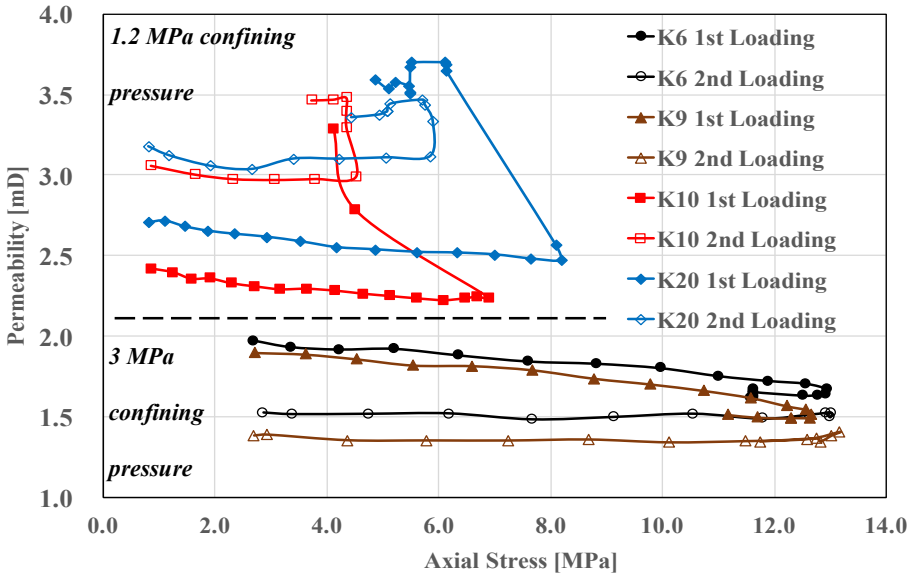

Figure 5.2 Permeability vs. Effective axial stress

3 MPa confining pressure scenario. Continuous decrease in permeability is observed in the 1st deviatoric loading for core K6 and K9 (Figure 5.2). In the 2nd deviatoric loading, permeability remains almost constant. Overall, permeability of the two samples ends up 0.5 mD lower compared to the initial value as a consequence of the two successvie deviatoric loadings.

1.2 MPa confining pressure scenario. K10 and K20 fall into the 1.2 MPa confining pressure scenario. A sharp increase in permeability appears in all the deviatoric loading phases as shear failure occurs. The end permeability for K10 and K20 after two successive deviatoric loadings are increased 31% and 21% respectively compared to the initial permeability.

Comparison between 1.2 MPa and 3 MPa confining pressure scenarios. Core samples which are loaded at 1.2 MPa confining pressure have higher initial permeability values because higher confining pressure is likely to end up with lower permeability. In the 1.2 MPa confining pressure scenario, the occurrence of shear failure enhanced permeability, so that the end permeability appears to be higher than

the initial permeability. In the 3 MPa confining pressure scenario, even though permeability remains unchanged in the 2nd deviatoric loading, however, the initial permeability is still higher than the end permeability. Thus, the effective confining pressure applied throughout the deviatoric loadings plays an important role in the permeability evolution. Lower confining pressure in the deviatoric loading phase tends to result in higher initial and end permeability. In the end, the effect of two successive deviatoric loadings resulted in an enlargement in the difference between the end permeability of the two scenarios.

Two permeability evolution phases are identified in the 2nd deviatoric loading:

1) From the beginning until reaching the peak axial stress, permeability remains almost constant in this phase.
2) As loading continues, increase in axial stress might induce the occurrence of shear failure, after which a slight increase in permeability is exhibited for samples tested at 1.2 MPa confining pressure, whereas, constant permeability is observed for samples loaded at 3 MPa confining pressure.

5.2.2 Impact of hydrostatic loading on subsequent deviatoric loading

Samples plotted in Figure 5.3 experience loading sequences of 1st deviatoric loading, hydrostatic loading, and 2nd deviatoric loading. Permeability evolution in the two deviatoric loadings is plotted against applied axial stress in Figure 5.3. Two different permeability evolution paths along the effective axial stress are observed for two different scenarios.

1.2 MPa confining pressure scenario. As a consequence of the hydrostatic loading performed prior to the 2nd deviatoric loading, the initial permeability in this loading phase is around 1.2 mD (Figure 5.3), which is 2 times lower than the initial permeability prior to the 1st deviatoric loading. The permeability at the end of the 2nd deviatoric loading is 1.3 mD for K24 and 1.5 mD for K19.

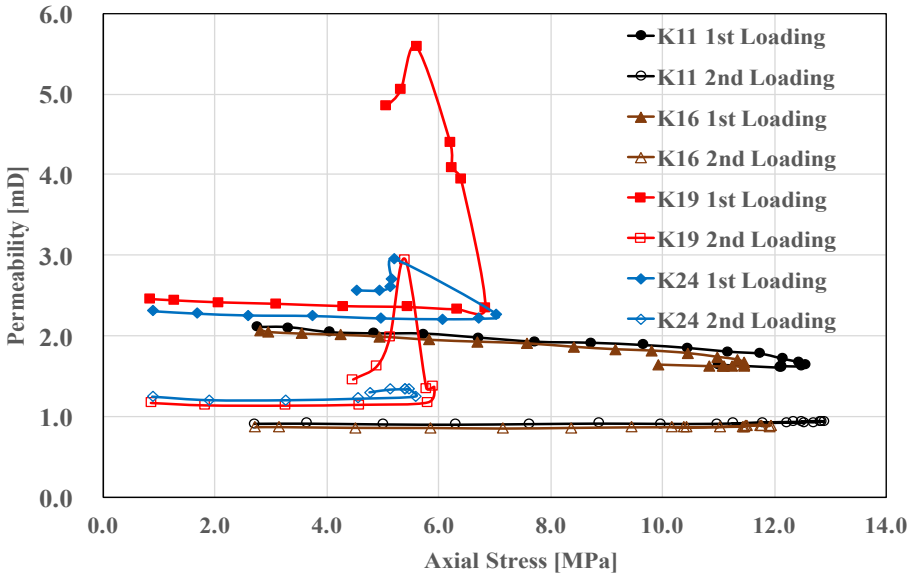

Figure 5.3 Permeability vs. Effective axial stress

3 MPa confining pressure scenario. The hydrostatic loading decreases permeability from 1.8 to 0.9 mD for K11 and K16. The subsequent 2nd deviatoric loading increases permeability to 1 mD due to the occurrence of shear failure. In the end, permeability ends up 2 times lower than initial permeability prior to the 1st deviatoric loading.

As is shown in Figure 5.2, the difference between the end permeability of the two different scenarios are increased after two successive deviatoric loadings. However, when a hydrostatic loading is applied in between the two deviatoric loadings, the difference between end permeability of the two scenarios is significantly reduced.

5.3 Shear failure and strain rate

The effect of shear deformation induced by the deviatoric stress on permeability has been studied by many investigators (Tuefel, 1987; Tuefel et al., 1991; Scott et al., 1994; Zhu et al., 1997; Kelkar et al., 2011). It is found that shear failure in chalk reservoirs contributes to the enhancement of permeability and continuous productivity, which corresponds with the experiment results obtained in this thesis that shear failure induced by both dilation and compression contributes to the increase in permeability.

In naturally fractured reservoirs, i.e. Ekofisk chalk reservoir, the mechanical response

of fractures and the matrix can affect the flow and permeability (Lee et al., 2011). Generally, the fracture or joint apertures are influenced and changed by fracture shear slip and opening. A large increase in permeability is reported from the laboratory experiments conducted by Ye et al. (2017) on the effect of the shear-induced shear slip of granite rock on permeability evolution. The experimental results obtained in Chapter 4, test series 2-4 in this thesis exhibit evident permeability enhancement in deviatoric loading processes.

It is continuously observed in the test series that the occurrence of increase in permeability during loading is accompanied with a relatively rapid deformation in the radial direction. Assumption is made that the occurrence of shear failure can be caused by the accelerated deformation in the radial direction. Therefore, for the purpose of studying the occurrence of shear failure, the axial and radial strain rate of each deviatoric loading is used to determine the shear failure. The study conducted by Heiland (2003) on the influence of strain rate on permeability of low-porosity sandstones demonstrates significant dependence of permeability evolution on strain rate.

According to Figure 4.22, 4.38 and 4.39 in Chapter 4 on the relation between permeability and strain rate for K9, K11 and K16, the gap between the radial strain rate and axial strain rate is lessened after each deviatoric loading. In the 1st deviatoric loading, with a huge gap between the radial and axial strain rate, permeability is likely to decrease with increasing axial stress, however, as the increase in the radial strain rate becomes greater than the axial stran rate, permeability tends to stay constant. The critical point where radial strain rate surpasses axial strain rate appears in the 3rd deviatoric loading, during which either constant or increasing permeability is observed.

Based on the cases of permeability enhancement during deviatoric loadings, the relationships between permeability evolution and strain rate of these cases are plotted in Figure 5.4 and 5.5 respectively for the 1.2 MPa and 3 MPa confining pressure scenarios in order to further investigate the dependence of permeability on strain rate.

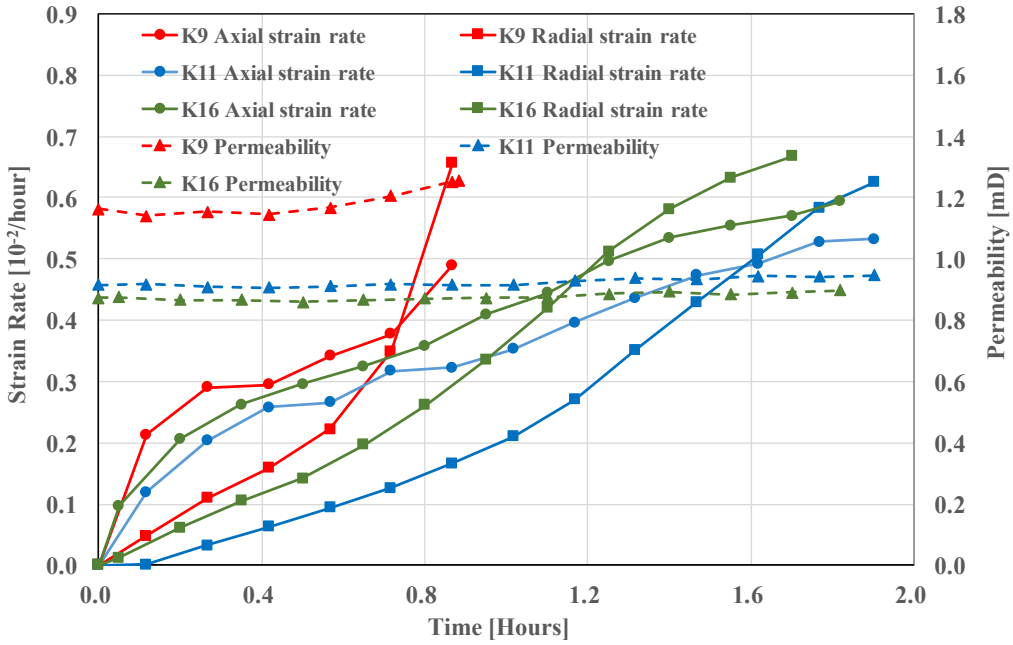

Figure 5.4 Permeability evolution and strain curve at 3 MPa confining pressure

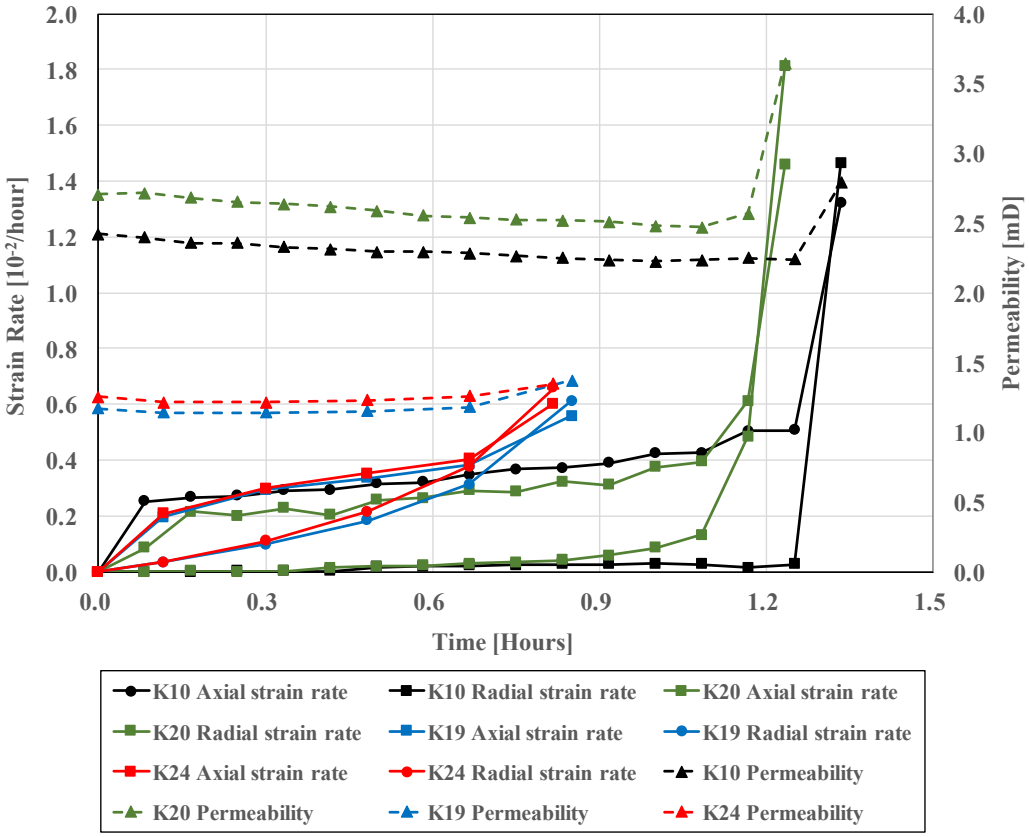

Figure 5.5 Permeability evolution and strain rate at 1.2 MPa confining pressure

As seen from Figure 5.4 and 5.5, when the radial strain rate exceeds the axial strain rate, indicating that the expansion due to dilatancy becomes predominant, permeability increase is initiated. Therefore, it is indicated that the permeability increase induced by shear failure is highly correlated to the strain rate in deviatoric loading. The critical point where the radial strain rate surpass the axial strain rate is considered as the symbol for the occurrence of shear failure.

It is also observed from all the strain rate-permeability figures in Chapter 4 that in the 1.2 MPa confining pressure scenario, the critical point appears in almost all the loading phases, whereas, in the 3 MPa confining pressure scenario, the critical point appears only in the 3rd deviatoric loading. Thus, it can be concluded that the critical point where the radial strain rate surpasses axial strain rate is also dependent on the confining pressure in deviatoric loading.

5.4 Impact of creep failure

Core K5, K6 and K12 failed in the early creep stage within one hour. Figure 5.6 shows the impact of fast creep failure on permeability and strain rate within the testing range of extensometer.

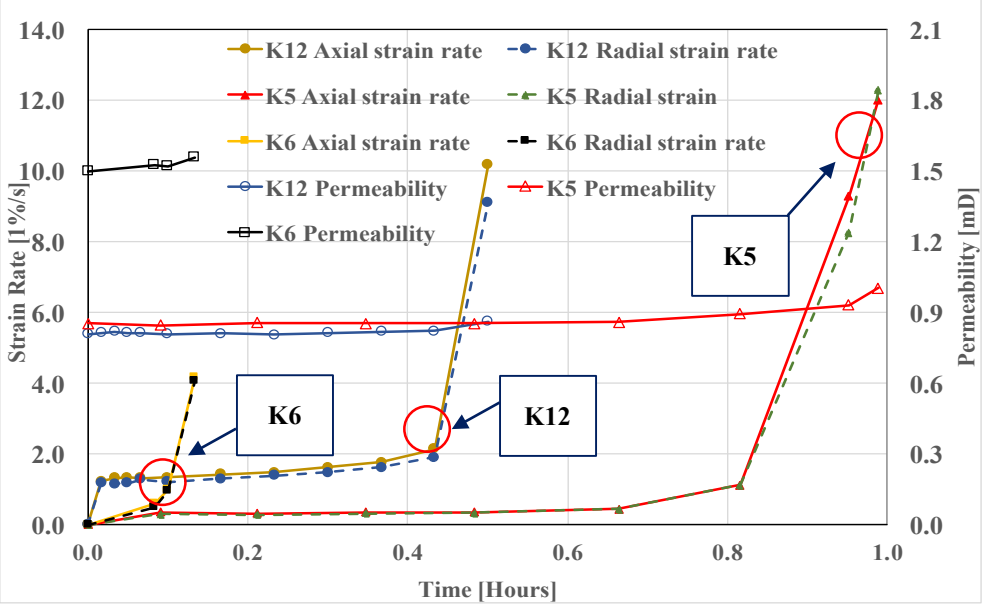

Figure 5.6 Permeability evolution and strain rate

A sharp increase in both axial and radial strain rate is initiated at the time when creep failure occurs, and this increase in strain rate is accompanied with a slight increase in permeability, around 0.1-0.2 mD. The intersection points where radial strain rate exceeds the axial strain rate are circled on Figure 5.6. The study performed by Zhang et al. (2015) on the permeability evolution and creep behavior of cataclastic sandstone suggesting that fast creep failure is generally initiated when the radial strain rate exceeds the axial strain rate. This phenomenon is also observed while shear failure occurs. However, despite this similar behavior, the occurrence of fast creep failure can increase the radial strain rate significantly higher than the occurrence of shear failure.

Chapter 6 Conclusion

This thesis illustrates the permeability evolution of chalk under different stress states achieved by five representative test series. Based on the detailed results described in Chapter 4 and the further discussion in Chapter 5 about the mechanical behaviors and their impact on permeability, the main conclusion remarks are as follow.

- **Hydrostatic Loading Effect On Permeability**. The closure of microcracks and fractures is attributed to the reduction in permeability in hydrostatic loading. Permeability evolution is strongly dependent on stress and strain. After a deviatoric loading, the initial permeability prior to the subsequent hydrostatic loading has minor effect on permeability evolution. The permeability-strain curves tend to converge as loading stress increases.
- **Deviatoric Loading Effect On Permeability**. In the 1st deviatoric loading, continuous decrease in permeability is exhibited and more ductile behavior is observed for chalk samples loaded at 3 MPa confining pressure. When loaded at 1.2 MPa confining pressure, the specimen is more brittle, and the increase in the applied axial stress can induce shear failure, resulting in an increase in permeability.
- **Shear Failure and Strain Rate**. Shear failure occurring in the deviatoric loadings accounts for the enhancement of permeability. Shear failure can be identified by comparing the radial strain rate with the axial strain rate. The symbol for a single shear-band failure is the critical point where the radial strain rate exceeds the axial strain rate, indicating that the expansion due to dilatancy becomes predominant.
- **Fast Creep Failure and Strain Rate**. The fast creep failure occurred in deviatoric loading can be also identified by the intersection of radial and axial strain rate. However, the increment in radial strain is more drastic compared to the occurrence of shear failure.

Chapter 7 Future Work

- **Porosity Influence**. The experiments in this thesis are carried out on chalk cores within a small range of porosities varying from 38 to 40%. In order to develop profound understandings of permeability evolution in chalk reservoirs, core samples with a wider range of porosities should be employed. It is described in 5.3 that shear failure contributes to the enhancement of permeability, therefore, the effect of porosity on shear failure and strain rate can also be investigated for obtaining tenable explanations.
- **Confining Pressure Influence**. The effect of confining pressure on permeability during the deviatoric loading phase has been discussed in 5.1 that materials tend to be more brittle at lower confining pressure, therefore, a wider range or more points of confining pressure between 1.2 to 3 MPa can be used to determine the mechanism of the confining pressure influence on permeability evolution in deviatoric loadings.
- **Verification of the relationship between strain rate and single shear-band failure**. The observation and explanation of the single shear-band failure symbol appearing at the critical point where expansion strain rate is greater than the compression strain rate has been discussed in 5.3 and Chapter 4, whereas, more data is needed to testify this assumption and see if it applies to chalk with lower porosities as well.
- **Variation of stress path and pore pressure**. Even though these approaches to investigate the permeability have not been discussed and attempted in this thesis, permeability evolution can be more comprehensively studied and understood by carrying out these two methods. The variation of stress path can be achieved by changing the K value which stands for the constant stress ratio between confining stress and axial stress. Variation in pore pressure can be used to obtain the dependence of permeability on effective stress and distinguish the different behaviors between the application of external compaction pressure and change in internal pore pressure.

Reference

Agarwal, B., Allen, L.R., Farrell, H.E. (1997, December 1), Ekofisk Field reservoir characterization: Mapping permeability through facies and fractures intensity. SPE-35527-PA.

Biot, M.A. (1962). Mechanics of deformation and acoustic propagation in porous media. J. Appl. Phys. 33, 1482-1498.

Bordonaro, C.M., Krempl, E. (1992), The effect of strain rate on the deformation and relaxation behavior of 6/6 nylon at room temperature. Polym. Eng. Sci., 32: 1066-1072. doi: 10.1002/pen.760321604.

Bernabe, Y. (1986), Pore volume and transport properties changes during pressure cycling of several crystalline rocks, Mech. Mater., Vol. 5, 235-249.

Brace, W., Walsh, J., Frangos, W. (1968), Permeability of Granite under high pressure. J. Geophys. Res. 73(6): 2225-2236.

Brace, W.F. (1978), A note on permeability change in geologic materials due to stress. PAGEOPH 116, 627-633.

Byrd, W.D., Geology of the Ekofisk Field, Offshore Norway, Petroleum and the Continental Shelf of Northwest Europe, John Wiley & Sons, New York City (1975) 1,439-445.

Carslaw, H.S., Jaeger, J.C. (1959), Conduction of heat in solids, 2nd edition, Oxford, Clarendon Press.

Chalaturnyk, R.J., Scott, J.D. (1992), Evaluation of reservoir properties from geomechanical tests. J. Cdn. Pet. Tech 31 (5): 31-40.

Collins, P.M., Carlson, M.R., Walters, D.A., Settari, A. (2002), Geomechanical and thermal reservoir simulation demonstrates SAGD enhancement du to shear dilation. Paper, SPE/ISRM 78237 presented at the SPE/ISRM Rock Mechanics Conf. Irving, TX, 20-23 October.

DaSilva, F., Sarda, J.P., Schroeder, C. (1985), Mechanical behavior of chalks. Second North Sea Chalk symposium, Stavanger Norway.

David, C., Wong, T.F., Zhu, W. et al., Laboratory measurement of compaction-induced permeability change in porous rocks: Implications for the generation and maintenance of pore pressure excess in the crust. PAGEOPH (1994) 143: 425.

Edmond, J.M., Paterson, M.S. (1972), Volume change during the deformation of rocks

at high pressure. Int. J. Rock Mech. Min Sci. 9: 161-182.

El-Dessouky, H.T., Ettouny, H.M. (2002), Fundamentals of salt water desalination (Appendix A: Themodynamic Properties), ISBN: 978-444-508 10-2.

Fatt, I., Davis, D.H., Reduction in permeability with overburden pressure. Petroleum Transactions, AIME (1952) Vol. 195, 329.

Feazel, C.T., Farrell, H.E. (1988), Chalk from the Ekofisk area, North Sea: Nannofossils + Micropores = Giant Field. Soc. For Sedimentary Geology (SEPM) Giant Oil and Gas Field, Vol. 1 & Vol. 2 (CW12).

Feazel, C.T., Knight, I.A. Pekot, l.J., Ekofisk Field – Norway Central Graben, North Sea. AAPG Bull. A018 (1990).

Fjær E, Holt R.M., Horsrud P., Raaen A.M., Risnes R. (2008) Petroleum related rock mechanics. Elsevier, 2nd edition.

Gray, D.H., Fatt, I., Bergamini, G., The effect of stress on permeability of sandstone cores. SPE Journal (1963), SPE-531-PA.

Håkansson, E., Bromley, R., Nielsen, P.K. (1974), Maastrichtian chalk of north-west Europe – a pelagic shelf sediment. Spec. Publs. Int. Ass. Sediment 1:211-233.

Handin, J., Hager, Jr.R. V., Experimental deformation of sedimentary rocks under confining pressure: Tests at high temperature. AAPG Bull. Vol. 42, No. 12 (1958). P. 2892-2934.

Hardman, R.F.P., 1982, Chalk reservoirs of the North Sea, Bull. Geol. Soc. Denmark, vol. 30, p. 119-137, Copenhagen, September 1st.

Heiland, J., Permeability of triaxially compressed sandstone: Influence of deformation and strain-rate on permeability. Pure appl. geophys. 160 (2003) 889-908, 0033-4553/03/060889-20.

Indraratna, B., Ranjith, P.G., Gale, W. (1999, January 1), Deformation and permeability characteristics of rocks with interconnected fractures. Int. Soc. For Rock Mechanics. ISRM-9CONGRESS-1999-153.

Jamison, W.R., Tufel, L.W. (1979), Pore volume changes associated with failure and frictional sliding of a porous sandstone. Proc. U.S. Symp. Rock. Mech. 20: 163-170.

Jaumouille, L.D., Cordelier, P.R., Kharroubi, A. (1995), Measurement of gas permeabilities under different compaction modes on tight reservoir samples. SCA conference Paper Number 9519.

Kelkar, S., Zyvoloski, G., Rapaka, S., Yoshioka, K. (2011), Modeling shear failure and

permeability enhancement due to coupled thermal-hydrological-mechanical processes in enhanced geothermal reservoirs. Geothermal Res. Council 35th annual meeting, San Diego, U.S.

Kilmer, N.H., Morrow, N.R., Pitman, J.K., Pressure sensitivity of low permeability sandstones. J. Pet. Sci. & Eng. (1987) 1, 65-81.

Kjørslevik, T., Østensen, G. (2014), The effect of stress level and temperature on water weakening of chalk, BSc thesis, UiS.

Korsnes, R.I., Risnes, R., Faldaas, I., Norland, T., End effects on stress dependent permeability measurements. Tectonophysics Vol. 426 (2006), P. 239-251.

Knutson, C.F., bohor, B.F. (1963), Resrvoir rock behavior under moderate confining pressure, in 5th Symp. On rock mechanics, Univ. Minnesota: New York, MacMillan, P. 627-659.

Lee, B.T., Ghassemi, A. (2001, January 1). Shear slip and permeability change caused by injection/extraction in a fractured reservoir. American Rock Mechanics Association. ARMA-11-355.

Lockner, D.A. (1995), Rock failure. Rock Physics and phase relations. Washington, D.C., American Geophysical Union, 127-147.

Meling, L.M., Lehne, K.A. (1993, January 1), Description and interpretation of North Sea fractured chalk formations. SPE-25640-MS.

Menghini, M.L. (1989, July 1), Compaction monitoring in the Ekofisk area chalk fields. SPE-17853-PA.

Morrow, C.A., Zhang, B.-C., Byerlee, J.D. (1986), Effective pressure law for permeability of westerly granite under cyclic loading. J. Geophys. Res., 91 (B3), 3870-3876, doi:10.1029/JB091iB03p03870.

Nelson, R.A., Handin, J., Experimental study of fracture permeability in porous rock. AAPG Bull. V. 61. No.2 (1997), P. 227-236

Nermoen, A., Korsnes, R.I., Hiorth, A., Madland, M.V. (2015), Porosity and permeability development in compacting chalks during flooding of nonequilibrium brines: Insights from long-term experiment. J. Geophys. Res. Solid Earth, 120, 2935-2960.

Powell, B.N., Lovell, G.L. (1994, January 1), Mechanisms of chalk compaction. SPE-28132-MS.

Read, M.D., Meredith, P.G., Murrell, S.A.F. (1989, January 1), Permeability measurement techniques under hydrostatic and deviatoric stress conditions.

International Society for Rock Mechanics.

Rhett, D.W., Teufel, L.W., Effect of reservoir stress path on compressibility and permeability of sandstone. 67th SPE Annual Tech Conf & Exhib, Washington DC, October 4-7 (1992), SPE-24756-MS.

Scholle, P.A., Chalk diagenesis and its relation to petroleum exploration. Oil from chalks, a Modern Miracle?, AAPG Bull., (1977) 61, 982-100.

Scott, J.D., Adhikary, D., Proskin, S.A. (1991), Volume and permeability changes associated with steam stimulation in an oil and reservoir. Presented at Petro. Soc. Of CIM and AOSTARA Tech Conf. Banff, Alberta. April 21-24.

Skempton, A.W., The pore pressure coefficient A and B. Geotechnique 4 (1954), 143-147.

Skovbro, B., Depositional conditions during Chalk sedimentation in the Ekofisk area Norwegian North Sea. In: J.P.H. Kaasschieter and T.J.A. Reijers (eds.): Petroleum geology of the southeastern North Sea and the adjacent onshore areas (The Hague. 1982) – Geol. Mijnbouw 62: 169-175.

Sulak, R.M., Danielsen, J., Reservoir aspects of Ekofisk subsidence. J Petrol Technol (1989) 41(7): P. 709-716, SPE 17852-PA.

Tang, G., Firoozabadi, A. (2001), Effect of pressure gradient and initial water saturation on water injection in water-wet and mixed-wet fractured porous media. SPE 4(6): 516-524.

Terzaghi, K.V. (1923), Die berechnung der durchässugkeitsziffer des tones aus dem verlauf der hydrodynamischen spannungserscheinungen. Sitzungsber. Akad. Wiss. Wien Math. Naturwiss. Kl. Abt. 132(2A): 125-138

Teufel, L.W. (1987, January 1), Permeabiltiy changes during shear deformation of fractured rock. ARMA-87-0473.

Teufel, L.W., Permeability changes during shear deformation of fractured rock. 28th U.S. sym. on rock mechanics, Tucson (1987), ARMA-87-0473.

Teufel, L.W., Rhett, D.W. (1991, January 1). Geomechanical evidence for shear failure of chalk during production of the Ekofisk Field. SPE-22755-MS.

Teufel, L.W., Rhett, D.W., Failure of chalk during waterflodding of the Ekofisk Field. SPE Annual Tech Conf. & Exhib. Washington, October 4-7 (1992) SPE-24911-MS.

Teufel, L.W., Warpinski, N.R., Laboratory determination of effective stress laws for deformation and permeability of chalk. International Journal of Rock

Mechanics and Mining Science & Geomechanics Vol. 30 (1990) P. 1169-1172.

Thomas, L.B., 1981, Deformation of chalk under confining pressure and pore pressure. SPE-8076-PA.

Van Den Bark, E., Thomas, O.D. (1981), Ekofisk: First of the giant oil fields in Western Europe. AAPG Bull. Vol. 65 No. 11, P. 2341-2363.

Vairogs, J., Hearn, C.L., Dareing, D.W., Rhoades, V.W. (1958), The effective compressibility of reservoir rock and its effect on permeability: Soc. Pet. Eng. AIME Trans., v. 213, p. 386-388.

Wang, W.-x., Madland, M.V., Zimmermann, U., Nrmoen, A., korsnes, R.I., Bertolino, S.R.A., Hildebrand-Habel, T. (2016), Evaluation of porosity change during chemo-mechanical compaction in flooding experiments on Liege outcrop chalk. Geo. Sco., London, Special Publications, 435, doi: 10.1144/SP435.10.

Wiborg, R., and J. Jewhurst, 1986, Ekofisk subsidence detailed and solutions assessed: Oil and Gas Journal, v. 84, no. 7, p. 47-55.

Zhang, J., Wong, T.-F., Davis, D.M. (1990), High pressure embrittlement and shear-enhanced compaction of Berea sandstone: Acoustic emission measurement and microstructural observation. Rock Mechanics Contributions and Challenges, ISBN 9061911230.

Zhang, Y., Shao, J.F., Xu, W.Y., Jia, Y., Zhao, H.B. (2015) Creep behavior and permeability evolution of catacalstic sanstone in triaxial rheological tests, European Journal of Environmental and Civil Enginnering, 19:4, 496-519, doi:10.1080/19648189.2014.960103.

Zhu, W., Montesi, L.G.J., Wong, T.-f., Shear-enhanced compaction and permeability reduction: Triaxial extension tests on porous sandstone. (1997), Mechanics of Materials Vol. 25, p. 199-214.

Zhu, W., Montési, L. Wong, T.-f., Characterizing the permeability-porosity relationship during compactive cataclastic flow. 42nd U.S. Rock Mechanics Sym, San Francisco, June 29-July 2, (2008), ARMA-08-290.

Zhu, W., Wong, T.-f. (1997) The transition from brittle faulting to cataclastic flow: permeability evolution. J. Geophys. Res., 102, 3027-3041.

Zoback, M.D. (2007), Reservoir Geomechanis. 1st Edition. ISBN-978-0-521-77069-9.